

BULGARIAN CHEMICAL COMMUNICATIONS

2025 Volume 57 / Number 2

*Journal of the Chemical Institutes
of the Bulgarian Academy of Sciences
and of the Union of Chemists in Bulgaria*

Drying of sour cherry with microwave and infrared drying methods; investigation of drying kinetics and parameters

G. Geniş, O. İsmail*

Department of Chemical Engineering, Faculty of Chemical and Metallurgical Engineering, Yıldız Technical University, Davutpaşa Campus, 34210, Esenler, Istanbul, Turkey

Received: July 21, 2022; Accepted: March 18, 2025

In this study, sour cherry samples (*Prunus cerasus* L.) were subjected to infrared and microwave drying. Before drying, the physical and mechanical properties of the sour cherry samples were determined along with the moisture content. For infrared drying, three different drying temperatures (50, 60 and 70°C) were used, while for microwave drying, three different microwave power levels (140, 210 and 350 W) were used. Drying took place completely during the falling rate period. The results showed that the moisture content and drying rate were affected by increased drying power level and drying air temperature. Microwave drying shortened the drying time and increased effective moisture diffusion (D_{eff}) when compared to infrared drying. Six different drying models were applied for all temperatures and power levels and the Alibas model best fitted the data. The activation energies were found to be 0.020 and 3.56 kW kg⁻¹ for microwave drying and infrared drying, respectively. High "L" and low "ΔE" values were obtained in infrared drying method of sour cherries.

Keywords: Sour cherry, microwave drying, infrared drying, quality

INTRODUCTION

Sour cherry (*Prunus cerasus* L.) is an important fruit produced especially in the Russian Federation, Turkey, Ukraine, Poland, Iran, the United States and Serbia. Based on Food and Agriculture Organization (FAO) statistics, Turkey produced approximately 143197 tons of sour cherries in 2019, ranking second in world cherry production after the Russian Federation [1]. About half of the total amount of cherry produced in Turkey is consumed as fresh fruit. The other half is used after processing as juice, sauces, pastilles, jam and frozen products [2].

A significant part of agricultural products need to be stored [3]. Storage conditions of dried fruits are more favorable and drying is preferred and applied due to economic gain.

Dried fruits, vegetables and spices constitute a large part of our exports, and the income from these products constitutes a large part of our total export income. In 2020, our country's total export of dried fruit was 477150 tons and its value was \$1.4 billion. In the first five months of 2021, our exports continued with \$514 million, an increase of 12 percent compared to the same period of the previous year. European Union countries and the USA come to the fore in our exports [4].

The aim in drying sour cherry is to reduce the moisture content to a level that will allow safe storage for a long time.

In other words, along with the decrease in water amount with the drying process, the possibility of enzymatic and microbiological spoilage is significantly reduced. However, since it is not possible to provide hygienic conditions with the sun drying method, which is widely used in Turkey, the products are polluted. In addition, due to the fact that drying takes a very long time, respiration continues especially in fruits for a while, and even a slight fermentation occurs most of the time, material losses occur and as a result, the quality of the products deteriorates. For this reason, the need to dry the products under controlled conditions arises and the necessity and number of drying facilities and systems is gaining importance day by day [5].

The most widely used method industrially is convection drying. Generally, products are dried with a tray dryer. In recent years, instead of drying with hot air due to long drying times, drying methods such as microwave and infrared have been studied. As for why, color quality and energy consumption of the product is very important in drying. Drying needs high energy input, but World's energy resources are limited. Thus, to balance energy demands, the development of energy systems with high efficiencies and minimal costs is important [6].

Due to the low thermal conductivity of food, heat transfer to the interior of the food is limited during conventional heating.

* To whom all correspondence should be sent:
E-mail: ismail@yildiz.edu.tr

This problem has resulted in the increased use of infrared radiation and microwaves in food drying to achieve fast and effective heat treatment.

In microwave drying, high-frequency waves rapidly pass through the dried material, are absorbed and converted into heat energy causing the water in the material to evaporate. The internal temperature of the food dried using microwave is higher than the surface temperature, and a more dynamic moisture transfer takes place compared to conventional drying [7].

One of the most important drying methods of foods with high moisture content is drying with infrared radiation. It penetrates into the material being dried and generates heat, but its penetrating power is limited. Certain features such as thermal efficiency, wavelength, fast heating rate, direct heat penetration into the product and reflectivity make IR heating more effective for some applications and provide significant reductions in energy consumption [8, 9].

The drying process is usually carried out in thin layers. Therefore, modeling the convective thin layer drying of sour cherry slices is necessary for better control of the drying process and quality drying of sour cherries in accordance with the standards of the importing countries. Unfortunately, there are very few studies on the drying behavior of sour cherry by microwave and infrared drying methods in the literature. Methods for hot-air drying of sour cherry [2, 10-12] are some examples. In contrast, Ghaderi *et al.* (2011) [13] and Motavali *et al.* (2013) [14] developed microwave-vacuum drying techniques to study the drying of sour cherry. Amiri Chayjan *et al.* (2014) [9] on the other hand, tried to model some drying properties of sour cherry using mathematical models and artificial neural networks under infrared irradiation.

Although a lot of information has been collected about physical and mechanical properties, effective moisture diffusion, activation energy and color parameters for various food products, there is very little published literature on effective moisture diffusion, activation energy and color parameters for sour cherry by infrared and microwave drying. The main purpose of this research is to determine the effective moisture diffusion, activation energy and color parameters of sour cherry during microwave and infrared thin layer drying process and model it using microwave power and IR radiation temperature. In order to compare the infrared method with the microwave method for drying sour cherries, the drying kinetics, the values of effective moisture diffusivity, activation energy and color

changes were determined. The moisture ratios were modeled using six thin-layer drying models.

MATERIALS AND METHODS

Materials

Sour cherries, which are grown in Çorlu location (Tekirdağ, Turkey) were provided from a local market in Çorlu in August 2021 and were kept in a refrigerator at a temperature of 4°C. The average length, width and thickness of the sour cherry are 17.20 ± 1.98 , 18.90 ± 2.22 and 18.45 ± 2.25 mm, respectively. Before the drying experiments and moisture determination the cherry samples were removed from the refrigerator and kept in a desiccator at room temperature for 2 h. Dry matter and moisture contents of the sour cherry samples were determined prior to the drying process. To determine the initial moisture content, four 10 g-samples were dried in an oven (Memmert UM-400, Germany) at 105°C for 24 h [15]. The average initial moisture content of the sour cherry was found to be about 74.40% w.b.

Determination of dimensional properties of sour cherry samples

The dimensions of 20 randomly selected sour cherry samples were determined. Using an electronic caliper with a precision of 0.01 mm, the three fundamental axial dimensions of the sour cherry samples were measured.

The arithmetic mean diameter (AMD), geometric mean diameter (GMD), sphericity index (SP), surface area (S) and aspect ratio (AR) of cherry samples were calculated using equations (1)-(5) obtained as a result of literature review. The formulas are as follows [16-19]:

Arithmetic mean diameter (AMD or D_a) mm:

$$D_a = (L+W+T)/3 \quad (1)$$

Geometric mean diameter (GMD or D_g),

$$\text{mm: } D_g = (L*W*T)^{1/3} \quad (2)$$

$$\text{Sphericity index (Sp), \%: } S_p = (D_g/L)100 \quad (3)$$

$$\text{Surface area (S), mm}^2: S = \pi(D_g^2) \quad (4)$$

$$\text{Aspect ratio (AR or } R_a): R_a = W/L \quad (5)$$

Drying equipment and drying procedure

Microwave drying process was performed in a home type Delonghi MW205S model microwave dryer with a working interval of 140-790 W (Delonghi, Treviso, Italy).

Before drying, the core of the samples was removed and divided into two parts. The sour cherry samples (approximately 15 ± 0.2 g) were dried in a microwave dryer at 140, 210 and 350W power level until the water content decreased to about 8.5% (w.b). The dried samples were removed from the

microwave at intervals of 60 s for 140W, 30 s for 210W, and 15 s for 350W, and their weights were measured with a digital balance (model BB3000, Mettler-Toledo AG, Greifensee, Switzerland) with an accuracy of 0.1 g.

Infrared drying experiments were performed using the MA 50.R model infrared moisture analyzer which works with 230 V at 50 MHz (Radwag Balances and Scales, Radom, Poland). Taking into account the effect of temperature, the sour cherries were dried in an infrared dryer at 50, 60 and 70°C. Sample weight was noted from the infrared radiation dryer screen at 15 min intervals for each temperature in infrared drying method. The drying process was terminated when the moisture content decreased to about 8.5% (w.b.) from an initial value of 74.40% (w.b.). All drying experiments were repeated three times and average values were used in the calculations.

Mathematical modeling of drying curves

The moisture content of drying samples at time t can be transformed to moisture ratio (MR) [20]:

$$MR = \frac{M_t - M_e}{M_0 - M_e} \quad (6)$$

where: M_t is the moisture content at time (g water/g dry matter), M_0 is the initial moisture content (g water/g dry matter), M_e is the equilibrium moisture content (g water/g dry matter).

The drying rate (DR) of sour cherry samples was calculated using equation (7):

$$DR = \frac{M_t - M_{t+\Delta t}}{\Delta t} \quad (7)$$

where: $M_{t+\Delta t}$ is the moisture content at $t+\Delta t$ (g water/g dm), and t is time (min).

In this study, drying curves were fitted to six different thin-layer drying models to select a suitable model to describe the drying process of sour cherry samples. (Table 1). The MR in these equations represents the moisture content or moisture ratio and drying time of the samples at any given moment. The moisture ratio was simplified to M_t/M_0 instead of equation 1 by some investigators [21, 22].

The obtained data were fitted to the models and their corresponding constants were calculated using Statistica 6.0 program software (Statsoft Inc., Tulsa, OK). In addition, one-way analysis of variance (ANOVA) and multiple comparisons (post-hoc LSD; least significant-difference test) were used to evaluate the significant differences of the data at $p \leq 0.05$. The data were expressed as means \pm standard deviation (SD).

Table 1. Mathematical models applied to the sour cherry samples drying curves

Model name	Equation	Ref.
Aghbashlo <i>et al.</i>	$MR = e^{\left(\frac{-k_1 t}{1+k_2 t}\right)}$	[23]
Alibas	$MR = ae^{(-kt^n)} + bt + g$	[24]
Jena and Das	$MR = ae^{(-kt+bt^{0.5})} + c$	[25]
Parabolic	$MR = a + bt + ct^2$	[21]
Verma	$MR = ae^{(-kt)} + (1-a)e^{(-gt)}$	[26]
Wang and Singh	$MR = 1 + at + bt^2$	[26]

a, b, c, k, n, g : Constants in models, MR : Moisture ratio, t : Drying time

To determine the best fitted model, the coefficient of determination (R^2), root mean square error ($RMSE$) and reduced chi-square (χ^2) statistical evaluation methods were applied. In the literature, higher R^2 values and lower (χ^2) and $RMSE$ values were accepted as better results.

These parameters can be calculated using equations (8) and (9):

$$\chi^2 = \frac{\sum_{i=1}^N (MR_{exp,i} - MR_{pre,i})^2}{N-z} \quad (8)$$

$$RMSE = \left[\frac{1}{N} \sum_{i=1}^N (MR_{pre,i} - MR_{exp,i})^2 \right]^{\frac{1}{2}} \quad (9)$$

where: $MR_{exp,i}$ and $MR_{pre,i}$ represent the experimental and predicted values of moisture ratios, respectively. N is the total number of experiments, and z is the number of constants in the model.

Calculation of moisture diffusivity and activation energy

In drying, diffusion is used to indicate the rate of moisture flow or the movement of moisture out of the material. The drying process (infrared-microwave drying) of foodstuffs usually takes place during the falling rate period. Moisture is transferred *via* molecular diffusion during the falling rate period.

A diffusion model (based on some assumptions) based on Fick's second diffusion law was used to determine the effective moisture diffusion coefficients and equation (10) can be simplified as given in [20]:

$$\ln(MR) = \ln\left(\frac{8}{\pi^2}\right) - \left(\frac{\pi^2 \cdot D_{eff}}{4L^2} t\right)$$

$$S = \frac{\pi^2 D_{eff}}{4L^2} \quad (10)$$

where, D_{eff} , L , t and S are the effective moisture diffusivity (m^2/s), the half-thickness of the samples (cm), the drying time (s) and the slope, respectively.

The dependence of the effective diffusivity on temperature and power level is described by the Arrhenius equation [22, 27].

$$D_{eff} = D_o \exp\left(-\frac{E_a}{RT}\right) \quad (11)$$

where: D_o (m^2/s), E_a (J/mol), R ($8.314 J/(mol \times K)$) and T (Kelvin) are the pre-exponential factor of Arrhenius equation, activation energy, universal gas constant and temperature, respectively.

$$D_{eff} = D_o \exp\left(-m \frac{E_a}{P}\right) \quad (12)$$

where: P is the drying power level and m is the sample weight (g).

Color parameters

Color measurements of fresh and dried sour cherry samples were done with Chroma Meter (PCE-CSM 1, PCE GmbH, Germany). Five random readings for each selected sample were recorded. The color was measured in terms of CIEL, procedure was based on the determination of values L (lightness/darkness), a (redness/greenness), and b (yellowness/blueness). The total color changes (ΔE) of the sour cherry samples were calculated from the equation below [22]:

$$\Delta E = \sqrt{(\Delta L)^2 + (\Delta a)^2 + (\Delta b)^2} \quad (13)$$

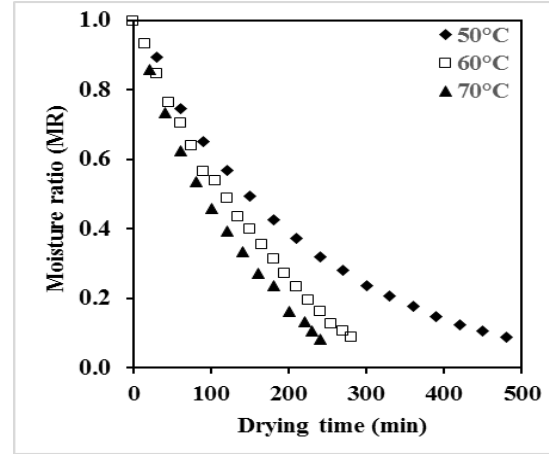
RESULTS AND DISCUSSION

Calculation of dimensional properties

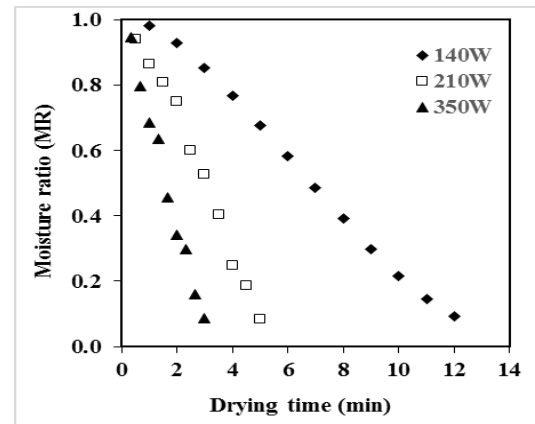
The necessary measurements were carried out on 20 randomly selected samples from sour cherries purchased from the market. The average principle dimensions of the sour cherries, viz. longitudinal axis, intermediate axis, and transverse axis were found to be 17.20 ± 1.98 , 18.90 ± 2.22 and 18.45 ± 2.25 mm, respectively. The average sour cherries arithmetic mean diameter (AMD) and geometric mean diameter (EMD), were found to be 18.18 ± 2.07 mm, and 18.16 ± 2.06 mm, respectively. These average diameters will help us in evaluating the projection area of a fruit particle moving in the turbulent region of an air flow and in drying the fruits [17]. The sphericity index (SP), surface area (S) and aspect ratio (AR) were calculated as 105 ± 4.32 , 1035.5 ± 229.75 mm² and 1.09 ± 0.07 , respectively. The fruit's flow ability characteristics can be seen in terms of aspect ratio and sphericity. Pradhan *et al.* have proved in 2012 that these two parameters affect the flow of the fruit [28]. A sphericity value between 1 and 0.90 indicates perfection for the fruit [29]. The value of 1.05 found for sour cherry is considered to be a high sphericity index value.

Change of moisture ratio and drying rate during microwave and infrared drying

The drying curves (drying time versus moisture ratio) of the sour cherries microwave dried at 140, 210 and 350W and infrared dried at 50, 60 and 70°C are presented in Figure 1.



(A)



(B)

Figure 1. Drying curves of sour cherries with infrared and microwave drying methods at different temperatures (A) and power levels (B).

Drying of sour cherries with both microwave and infrared dryers started at an initial moisture content of approximately 74.40% (w.b.) and continued until a final moisture content of 8.50% (w.b.) was reached.

As shown in Figure 1, the times to reach 8.50% (w.b.) moisture content from the initial moisture content of sour cherries in microwave drying at 140, 210 and 350W were found to be 12, 5 and 3 min, respectively whereas in infrared drying the times were found to be 480, 280, and 240 min for drying at 50, 60, and 70°C, respectively. Reducing the moisture content of foods down to between 10 to 20% by weight prevents bacteria, mold, yeast and enzyme damage [27].

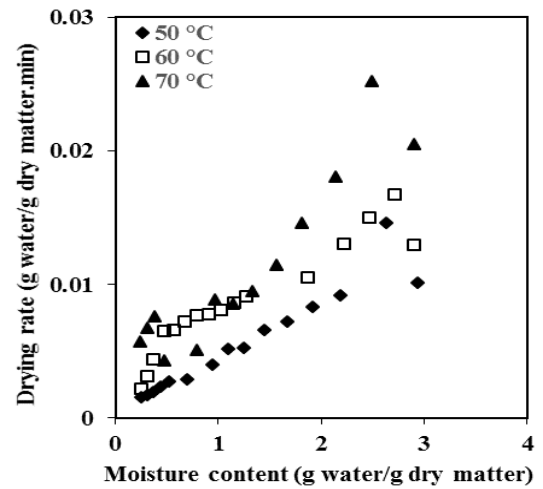
As expected, the increase in drying temperatures and power levels resulted in a decrease in the drying time of the sour cherry samples for both drying methods. A fast decrease in the moisture content was observed for all drying conditions applied at the beginning of the drying process; however, this drying rate decreased as the drying proceeded. Similar results were also reported for fruit products by earlier researchers [30, 31].

Sour cherry samples dried by the microwave drying method were found to have a shorter drying time by comparison with infrared drying method and the results show that microwave drying was a more effective method for drying sour cherry samples.

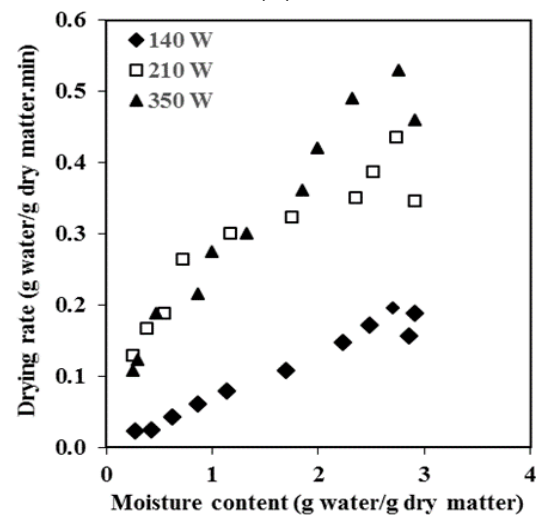
The changes in drying rates *versus* moisture content for both microwave and infrared dryers are shown in Figure 2.

The drying rate decreased continuously with increasing drying times or decreasing moisture content. These findings are also in agreement with previous studies [32]. The microwave drying method showed higher drying rate at all three conditions as compared to the infrared drying method. As the temperature and power level increased, drying rate increased in both drying methods.

When analyzing Figure 2, two different periods can be defined: warming and falling rate periods. In the drying rate curves of both drying methods, no constant-rate drying period was obtained. Drying occurred in the falling rate period for both drying methods. In other words; initially, when the moisture content was high, the drying rate at all drying conditions increased with time corresponding to a transition period in which isothermal and non-isobaric conditions were present, but then decreased steadily as the moisture content decreased. The presence of falling rate drying behavior is indicative of a gradual increase in both mass and internal resistance to heat transfer [33]. It may be that the porosity of the samples decreases over time, the resistance to the movement of water increases as a result of shrinkage as drying progresses, leading to a further reduction in drying rates [34].



(A)



(B)

Figure 2. Drying rates *versus* moisture content of sour cherry samples at different temperatures (A) and power levels (B)

Evaluation of the models

Thin-layer drying models, preliminary evaluation of all drying processes, have significant practical value for engineers. Moisture contents of sour cherry samples were converted to dimensionless moisture ratio so that modeling studies could be carried out easily. Moisture ratio values of sour cherry samples were calculated by using Equation 6. The experimental data were fitted to the models given in Table 1 and statistical data are shown in Table 2.

Table 2. Statistical results obtained with the different thin-layer drying models for sour cherries samples compared with experimental values

Models	Parameters	Microwave drying			Infrared drying		
		140 W	210 W	350 W	50°C	60°C	70°C
Aghbashlo <i>et al.</i>	R^2	0.9989	0.9995	0.9972	0.9961	0.9985	0.9946
	χ^2	0.000098	0.000084	0.000029	0.000356	0.000184	0.000742
	$RMSE$	0.009102	0.007273	0.004791	0.017238	0.012423	0.021694
Alibas	R^2	0.9996	0.9999	0.9992	0.9987	0.9991	0.9995
	χ^2	0.000054	0.000008	0.000145	0.000156	0.000137	0.000052
	$RMSE$	0.006152	0.004684	0.010183	0.010837	0.005065	0.005809
Jane and Das	R^2	0.9991	0.9974	0.9963	0.9994	0.9995	0.9996
	χ^2	0.000210	0.000604	0.000977	0.000104	0.000201	0.000161
	$RMSE$	0.012062	0.020064	0.024937	0.001802	0.011973	0.011284
Parabolic	R^2	0.9971	0.9956	0.9953	0.9982	0.9989	0.9992
	χ^2	0.000831	0.001167	0.001205	0.000544	0.000347	0.000264
	$RMSE$	0.025279	0.029579	0.029608	0.021163	0.016517	0.01492
Verma	R^2	0.9763	0.9664	0.9948	0.9991	0.9990	0.9973
	χ^2	0.005980	0.008911	0.001466	0.000058	0.000080	0.000564
	$RMSE$	0.067822	0.081751	0.032654	0.006932	0.007923	0.02179
Wang and Singh	R^2	0.9946	0.9958	0.9949	0.9972	0.9989	0.9991
	χ^2	0.001166	0.001116	0.001287	0.000889	0.000444	0.000130
	$RMSE$	0.031415	0.03049	0.03245	0.028013	0.019504	0.016404

The best model describes the thin-layer drying properties of sour cherry samples chosen as the model with the highest R^2 values and the lowest χ^2 and $RMSE$ values. As can be seen from Table 2, the R^2 values were higher than 0.9664 which indicates a good fit because a R^2 value close to one implies that the predicted drying data are close to the experimental drying data.

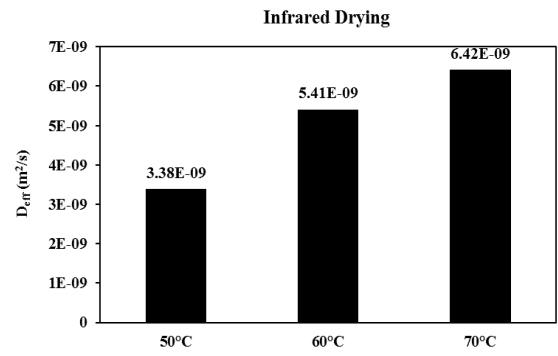
Another statistical parameter calculated to compare the accuracy of the model is the root mean square error ($RMSE$) and reduced chi-square (χ^2) values, which represent the differences between the estimated and experimental values. It is desirable that χ^2 and $RMSE$ be close to zero. As a result, the Alibas model was found to be the best model for all drying methods and drying conditions.

Determination of effective diffusivity

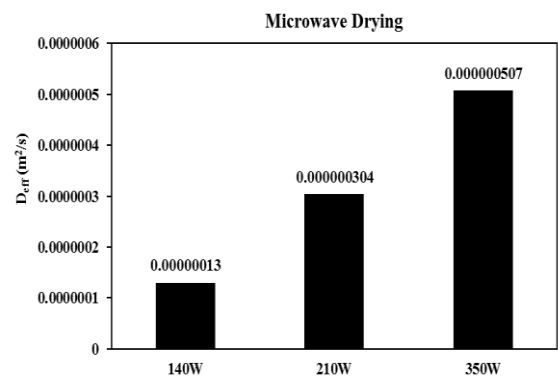
The variation of effective diffusion coefficients with temperature and power levels is shown in Figure 3.

As seen in Figure 3, based on the analytical solution of Fick's second law, the effective moisture diffusion of sour cherries was found in the range of 1.30×10^{-7} and 5.07×10^{-7} m²/s in microwave drying, 3.38×10^{-9} and 6.42×10^{-9} m²/s in infrared drying. The result is that the effective moisture diffusion increased with the increase in drying temperature and power levels. In addition, it was observed that the effective moisture diffusion values in the microwave drying method were higher than the infrared drying method. From this research, effective

diffusion values were found in the reference range of 10^{-12} to 10^{-8} m²/s for the drying of foodstuffs [35].



(A)



(B)

Figure 3. The effective moisture diffusivity obtained for sour cherry samples dried at different temperatures (A) and power levels (B).

Color analysis

Activation energy is defined as the minimum energy required for the moisture transfer to begin and continue. The logarithm of effective diffusivity (D_{eff}) as a function of the reciprocal of absolute temperature (T) and power level (P) is plotted in Figure 4.

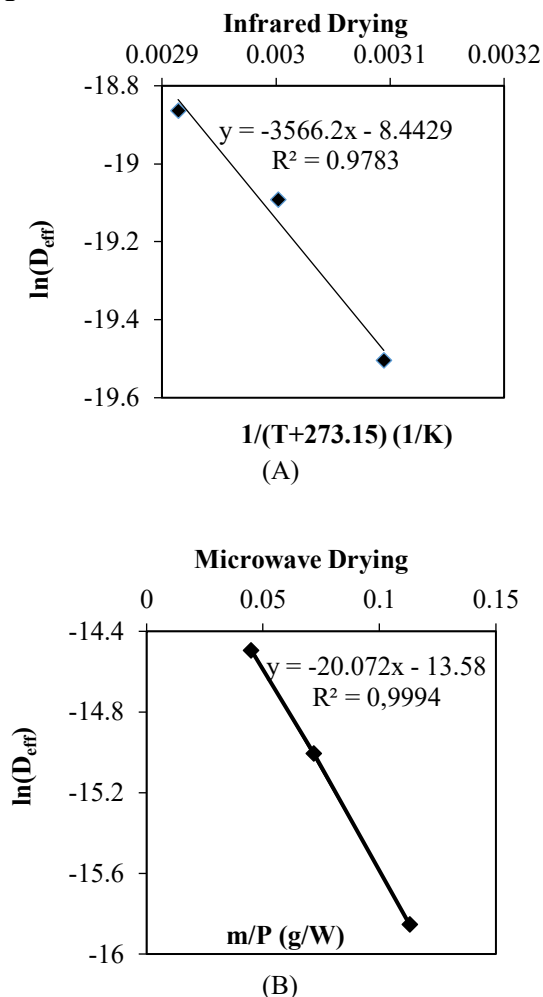


Figure 4. Variation of $\ln(D_{eff})$ with $1/T$ (A) and m/P (B).

The Arrhenius equation should sometimes be viewed simply as a method of curve-fitting, without physical interpretation, where the D_0 and E_a values represent suitable nonlinear regression constants. The activation energy can be calculated from the slope of the plot of $\ln(D_{eff})$ vs. $1/T$ (1/K) or m/P (g/W) and estimated E_a values are 3.56 and 0.020 kW/kg, for the infrared and microwave drying methods, respectively. Again from the same equations, the estimated D_0 values of the sour cherry samples dried by infrared and microwave drying methods were found as $2.156 \times 10^{-4} \text{ m}^2/\text{s}$ and $1.267 \times 10^{-6} \text{ m}^2/\text{s}$, respectively. The estimated D_0 values obtained in the present work were found to be compatible with the values reported in the literature [36-38].

The drying process changes the surface properties of foods. This causes reflection and color change. Therefore, the operating temperatures should be kept low. In this study, the total color change (ΔE) value was measured to determine color differences between fresh and dried sour cherries for both methods. L , a , and b , and corresponding ΔE values are shown in Table 3.

Variance analysis of the color parameters was carried out to examine the influence of the main factors, namely drying methods and conditions.

As seen in Table 3, the color values were measured as 15.14 ± 0.23 , -9.71 ± 0.18 and 20.55 ± 0.69 for " L ", " a " and " b ", respectively in the fresh sour cherry samples. A significant decreased in " b " values was observed in both drying methods while " a " values have increased slightly. The coordinate " L " values of cherries dried by microwave and infrared drying methods has changed very little compared to the fresh sample. In other words, while some decrease in " L " values was observed in the microwave drying method at 210 and 350 W, " L " values increased slightly in infrared drying. For drying by infrared and microwave methods, the differences in lightness, redness and yellowness are not so evident ($p < 0.05$).

When using fresh cherry samples as a reference, higher ΔE represents a greater color change from the reference material. Since total color difference (ΔE) is a function of the three CIE L^* , a^* , and b^* coordinates (Eq.(13)), the ΔE values ranged between 9.84 ± 0.09 – 14.06 ± 0.15 and 7.53 ± 0.06 – 13.20 ± 0.13 for the microwave and infrared drying methods, respectively. Increasing the drying temperature and power level generally resulted in lower color change. Color changes caused by drying temperatures and power levels in sour cherry samples may be closely related to pigment degradation, formation of brown pigments by non-enzymatic (Maillard reaction) and enzymatic reactions. The Maillard reaction usually occurs when foods are heated. The parameters affecting the Maillard reaction are primarily sugars and proteins, temperature and duration of the heat treatment [39]. The lowest total color change was observed in infrared drying at 70°C .

The analysis showed a statistically significant influence of the drying temperature and method on the sour cherries color. An ANOVA analysis of total color change of the dried sour cherries samples showed the existence of four groups which differed significantly from one another ($p < 0.05$; post-hoc LSD) depending on the different drying conditions.

Table 3. Color values of fresh and dried sour cherries

Drying method	Drying Conditions	Color Parameters			ΔE
		<i>L</i>	<i>a</i>	<i>b</i>	
	Fresh	15.14 ± 0.23 ^b	-9.71 ± 0.18 ^a	20.55 ± 0.69 ^b	0
Microwave Drying	140 W	15.65 ± 0.07 ^a	-5.74 ± 0.19 ^b	7.06 ± 0.27 ^d	14.06 ± 0.15 ^a
	210 W	14.98 ± 0.08 ^c	-7.00 ± 0.30 ^d	8.79 ± 0.82 ^a	12.06 ± 0.16 ^c
	350 W	14.56 ± 0.32 ^d	-8.15 ± 0.56 ^b	10.84 ± 0.32 ^d	9.84 ± 0.09 ^b
Infrared Drying	50°C	15.90 ± 0.18 ^a	-5.46 ± 0.19 ^c	8.07 ± 0.56 ^c	13.20 ± 0.13 ^d
	60°C	15.38 ± 0.19 ^b	-6.30 ± 0.25 ^b	9.20 ± 0.11 ^b	11.85 ± 0.35 ^c
	70°C	15.60 ± 0.41 ^c	-7.45 ± 0.32 ^d	13.37 ± 0.52 ^b	7.53 ± 0.06 ^b

Note: Means ± SD are given in the Table; significantly ($P < 0.05$). ^{a b c d} - groups that are statistically significantly ($p < 0.05$) different from each other according to drying temperature.

When infrared drying and microwave drying are compared, sour cherries samples dried with infrared drying yielded lower total color change (ΔE) than microwave drying at all drying conditions. Similar results have been reported by Wojdyło *et al.* [40]. and Sumic *et al.* [41] for sour cherries.

CONCLUSION

Both methods of drying have greatly influenced the drying characteristics of the sour cherry samples.

The drying rate and product quality was significantly influenced by the drying method, power level and temperatures. In both drying methods, the drying time decreased with increasing power level and temperature, but the effective diffusion coefficient increased.

The microwave drying method was found to provide shorter drying time and increased moisture diffusion; therefore, the microwave drying method could be the first choice for dehydration of foods.

In order to explain the drying behavior of sour cherry samples, six different thin-layer drying models were compared according to their coefficient of determination, reduced chi-square and root mean square error values. For both drying methods, the Alibas model showed a better fit to the experimental sour cherry data compared to the other models.

According to the results obtained, infrared drying method has a significant effect on the final quality (ΔE) of dried sour cherry samples.

Based on the results of the present investigation, it may be concluded that microwave drying is suitable for large-scale production in terms of short drying time, while infrared drying - in terms of product quality.

Acknowledgment: This work was supported by the Research Fund of the Yildiz Technical University. Project Code: FYL-2021-4585.

REFERENCES

1. FAO Statistical database. <http://www.faostat.fao.org/> (accessed 2021) 2019.

- H. R. Gazor, S. Maadani, H. Behmadi, *Agric. Conspec. Sci.*, **79**, 119 (2014).
- A. Basman, S. Yalcin, *J. Food Eng.*, **106**, 245 (2011).
- <http://www.turktarim.gov.tr>
- J. Wang, Y.S. Xi, *J. Food Eng.*, **68**, 505 (2005).
- I. Shabbir, M. Mirzaeian, *Int. J. Hydrog. Energy*, **41**, 16535 (2016).
- J. Wang, K. Sheng, *LWT*, **39**, 247 (2006).
- N. Sakai, W. Mao, Infrared heating, in: Sun, D.-W. (ed.), *Thermal Food Processing: New Technologies and Quality Issues*. CRC Press LLC, USA, 2006.
- R. Amiri Chayjan, M. Kaveh, S. Khayati, *Agric. Eng. Int: CIGR J.*, **16**, 265 (2014).
- I. Doymaz, *J. Food Eng.*, **78**, 591 (2007).
- M. Aghbashlo, M. H. Kianmehr, S. R. Hassan-Beygi, *J. Food Process. Preserv.*, **34**, 351 (2010).
- H. R. Gazor, O.R. Roustapour, *Int. Food Res. J.*, **22**, 476 (2015).
- A. Ghaderi, S. Abbasi, A. Motevali, S. Minaei, *Iran. J. Nutr. Sci. Food Technol.*, **6**, 55 (2011).
- A. Motavali, G.H. Najafi, S. Abbasi, S. Minaei, A. Ghaderi, *J. Food Sci. Technol.*, **50**, 714 (2013).
- AOAC, *Official methods of analysis*, Arlington, USA, 1990.
- N. N. Mohsenin, *Physical properties of plant and animal materials*, **1**, New York, Routledge, 2020.
- S. S. Pathak, R. C. Pradhan, S. Mishra, *J. Food Process. Eng.*, **42**, e12992 (2019).
- V. Kamat, J.H. Sisodiya, M. K. Mahawar, K. Jalgaonkar, *Int. J. Chem. Stud.*, **8**, 225 (2020).
- R. Ilić, I. Glišić, T. Milošević, G. Paunović, *Acta Agric. Serb.*, **24**, 181 (2019).
- A. S. Kıpçak, O. İsmail, *J. Food Sci. Technol.*, **58**, 281 (2021).
- A. S. Kıpçak, *Res. Chem. Intermed.*, **43**, 1429 (2017).
- O. İsmail, O.G. Kocabay, *Turk J Fish Aquat. Sci.*, **18**, 259 (2018).
- M. Aghbashlo, M. H. Kianmehr, S. Khani, M. Ghasemi, *Int. Agrophys.*, **23**, 313 (2009).
- I. Alibas, *J. Agric. Sci.*, **18**, 43 (2012).
- S. Jena, H. Das, *J. Food Eng.*, **79**, 92 (2007).
- I. Alibas, *Food Sci. Technol.*, **34**, 394 (2014).
- O. İsmail, O.G. Kocabay, *Br. Food J.*, **124**, 1238 (2022).
- R. C. Pradhan, P.P. Said, S. Singh, *Agric. Eng. Int.*, **15**, 106 (2012).

29. A. Field, *Discovering Statistics using SPSS for Windows*, London-Thousand Oaks-New Delhi, Sage Publications, 2000.
30. I. Hammouda, D. Mihoubi, *Energy Convers. Manag.*, **87**, 832 (2014).
31. N. Izli, G. Yıldız, H. Unal, E. Işık, V. Uylaşer, *Int. J. Food Sci. Technol.*, **49**, 9 (2014).
32. A. Stegou-Sagia, D.V. Fragkou, *J. Therm. Eng.*, **1**, 236 (2015).
33. H. Darvishi, *Braz. J. Chem. Eng.*, **34**, 143 (2017).
34. J. Aprajeeta, R. Gopirajah, C. Anandharamakrishnan, *J. Food Eng.*, **144**, 119 (2015).
35. H.Z. Tekin, M. Başlar, S. Karasu, M. Kilicli, *J. Food Process. Preserv.*, **41**, 1 (2017).
36. H. Darvishi, P. Mohammadi, M. Azadbakht, Z. Farhudi, *J. Agr. Sci. Tech.*, **20**, 249 (2018).
37. H.S. El-Mesery, M. Qenawy, Z. Hu, W.G. Alshaer, *Case Stud. Therm. Eng.*, **50**, 103451 (2023).
38. X. Man, L. Li, X. Fan, H. Zhang, H. Lan, Y. Tang, Y. Zhang, *Agriculture*, **14**, 182 (2024).
39. Ö. G. Kocabay, O. İsmail, I. Doymaz, *Period. Polytech-Chem.*, **68**, 253 (2024).
40. A. Wojdyło, A. Figiel, K. Lech, P. Nowicka, J. Oszmianski, *Food Bioprocess. Technol.*, **7**, 829 (2013).
41. Z. Sumic, A.T. Horecki, S. Vidovic, S. Jokic, R. Malbasa, *Food Chem.*, **136**, 55 (2013).

Biochemical, transcriptional and fluorescence spectroscopy analysis of fatty acids in seeds of camelina varieties in the organic intercropping system

M. Marcheva^{1*}, M. Petkova², V. Slavova³, V. Popov⁴

¹ Department of Crop Science, Faculty of Agronomy, Agricultural University Plovdiv, 12 Mendeleev Blvd., Plovdiv 4000, Bulgaria

² Department of Microbiology and Environmental Biotechnology, Faculty of Plant Protection and Agroecology, Agricultural University Plovdiv, 12 Mendeleev Blvd., Plovdiv 4000, Bulgaria;

³ Bulgarian Academy of Sciences, Maritsa Vegetable Crops Research Institute, Agricultural Academy Plovdiv, Bulgaria

⁴ Department of Agroecology and Environmental Protection, Faculty of Plant Protection and Agroecology, Agricultural University Plovdiv, 12 Mendeleev Blvd., Plovdiv 4000, Bulgaria

Received: October 19, 2024; Revised: May 15, 2025

Intercropping involves the cultivation of two or more crops in the same field at the same time to improve yield per unit area by using resources or ecological processes that would otherwise not be used by a single crop. Camelina (*Camelina sativa* L.) is traditionally grown as an oilseed crop for producing vegetable oil and animal feed and is studied for its exceptional level of omega-3 fatty acids (up to 45%). The seeds contain 38 to 43% oil and 27 to 32% protein. The aim of this study is biochemical evaluation of the potential of this oil crop under organic cultivation of three varieties of camelina alone K1 (Luna), K2 (Lenka) and K3 (Local Bulgarian landrace) and co-cultivated with leguminous crops - pea (*Pisum sativum* L.) and vetch (*Vicia sativa* L.). Biochemical analysis showed that the percentage of oil content decreased in co-cropping with leguminous crops in variant K1 but increased in variants K2 and K3 from 33.1 - 35% to 37 - 38.9%. Fatty acid levels and gene expression profiles for the *fad6* gene associated with the synthesis of fatty acids (FA) were examined in three oilseed camelina cultivars that have utility for cultivar development in our spring camelina breeding program. The biochemical analyses of monounsaturated fatty acids as omega-9 oleic acid in camelina seeds show an increasing trend when intercropping was applied with vetch and pea. The most significant increase was observed in polyunsaturated fatty acids as linoleic C18:2 and linolenic acids C18:3 profiles in all three variants and co-cultivation with vetch. As a result of transcriptional analysis, the expression of *fad6* in camelina co-grown with vetch was 5 times higher compared to control plants grown alone. The application of a mobile fiber-optic system for qualitative biochemical and transcriptional analysis is demonstrated. The spectral distribution of the emission fluorescence signal depends on expression in camelina. In camelina grown with peas and grown alone, a clear correlation was observed. The intensity of the fluorescence signal directly depends on the content of monosaturated fatty acids. Correlations were observed, except in the spectral distribution of the fluorescence signal and in its intensity when growing camelina alone and in combination with peas. When grown alone, the distribution of the signal is better compared to representatives grown in combination with peas and vetch.

Keywords: *Camelina sativa* L., biochemical analysis, transcriptional analysis, fluorescence spectroscopy analysis, intercropping

INTRODUCTION

Camelina (*Camelina sativa* (L.) Crantz) is an oilseed crop from the *Brassicaceae* family, and it is important for food, feed, and industrial uses. *C. sativa* possesses several agronomic properties such as resistance to insects and easy adaptation to any climatic conditions, the only limitation for

its cultivation being heavy clay or waterlogged soils. Seed yields and oil content were highly variable depending on the environment and it outdid rapeseed in trials under identical drought conditions [1].

Considering the climate changes, good drought tolerance has been pointed out as one of

* To whom all correspondence should be sent:

E-mail: marina.marcheva@gmail.com

the advantages of this crop [2, 3]; especially during flowering, drought can reduce plant growth and development [4]. It shows good cold survival as it can germinate at low temperatures and the plants can tolerate freezing [5], although this has not been fully characterized for all stages of development and varieties. For some genotypes, the crop has been observed to survive low temperatures without damage [6].

The plant provides a high-value feed with sufficient residual lipid content (5–10%) that has a rich protein profile similar to soybean meal [7]. The main content of the seeds of this crop is oil (40%) [8, 9]. Many studies have shown that the oil plays a role in reducing cholesterol and inflammatory potential due to the increased content of α -linolenic (omega-3) and linoleic (omega-6) fatty acids, as well as bioactive compounds such as tocopherols and phenols [10]. The camelina crop is studied for its extremely high level (up to 45%) of omega-3 fatty acids, which is unusual in plant sources [7]. Over 50% of the fatty acids in cold-pressed camelina oils are polyunsaturated - omega-3 fatty acids, alpha-linolenic acid, gamma-tocopherol, and linoleic acid. The oil is also very rich in natural antioxidants, such as tocopherols, which makes it extremely stable and very resistant to oxidation and rancidity. It contains 1 - 3% erucic acid and the vitamin E content of camelina oil is approximately 110 mg/100 g [11]. It is very suitable for use as frying oil, as it has an almond-like taste and aroma.

Camelina has recently been grown because of its potential as a biofuel and biolubricant [5]. Studies show that camelina-based jet fuel reduces net carbon emissions by about 80% [12]. The US Navy selected it as the feedstock for its first aviation biofuel test and successfully operated an F414 static engine in October 2009 at Naval Air Station Patuxent River, Maryland [13]. Dutch organic farming company Waterland International and the Japanese Farmers' Federation reached an agreement in March 2012 to plant and grow camelina on 2,000 to 3,000 ha in Fukushima Prefecture. The health organization has approved oil as a healthy food. The plant is a valuable source of essential amino acids, especially sulfur-containing ones, which are generally lacking in leguminous crops, thus

representing an alternative source of protein for both humans and farm animals.

Camelina is approved as a food additive for cattle in the US, as well as an ingredient (up to 10% of the ration) in chicken feed for broilers and feed for laying hens. Several by-products have been extracted with significant crude protein content. Camelina is also used in cosmetics and cooking. The edible seeds can be sprinkled on salads or mixed with water to make an egg substitute.

According to Maitra *et al.* [14], intercropping is the agricultural practice of growing two or more different crops in the same field at the same time. The main objective of intercropping is the production of a higher yield per unit area by using resources or ecological processes that would not otherwise be used by a single crop. Multi-crop intercropping systems provide respective ecosystems with benefits due to their independent symbiotic capacity for nitrogen fixation (in the case of legumes) and nitrogen contribution to the next crop, remobilization of phosphorus by mycorrhizal and soil microorganisms, resulting in reduced nitrogen input and phosphorus with fertilizers and more rational use of energy, improving biodiversity and overall soil health.

From 2021, the Agricultural University in Plovdiv is a partner of several European countries in the SCOOP Project. This project is focused on organic farming systems intended to preserve the ecosystem and agricultural land integrity, biodiversity, as well as food and feed security. While camelina can potentially be grown anywhere in Europe, SCOOP companion crops will be identified locally according to the specific needs of stakeholders, the expectations of local farmers and traditional food. The purpose of the study is to evaluate the biochemical composition of oil, transcription of the *fad6* gene involved in the synthesis of very long fatty acids (VLFA) and fluorescence spectroscopy analysis of fatty acids in seeds of camelina cultivars grown on certified organic far alone and in intercropping with legumes peas (*Pisum sativum*) and vetch (*Vicia sativa*). In higher plants, polyunsaturated fatty acids (PUFAs) are synthesized by various FAD (fatty acid desaturases). FAD is a ubiquitous enzyme family and is responsible for introducing double bonds into the hydrocarbon chains of fatty acids [15]. They play an essential role in fatty

acid metabolism and maintain biological membranes in most creatures [16]. Biosynthesized α -linolenic acid is converted from linoleic acid by FAD genes. Linoleic acid and α -linolenic acid are so-called essential fatty acids (EFAs) in human bodies because of their ability to synthesize these compounds [16, 17]. Therefore, *fad6* is the key enzyme for producing linoleic acid and is also the speed-limiting enzyme for routes of ω -6 and ω -3.

Fluorescence spectral analysis allows non-invasive analysis, in a short time, with high sensitivity, without disturbing the integrity of the biological object. The optical properties of compounds in cereals and legumes are determined by energy structure of electrons in molecules, which includes both occupied and unoccupied electronic energy levels, as well as the energy levels of atomic vibrations in molecules. Fluorescence spectra of seeds of camelina cultivars allow obtaining important information for optimizing the yield and content of polyunsaturated fatty acids (PUFA) [18].

MATERIALS AND METHODS

Field experiments

Field trials were conducted on the certified organic field at the Agroecological Center of the Agricultural University - Plovdiv. The soil type is Mollic fulvisols – FAO, with a low humus content of 3.7% and neutral pH. A randomized complete block design was used for setting a small plot experiment on the effect of an intercropping system of camelina and protein crops, compared to a sole crop of the same species. Three genotypes of *Camelina sativa* – the Polish winter varieties Luna (K1) and Lenka (K2) and a local Bulgarian landrace (K3) were grown in two successive years -2022 and 2023 in a pure stand and combined with fodder pea (*Pisum sativum*) and vetch (*Vicia sativa*). In this study, we present the results from the spring cultivation in small plots of 10 m² (1.4 × 7.7 m). The sowing was executed with plot seeder Wintersteiger AG with 800 germinating seeds/m². Each variant of the sole crop or its combinations (Table 1) was set in three replications. Fertilization with approved for organic farming solid fertilizer - 30 kg/ha of active substance nitrogen was done before soil cultivation. Appropriate insecticides were

necessary as we observed a serious infestation of cabbage flea beetle (*Phyllotreta cruciferae*) on the field at the beginning of the vegetation. No significant environmental or biotic stress factors were observed during the vegetation of camelina in both years.

Plant material

During the flowering stage, 30 plants per variant and replication were marked according to stage. During maturation pods were collected at 10-day intervals, 10 up to 30 days after flowering (DAF), as shown in Figure 1. Seeds were harvested in liquid nitrogen and stored at -80°C for gas chromatographic analysis and RNA extraction in triplicate as was published by Petkova et al. [19].



Figure 1. Development stages of seeds maturation A) 10 DAF and B) 30 DAF.

Determination of oil and fatty acid profile by gas chromatography

At 30th DAF, oil was extracted from seeds with n-hexane using accelerated solvent extraction according to the methods of Haagensohn [19, 20] for oil content determination. One g of camelina seeds was dried for 4 h at 70°C. The seeds were ground in a coffee grinder with 3.5 g of diatomaceous earth, and samples were loaded into 10 ml stainless steel cells. Any remaining extraction cell void volume was filled with diatomaceous earth before extraction. The solvent containing extracted oil was collected in pre-weighed vials, and the solvent was evaporated to dryness with a stream of dry air (dew point of -70°C). Extracted samples were air-dried, and reground for a second extraction and the total oil recovery from the two extractions was recorded. Oil is reported as a percentage of seed dry weight. The seeds of camelina varieties (2 g) were subjected to quantitative and

qualitative analysis of the composition of fatty acids. The extraction of fatty acids from the seeds was performed with a 1 ml solution of esterification buffer (75 ml of hexane, 20 ml of chloroform and 5 ml of sodium methoxide in methanol) [21]. GC analysis was performed with a Hewlett-Packard gas chromatograph (model: HP5890 fitted with a 30 m FFAP capillary column (0.25 mm narrow aperture and 0.5 μm thick film). The fat content was determined by the residual method with a Soxhlet apparatus.

Real-time PCR analysis

Total RNA was extracted from 100 mg of control camelina leaves and leaves from camelina intercropped plants. First-strand cDNAs were reverse-transcribed from 1 μg each total RNA using a Hi-cDNA synthesis kit (Himedia, Mumbai, India). Gene-specific primers for *fad6* gene (5'-ATCACATAAGCCCAAGCATACCG-3' and *fad6*-Rv - 5'-TCGTCTTCATCAACCGCCATT-3') expression by Primer 5 software (Applied Biosystems, Foster City, CA, USA). Each 25 μl PCR reaction contained 12.5 μl 2 \times SYBR Green Mastermix (- iTaq Univer SYBR Green SMX 500, BioRad, Hercules City, CA, USA), 0.5 μl 10 μM each primer, 1 μl of each first-strand cDNA template, and 10 μl dd H₂O. The PCR reaction was performed in a real-time PCR detector (Bio-Rad Laboratories, Hercules City, CA, USA) with Opticon Monitor 3 software (Bio-Rad Laboratories). The following thermal cycling profile was used: 95°C for 10 min; 35 cycles of 95°C for 15 s and 56°C for 1 min; and 95°C for 15 s, 60°C for 1 min, and 95 °C for 15 s [22]. As an internal control to normalize all data actin expression was used [23]. Experiments were carried out with three independent biological replicates each containing three technical replicates [24]. The difference in mRNA expression was estimated using threshold cycles, by the 2 $^{-\Delta\Delta\text{CT}}$ method of Livak and Schmittgen [25].

Spectral measurements

The mobile fiber-optical spectral installation is designed specifically for the study of fluorescence signals for the rapid analysis of camelina seed samples. It includes the following components (Figure 2):

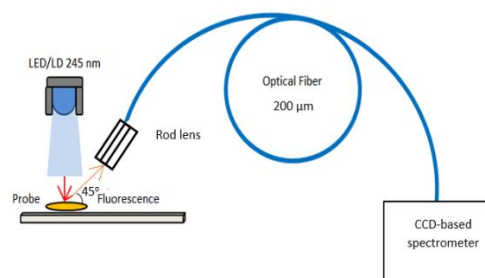


Figure 2. Mobile experimental installation used for fluorescence spectroscopy.

- Laser diode (LED) with emission radiation of 245 nm with a supply voltage in the range of 3V. It is enclosed in a hermetically sealed TO39-type metal case. The emitter current consumption is 0.02A, and its voltage drop is in the range of 1.9 to 2.4V. -6V is the minimum emitter voltage value.

- Rod lens consists of two connected Schott and Corning lenses with anti-reflective coatings that have different dispersion coefficients. It is of the achromatic doublet type. The chromatic aberration of one lens compensates for that of the other. This is due to the values of their radii. The forming optic has a diameter tolerance of - 0.005 mm.

- The multimode optical fiber has a core diameter of 200 μm . The optical fiber is of the type FG200LEA. It has a step index of the attenuation coefficient.

- The area of the quartz glass is 4 cm². Its optical properties include being transparent to visible light and ultraviolet and infrared rays. For this reason, it is observed that there are no inhomogeneities that scatter the light. The optical and thermal properties of quartz glass are superior to those of other types of glass due to its purity. Quartz glass has a very low light absorption coefficient.

- The sensitivity of the CMOS detector is in the range of 200 nm to 1100 nm. $\delta\lambda= 5$ is its resolution. Unlike widely used sensors, the profile of the detector sensor projections used in this study along the X and Y axes is designed to generate very small amounts of data.

The sample fluoresces after being irradiated by the LED. The emission signal is obtained at 45° from Rod Len, and the emission signal is generated. It is then transmitted through the optical fiber to the detector.

The fiber optic set-up used in this study has the following three unique advantages:

- Rod Len was used in the construction of the system. This lens was chosen for its high light transmission coefficient, which is due to the complete filling of the air gaps between the individual lenses included in its composition.
- An optical fiber and a Rod Len are precisely connected in a duralumin housing. This design achieves the optimum in laser diode imaging and fiber optic compilation, ensuring low levels of signal intensity loss.
- The emission fluorescence signal is obtained at 45°.

RESULTS AND DISCUSSION

Determination of total fat and fatty acid composition

Oil content in camelina seeds varies between genotypes and environmental conditions from 35 to 45% [26-29]. Our results correspond to these reports but remain far from the higher level of total crude fats. The low level of fertilization in our trial was chosen for better discrimination of the effect of the companion protein crop on the overall benefits of intercropping. While the yield of both crops is beneficial for the farmers [30], the seed oil content varies and is closer to the findings of Juodka that the crude fat content in seeds of camelina grown in Lithuania was around 36.84% [31]. Genotype reactions to poor nutrition regimes remain significant not only for the productivity of grains but also for their quality.

Differences between varieties are up to 4.8% - from 34.4% in the sole crop of Luna up to 39.2% for the local Bulgarian landrace. K3 has better

productivity [30] and a higher percentage of total crude fats in all variants with a slight decrease (only 1.1%) for the camelina pea combination. This intercropping is more suitable for K2 cultivation where an increase of 1% is observed. The oil content of the Luna seeds is higher when accompanied by vetch (37.9%) than for the variant of camelina and fodder pea (33.5%).

Camelina oil has saturated fatty acids (FA) such as palmitic acid (PA; 16:0) and stearic acid (SA; 18:0) and unsaturated – monounsaturated oleic acid (OA; 18:1) and polyunsaturated as linoleic acid (LA; 18:2) and α -linolenic acid (ALA; 18:3). This omega-3 fatty acid is needed as a substitute for the human eicosapentaenoic acid (EPA) and docosahexaenoic acid (DHA) [32]. The results of the percentage content of fatty acids with a carbon chain length of C12 to C24 in the oil obtained from the seeds of three varieties of camelina K1 (Luna), K2 (Lenka) and K3 (Local) grown as sole-crop and compared to intercropping with leguminous crops in our certified organic field are presented on Table 2.

Lauric acid C12:0 is not contained in K3 but is present in low concentrations (0.1%) in the oils of all the other variants. The amount of myristic acid C14:0 does not exceed 0.1% in all tested seeds, which makes the oil less harmful to human health. The percentage content of palmitic acid C16:0 is higher in K1 (6.0%) and remains up to 5.7% in the other variants. Fat is an essential macronutrient of the human diet and vegetable oils represent a more consumed fat [33]. The effects of saturated fatty acids (C12:0 till C18:0) have been the focus on the reduction of cardiovascular diseases, obesity, and cancer prevention [34, 35].

Table 1. Total crude fat content in the mature seeds of three varieties of camelina K1 (Luna), K2 (Lenka) and K3 (Local Bulgarian landrace) grown alone and co-cultivated with leguminous crops - pea (*Pisum sativum* L.) and vetch (*Vicia sativa* L.), %.

№	Genotype	Camelina	Camelina	Camelina	Average for the genotype
		sole crop	pea	vetch	
1	Luna K1	34.4	33.5	37.9	35.3
2	Lenka K2	35.1	36.1	35.1	35.4
3	BG landrace K3	39.2	37.9	38.9	38.7
4	Average for the crop system	36.2	35.8	37.3	36.5

Table 2. Fatty acid composition (FAC) of the camelina oil from sole-crop and intercropping camelina Polish varieties K1 – Luna, K2 – Lenka and K3 – local Bulgarian landrace with pea and vetch, %.

FAC, %	1	2	3	4	5	6	7	8	9
	K1	K2	K3	K1+ pea	K2+ pea	K3+ pea	K1+ vetch	K2+ vetch	K3+ vetch
12:0	0.1	0.1	0.0	0.1	0.1	0.1	0.1	0.1	0.1
14:0	0.1	0.1	0.1	0.1	0.1	0.1	0.1	0.1	0.1
16:0	6.0	5.7	5.7	5.7	5.5	5.7	5.6	5.5	5.7
16:1	0.1	0.1	0.1	0.1	0.1	0.1	0.1	0.1	0.1
18:0	1.9	2.1	2.3	1.9	2.0	2.3	1.9	2.1	2.3
9-18:1	14.1	17.3	18.3	14.9	17.2	17.2	14.6	17.7	18.3
11-18:1	1.0	0.9	0.9	0.9	0.9	0.9	0.9	0.9	0.9
18:2	20.6	19.9	18.4	21.0	19.7	18.5	20.5	19.5	19.0
18:3	31.5	30.2	32.9	31.7	31.0	34.1	32.5	30.9	35.6
20:0	1.5	1.5	1.4	1.4	1.5	1.3	1.4	1.5	1.4
20:1	15.1	15.3	14.2	14.8	15.3	13.9	15.0	15.2	16.0
20:2	1.9	1.6	1.3	1.9	1.6	1.4	1.9	1.5	1.3
20:3	1.1	0.9	0.9	1.1	1.0	1.0	1.1	1.0	0.9
22:0	0.3	0.3	0.3	0.3	0.3	0.3	0.3	0.3	0.3
22:1	3.7	3.1	2.5	3.4	3.1	2.5	3.4	3.0	2.5
24:0	0.2	0.2	0.1	0.1	0.2	0.1	0.2	0.2	0.1
24:1	0.7	0.6	0.6	0.6	0.6	0.6	0.6	0.6	0.6

Polyunsaturated fatty acids include oleic, linoleic, and α -linolenic acids. Oils rich in oleic acid are suitable for heat treatment and have a long shelf life. In the present experiment, variation in oleic acid content is due mostly to genotype (around 14% for K1 up to 18.3% for K3) and to a lesser extent to the combination with vetch or fodder pea in our organic field. The cropping system has a lower impact on the linoleic C18:2 content and variations are mainly due to the variety. The most significant increase was observed in α -linolenic acids C18:3 profiles of the local Bulgarian landrace K3 when cultivated with vetch (up to 35.6%) and pea (34.1%) compared to the sole crop (32.9%). Its content is better also for the intercropping of the other two varieties Luna (K1) with vetch and Lenka (K2) with pea. Linolenic acid is a very valuable acid, but it oxidizes easily, which lowers the quality of food products during their storage. The oil with a high content of C18:3 was used for technical purposes and combustion.

The vetch as companion crop for K3 has a positive effect on the increase of eicosenoic acid C20:1. (Table 2).

Fad6 gene expression in the development seeds of camelina

Two PCR reactions were performed with 2 sample pairs of primers. The purified RNA does

not contain DNA; therefore, the obtained amplification curves are not due to contamination and the RNA is of the necessary quality to run the PCR reactions. Actin was chosen as the "housekeeping" gene because it is expressed equally in all stages of camelina seeds development. As a result, *fad6* expression in camelina K3 variety grown intercropping with vetch was 5 times higher compared to control self-grown plants (Fig. 3). A correlation was observed between levels and *fad6* gene expression across seed formation of K3 in the nine different cultivation plots. Positive correlation was detected in C18:3 and C20:1 fatty acids.

Fluorescence spectroscopy analysis of seeds of camelina

From the stated circumstances, it can be concluded that fluorescence spectroscopy finds application for the analysis of camelina. This allows obtaining essential information about changes in the chemical composition and expression of camelina plants under organic cultivation and co-cultivation with peas and figs. The three main advantages of fluorescence spectroscopy are that the method is fast, can be performed *in situ* under uncontrolled conditions, and does not require consumables when performing the analyses.

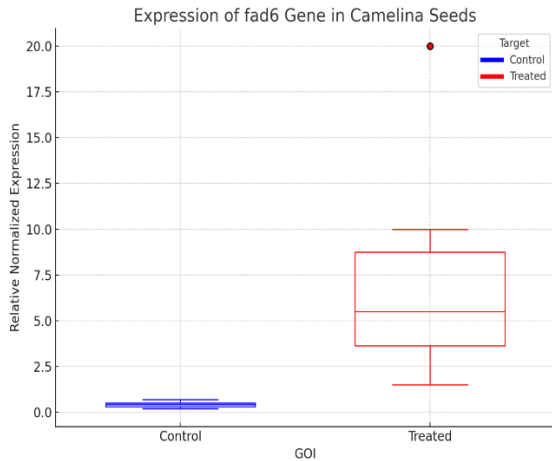


Figure 3. Comparison of *fad6* gene expression level between control self-grown plants and K3 variety grown in intercropping with vetch.

A literature survey was conducted to discover a similar research published by Slavova [24]. It turned out that until now the described experimental approach for analysis of camelina crops under organic cultivation and co-cultivated with pea and vetch is not known to have been implemented to conduct our experiment. Due to

this fact, we claim that for the first time, we applied fluorescence spectroscopy for the analysis of different camelina plant samples (alone and in intercropping variants) after harvest.

Figure 4 A) represents the spectral distribution of the emission fluorescence signal of K1, K1+pea and K1+vetch. A significantly stronger intensity of K1+vetch at 435 nm is observed, which is due to increased expression compared to K1 and K1+pea. The same result is confirmed by Figures 4 B and 5 A for the remaining two varieties K2 and K3, respectively.

The level of distribution of the emission signal in Figures 4 and 5 is dependent on the fatty acid content. The results of these three graphs show that camelina with a higher fatty acid content is best obtained if grown in combination with vetch. The highest level of fatty acid content is observed in K1+vetch. This result is presented in Figure 5B. Luna variety co-cultivated with vetch is the best of the three combinations for optimal obtaining of the highest fatty acid content.

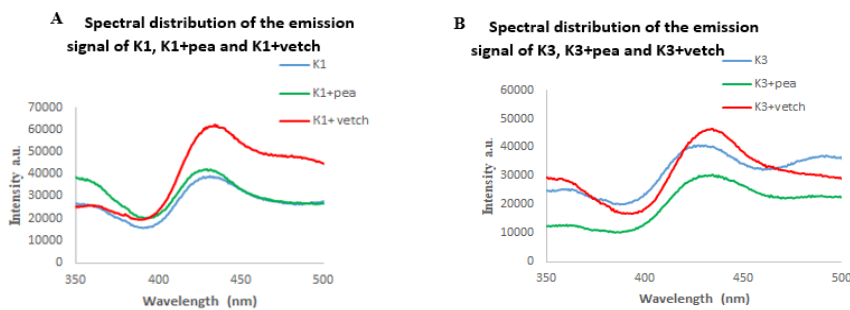


Figure 4. Spectral distribution of the emission signal of A) K1, K1+pea and K1+vetch and B) K3, K3+pea and K3+vetch

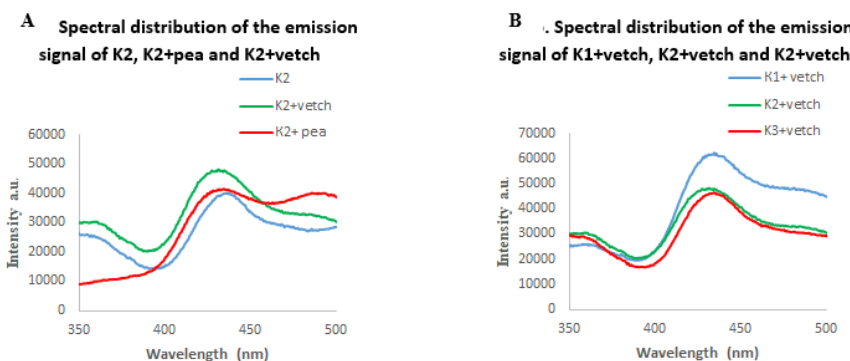


Figure 5. Spectral distribution of the emission signal of A) K2, K2+pea and B) K2+vetch and K1+vetch,

K2+vetch and K3+vetch

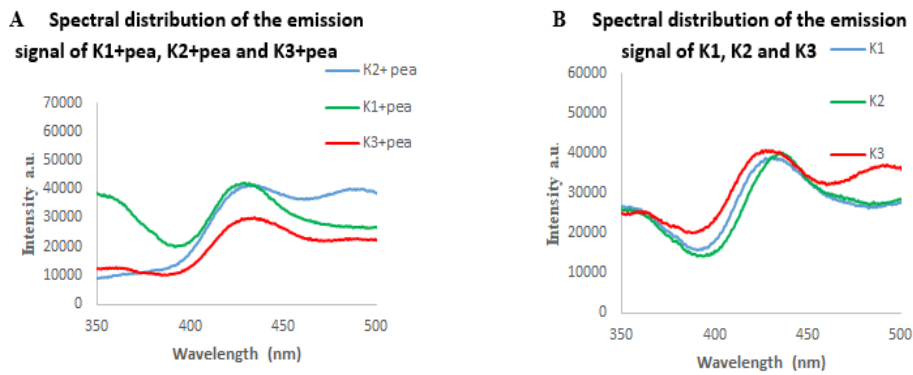


Figure 6. Spectral distribution of the emission signals of A) K1+pea, K2+pea and K3+pea and B) K1, K2, and K3.

A difference in the emission fluorescence signal of K1, K2 and K3 is presented in Figure 6 B. The spectral distribution for samples K1 and K2 is similar, but some differences in the intensities of the emission signal occurred. The difference in the emission wavelength shift between them and K3 is due to the different varietal characteristics. K3 has a more intense shift due to the tendency to increase the total crude fat content.

Figure 6 A presents the observed differences in the spectral distribution of the fluorescence signal and in its intensity when growing camelina alone and in combination with peas. Stability in signal propagation is observed in self-cultivation compared to camelina co-cultivated with pea and vetch. The presented spectral distributions of all tested materials are considered unique for each specific genotype. This can be considered as a basis for using the used installation for recognizing available camelina seeds in a non-invasive way with high accuracy. In this respect, it could be expected that seeds can be distinguished to confirm a closely related origin or genetically distantly related forms, the presence of inhomogeneous or stabilized selection material, and/or spectral definition of seeds of unknown origin. To confirm the application of fluorescence spectroscopy for the quantitative determination of fatty acids, it is necessary to deepen the studies on correlations in fatty acid measurements with spectral fluorescence analysis to confirm the possibility of

using the dependence between the quantitative content of fatty acids in camelina seeds and the spectral distribution and intensity of the fluorescence signal obtained by spectral analysis of seeds of a selected genotype.

CONCLUSIONS

The analyses of our results show variation between genotypes, with a higher total crude fat content observed in the local Bulgarian landrace (K3) compared to the Polish varieties Luna (K1) and Lenka (K2). A clear tendency for improvement in oil content in camelina seeds was established when applying intercropping with fodder pea or vetch. Vetch proved to be a better companion for Luna, while fodder pea was more beneficial for Lenka. Therefore, a personalized decision for intercropping should be made based on the specific camelina variety.

Polyunsaturated fatty acids dominated the oil profile in all variants. Intercropping camelina with vetch enhanced the levels of α -linolenic acid (C18:3) and eicosenoic acid (C20:1) in K3 compared to its sole-crop variant. The same trend of increased α -linolenic acid was also observed in Luna when co-cultivated with vetch. For Lenka (K2), the fatty acid values were similar in both intercropping combinations. These findings were further supported by gene expression analysis, where the *fad6* expression in K3 intercropped with vetch was five times higher than in control plants grown in sole cropping. A positive correlation was observed between *fad6* expression levels and the content of α -linolenic

acid (C18:3) and eicosenoic acid (C20:1) in K3 across the different cultivation plots.

Fluorescence spectral analysis of camelina seeds revealed a correlation between the spectral characteristics (intensity and distribution of the fluorescence emission signal) and the content of monounsaturated fatty acids. Specifically, signal intensity was higher in seeds with elevated monounsaturated fatty acid content. For instance, K1 grown with vetch showed a stronger fluorescence signal at 435 nm, corresponding to higher FA levels. Notably, camelina grown in sole cropping showed more stable and clearly distributed emission signals compared to intercropped variants, suggesting that intercropping can influence seeds' biochemical composition and thus their spectral profiles.

In the future, this observed correlation between fluorescence spectral characteristics and fatty acid content could be further developed into a rapid, non-invasive method for screening camelina seed quality and biochemical composition under different organic cropping systems.

Acknowledgement: Financial support from CORE Organic ERA-NET and the Bulgarian National Science Fund (BNSF) by the project KP - 06-DO 02/4 is gratefully acknowledged.

REFERENCES

1. E.J. Murphy, in: T.A. McKeon, D.G. Hayes, D.F. Hildebrand, R.J. Weselake (eds.), *Industrial Oil Crops*, AOCS Press, Urbana, IL, USA, 2016, p. 230.
2. J. Zubr, *Ind. Crops Prod.*, **6**, 119 (1997).
3. R.K. Gugel, K.C. Falk, *Can. J. Plant Sci.*, **86**, 1058 (2006).
4. J. Vollmann, A. Damboeck, A. Eckl, H. Schrems, P. Ruckenbauer, in: J. Janick (ed.), *Progress in New Crops*, ASHS Press, Alexandria, VA, USA, 1996, p. 362.
5. D.T. Ehrensing, S.O. Guy, Camelina, Oregon State University Extension Service, Corvallis, OR, USA, EM 8953-E (2008).
6. A. Francis, S.I. Warwick, *Can. J. Plant Sci.*, **89**, 810 (2009).
7. D.H. Putnam, J.T. Budin, L.A. Field, W.M. Breene, In: J. Janick, J.E. Simon (eds.), *New Crops*, Wiley, New York, NY, USA, 1993, p. 322.
8. V.K.S. Shukla, P.C. Dutta, W.E. Artz, *J. Am. Oil Chem. Soc.*, **79**, 969 (2002).
9. C. Boyle, L. Hansen, C. Hinnenkamp, B.P. Ismail, *J. Am. Oil Chem. Soc.*, **95**, 1062 (2018).
10. J.G. Crowley, A. Fröhlich, The composition and use of camelina, Teagasc, Dublin, Ireland, 1998.
11. R. Hofer (ed.), *Sustainable solutions for modern economics*, Royal Society of Chemistry, Cambridge, UK, 2009.
12. S. De Jong, K. Antonissen, R. Hoefnagels, L. Lonza, M. Wang, A. Faaij, M. Junginger, *Biotechnol. Biofuels*, **10**, 64 (2017).
13. K.A. McVay, P.F. Lamb, Camelina Production in Montana, Field Crops No. D-16, Montana State University Extension, Bozeman, MT, USA, 2007.
14. S. Maitra, J.B. Palai, P. Manasa, D.P. Kumar, *Int. J. Agric. Environ. Biotechnol.*, **12**, 45 (2019).
15. A.K. Singh, S.K. Raina, M. Kumar, L. Aher, M.B. Ratnaparkhe, J. Rane, A. Kachroo, *Plant Mol. Biol.*, **110**, 218 (2022).
16. S. Zhu, Z. Zhu, H. Wang, L. Wang, L. Cheng, Y. Yuan, D. Li, *Sci. Hortic.*, **239**, 170 (2018).
17. H.G. Damude, A.J. Kinney, *Plant Physiol.*, **147**, 968 (2008).
18. X. Zhu, D. Wang, N. Li, X.S. Sun, *ACS Omega*, **2**, 8004 (2017).
19. M. Petkova, W.S. Chao, L. Cook, M. West, M. Rahman, M.E. Foley, *Plant Breed. Seed Sci.*, **72**, 32 (2015).
20. D.M. Haagenson, R.L. Brudvik, H. Lin, D.P. Wiesenborn, *J. Am. Oil Chem. Soc.*, **87**, 1358 (2010).
21. M.D. Zlatanov, G. Angelova-Romova, R. Antova, R.D. Dimitrova, B. Momchilova, M. Nikolova-Damyanova, *J. Am. Oil Chem. Soc.*, **86**, 875 (2009).
22. S. Lu, A.P. Smith, D. Moore, N.M. Lee, *Mol. Cell. Probes*, **24**, 320 (2010).
23. X. Zhao, Y. Shen, W. Hu, J. Chen, T. Wu, X. Sun, W. Chen, *Mol. Immunol.*, **68**, 647 (2015).
24. V. Slavova, E. Ropelewska, K. Sabanci, *Eur. Food Res. Technol.*, **249**, 3245 (2023).
25. K.J. Livak, T.D. Schmittgen, *Methods*, **25**, 408 (2001).
26. Y. Jiang, C.D. Caldwell, K.C. Falk, R.R. Lada, D. MacDonald, *Agron. J.*, **105**, 1852 (2013).
27. S.S. Malhi, E.N. Johnson, L.M. Hall, W.E. May, S. Phelps, B. Nybo, *Can. J. Soil Sci.*, **94**, 47 (2014).
28. B. Moser, *Lipid Technol.*, **22**, 273 (2010).
29. E. Ropelewska, K.J. Jankowski, *OCL*, **27**, 46 (2020).
30. M. Marcheva, J. Jordanov, G. Stanchev, P. Zorovski, in: Book of Abstracts of V. Balkan Agricultural Congress, Edirne, Turkey, 23 (2023).
31. R. Juodka, R. Nainienė, V. Juškienė, R. Juška, R. Leikus, G. Kadžienė, D. Stankevičienė, *Animals*, **12**, 295 (2022).
32. A.C. Rustan, C.A. Drevon, *eLS* (2005).

33. J. Aranceta, C. Perez-Rodrigo, *Br. J. Nutr.*, **107**, S22 (2012).
34. G. Assmann, P. Buono, A. Daniele, E. Della Valle, E. Farinaro, G. Ferns, V. Krogh, D. Kromhout, L. Masana, J. Merino, *Nutr. Metab. Cardiovasc. Dis.*, **24**, 1300 (2014).
35. N.A. Berger, *Ann. N.Y. Acad. Sci.*, **1311**, 76 (2014).

Determination of boundary conditions from experimental data for computational fluid dynamics simulations for phases change material solutions in the ground mass with emphasis on ground heat exchangers

K. V. Stefanova

Institute of Chemical Engineering, Bulgarian Academy of Sciences, Acad. G. Bonchev Str. Bl.103, 1113 Sofia, Bulgaria

Received: February 02, 2025; Revised: May 20, 2025

The main disadvantage of horizontal ground heat exchangers is that the area above them cannot be used for agricultural purposes, and the shallow location of the horizontal pipes leads to frequent temperature fluctuations. This can be overcome by appropriate solutions for a thermal storage regulation unit. The purpose of this work is: 1) systematization of research on ground heat exchangers with phases change material by means of pictorial illustrative table; 2) analysis of the results for the measured temperatures for the ground depths of 2 m and 6 m, for the summer period and determination of the thermal conductivity of the researched soil layer. The results are shown graphically. This data is suitable for running computational fluid dynamics simulation and the resulting temperature variation data can be entered as input data for the thermal energy storage based of phases change material low-paraffin waxes type.

Keywords: Ground source heat pump (GSHP), ground heat-exchanger (GHE), thermal energy storage (TES), phases change material (PCM), paraffin wax, renewable energy sources (RES)

INTRODUCTION

The use of alternative and sustainable ways with the participation of renewable energy sources for air conditioning of homes, industrial buildings and agricultural sites gives an advantage in two aspects: reducing the impact on the environment and saving primary energy. Geothermal energy combined with geothermal installations can undoubtedly contribute to this goal [1-3]. Geothermal installations significantly save primary energy, which also contributes to the environmental impact [4]. According to the statistical office of the European Union - Eurostat 2022 [5], from the total production of energy, the energy from renewable energy sources is different, as follows: Sweden - 62.6%, Finland - 43.1%, Latvia - 42.1%, Austria - 36.4%, Bulgaria - 17.0%, Malta - 12.2%. Geothermal energy is 1.22% of the total acquired energy sources in Bulgaria in 2021 [6].

In the last few decades, considerable efforts have been made to develop geothermal systems for building installations, as well as to solve the various problems in their design. Extensive studies have been conducted in different countries on the use of these systems [7-9], for modeling of the plant components [10], for capacity control [11], for unbalanced load balancing [11], for thermal efficiency optimization [8] and others. In a review, for the use of heat pumps it was found that about 2 to 4 GW of thermal energy could be obtained

[12]. In the case of vertical ground heat exchangers, the main disadvantage is the initial investment for drilling, difficult access to the pipes at depth in case of depreciation or need for repair. It should also be noted that the lifetime of some materials for geothermal heat pumps is up to 35 years [13]. On the other hand, at the horizontal ground heat exchanger (HGHE) by good research and design, only climatic conditions remain difficult to predict and compensate for their negatives [14, 15]. For example, with a small temperature difference to the ground, the size of the heat exchanger will be very large [16, 17] or expensive [18]. Some of the physical complexities of horizontal ground heat exchangers are related to the annual behavior of shallow soil areas, which is affected by temporal climate changes over a year [19, 20].

A key point for shallow-placed systems is that site-specific measurements of soil temperature are required to correctly determine the initial boundary conditions. In study [21], an example temperature map at different depths is presented, in which the variations of ground temperature tend to be independent of the ambient air temperature at depths greater than 5 m. Compilation of such ground temperature maps is possible by mathematical modeling and simulations, but the best option is to measure the temperature of the ground *in situ*, as argued in study [22]. Another disadvantage is the need for a free area exposed to direct sunlight, with an area about 2.5 times larger than that of the

* To whom all correspondence should be sent:

E-mail: kstambolieva@abv.bg,
k.stefanova@iche.bas.bg

building to be heated. Statistics show that the typical shading coefficient (SCC) for a tree providing light shade is 0.55, and for a tree providing heavy shade is 0.25 [23].

In study [24] it is estimated that the performance of the horizontal ground heat exchanger at 6 m depth using a tank of 0.6 - 0.9 m in diameter filled with PCM suspended in water is an alternative to the conventional vertical ground heat exchanger. The study of the lithological construction and the calculation of the heat transfer of the ground mass at a given place is of extreme importance for the design and modeling of geothermal installations [25]. The precise results for the coefficient of thermal conductivity and the thermal resistance are also necessary for the introduction of boundary conditions in mathematical modeling and computer simulations. The thermal response test method is suitable for determining the thermal conductivity of soil layers in the presence of a constant temperature source [26, 27].

The purpose of this work is: 1) review and systematization of research on ground heat exchangers with PCM; 2) selection of a depth for measuring the temperature in the ground suitable for a study of ground heat exchangers with participation of PCM; 3) analysis of the results for the measured temperatures for the ground depths of 2 m and 6 m, for the summer period and determination of the thermal conductivity of the researched soil layer.

RESEARCH FOR RENEWABLE THERMAL STORAGE IN THE GROUND MASS, GROUND HEAT EXCHANGER AND PHASES CHANGE MATERIAL

In the technical characteristics of geothermal installations, data on the cooling of the ground mass over time, as well as on heat recovery measures, are rarely provided. In order to ensure that the geothermal system will be a system with renewable energy sources and environmentally friendly, effective and carefully selected measures are needed to recover the heat in the ground mass.

Solutions using excess heat from solar systems are proposed in scientific circles, including geothermal installations with heating of the adjacent soil [27-29]. Trillat-Berdal *et al.* (2006) [30] "injected" excess heat into the ground through a borehole heat exchanger with a propylene glycol carrier and measured the warming of the surrounding ground mass. Experimental data on terrestrial-solar heat storage are also presented by Georgiev *et al.* (2020) [31].

Other researchers propose the use of combined approaches with solar sources and additional

elements filled with suitable materials, for example, phase change materials for heat storage [32]. These measures will prevent excessive warming of the land mass and maintain the heat balance for the cooling process on hot days. In [33] Mohanraj *et al.* (2021) present the production of solar pure water due to condensation with the participation of phase change materials and a heat pump.

On the other hand, more and more often, mathematical modeling and software simulations are used to generate an effective solution, by optimizing existing technologies or predicting innovations [34]. Such theoretical studies are also performed with modern computer simulation packages for computational hydrodynamics, as computational fluid dynamics (CFD) [35, 36]. The simulation of two-phase flows associated with a phase change is presented in studies [37, 38]. The heat conduction outside the heat exchanger can be represented by the model of a cylindrical source surrounded by a homogeneous medium with constant properties, in this case it is the ground [39-41].

Wang *et al.* (2014) [42] have conducted a numerical simulation of heat transfer for three models with grout and soil. The results show that the ground area can be effectively reduced with phase change materials such as backfill. Increasing the efficiency of heat exchange in the ground, as well as simulating the distance and storage volume of the drilling rigs, are also presented, through the transient system simulation (TRNSYS) program [43].

The thermal energy storage (TES) based on phase change material is one of the effective strategic technologies for balancing the heating flux and cooling flux [44, 45]. Phase change material in ground source heat pump can be used in all elements of installations at heating, at cooling and at power generation [46, 47]. The right PCM types - paraffin wax, non-paraffin organics, hydrated metallic salts [48] will lead to a reduction in the total length of the borehole, which is equivalent to a reduction in the investment cost of setting up the system. For GSHP applications, organic PCM like paraffin is the most common choice [49, 50]. The low-paraffin waxes (L-PW) are presented with a cooling application, but use for ground heat exchange would be suitable to compensate for thermal fluctuations over time [50-53].

The idea for a cylindrical heat exchanger with PCM is presented in [55]. Pardiñas *et al.* (2017) [56] proposed conductive baffles in the tank. In Pagkalos *et al.* (2020) [57] the heat exchanger is immersed in paraffin PCM. The GSHP efficiency is improved due to natural convection of water and additional load capacity provided by PCM in underground

thermal battery, as reported in [58]. PCM capsules in storage tank with a solar hot water heating system are placed between heat pump and ground heat exchanger [59]. In Qian *et al.* (2020) [60] specifications of ground heat exchange are as follows: borehole diameter 0.133 m, fluid flow rate 0.732 kg s^{-1} , thermal conductivity of HDPE pipe 0.4

$\text{W m}^{-1} \text{ K}^{-1}$, soil thermal conductivity $2.96 \text{ W m}^{-1} \text{ K}^{-1}$, shank space 0.042 m . Some studies investigated PCM as grout, [49, 50]. When PCM is added to the grout of vertical ground heat exchange, the length of the pipes is reduced and the heat pump works more stably and efficiently [61].

Table 1. Position of phases changes material (PCM) in ground heat exchanger (GHE)

Position of PCM in GHE	Summary scheme	Description	References
In the center of the pipe		Double tubes	[61]
Outside of the pipe		Double tubes	[62]
Combinations of pipe		Triple tubes	[63]
		GHE with PCM pipes	[69-71]
Grout and PCM		Grout modified	[43, 45, 57, 59, 67-70]
Underground PCM storage tank		Cylindrical tank as thermal battery	[50]
		Cylindrical tank	[46, 72, 73]
		Panels tank (3m x 5m)	[73]
Soil and PCM		Soil modified with microencapsulated PCM	[74]
Increasing of the thermal conductivity of PCM		Conductive baffles in tank	[47, 63]
		Steel balls encapsulated with paraffin	[29, 50, 64, 75]

 - PCM
  - Fluid flow
  - Grout
  - Grout and PCM
  - Soil
  - Thermal conductivity

In Righetti *et al.* (2020) [62] the 70 °C paraffin wax included in three 3D aluminum periodic structures is investigated for purposes of a latent heat storage tank. The paraffin with 20% Cu nanoparticles in the blade shape showed a notable potential to absorb thermal energy from the heat transfer fluid and decrease the outlet water temperature [49]. The soil and PCM backfill with low and high phase change temperature should be used for summer and winter modes [63, 64]. The principal positions of PCM in geothermal installations are given in Table 1.

The researchers of study [65] looked at PCM in the center of the heat exchanger tubes. Other studies were with PSM around the tubes [66]. In study [67] three concentrically arranged tubes are used as the PSM inter layer and were surrounded by the heat transfer tubes.

The filling mass around the pipes, the so-called grout, can also be replaced by PCM or partially modified with PSM [48, 49, 61, 63, 71-74]. Some researchers use tanks with PCM as a separate module to the systems for geothermal installations. These tanks may consist of concentric tubes [49] or be multi-tube in cylindrical tanks [51, 75, 76] and panel type tanks [77]. The surrounding ground mass is also modified with PSM [79]. Some of the researchers try to propose solutions and variations with the participation of additional materials and structural elements to increase the conductivity of the environment [32, 52, 79].

The following important conclusions have been drawn in [80] for the horizontal ground heat exchanger as a flat-panel installed 1–1.5 m under the ground surface: the use of PCM in proximity or coupled directly with the horizontal ground heat exchanger seems to work better than solutions with greater distances or with PCM added to the backfill material. The use of PCM in addition to the flat-panel horizontal ground heat exchanger allows to obtain an improvement in heat pump performance with a consequent energy saving of about 10%. Consequently, a reduction of the horizontal ground heat exchanger field size can be obtained for the same energy consumption. The installation of the PCM has been considered as a thin sheet of material of 5 mm close to the flat-panel heat exchanger, this sheet can be in direct contact with the HGHE, or it can be moved far from heat exchange surface.

Studies have been found showing the horizontal ground heat exchanger to be competitive with the vertical ground heat exchanger if phase change materials are included. The number of works in this

direction are few and in most cases without specific studies on the temperature and conductivity of the ground mass.

RESULTS FOR THE MEASURED TEMPERATURES FOR THE GROUND DEPTHS OF 2 M AND 6 M FOR THE SUMMER PERIOD AND DETERMINED THERMAL CONDUCTIVITY OF THE SOIL LAYER

Thermal characteristics can be calculated using the thermal response test method [25, 26]. The thermal conductivity λ_t of the ground is given by the equation for an interpolated straight line α as the slope *versus* duration τ of α in a plot of the evolution of the temperature T *versus* the logarithm of time:

$$T = \alpha \ln(\tau) + n \quad (1)$$

$$\lambda_t = \frac{Q_{GSR}}{4 \pi H \alpha} \quad (2)$$

where T - ground temperature at 2 m depth [°C]; α - an interpolated straight line; τ - duration in 72 h [h]; Q_{GSR} - the average value of global solar radiation (GSR) as heat power [W/m² per hour]; H - depth [m]. The purpose of our study is to search for suitable data from measured values of the temperature in a soil layer at a depth of 2 m for the summer period, from which to estimate the thermal conductivity of the soil layer at a depth of 6 m by the thermal response test method. This will allow theoretical calculations to be made by CFD method for a tank full of L-PW waxes at a depth of 2 m, which can be considered as a low-temperature heat source TES [81, 82].

For this purpose, ground temperature measurements were carried out with dataloggers placed at a depth of 2 m and 6 m, with a temperature measurement interval of 1 h, in a private property in the Gorna Banya area, Sofia, Bulgaria. Such an established interval at the depth of 2 m is for the period 27.08 - 16.10.2023, when temperatures were measured from 16.9 °C through 17.3 °C to 16.9 °C, Fig. 1.

The average temperature for this period of 51 days was 17.15 °C. Fig. 1 shows the obtained temperature data for depths of 2 m and 6 m for an interval of 51 days of the summer season, in the Gorna Banya area, Sofia, Bulgaria. For the measured temperature values for 6 m depth, it was calculated that the regression dependence is 0.2618, responsible for thermal conductivity of the soil layer between 2 m and 6 m depth, using the thermal response test method calculated for the period 30.08 - 10.10 2023 in Sofia, Fig. 2.

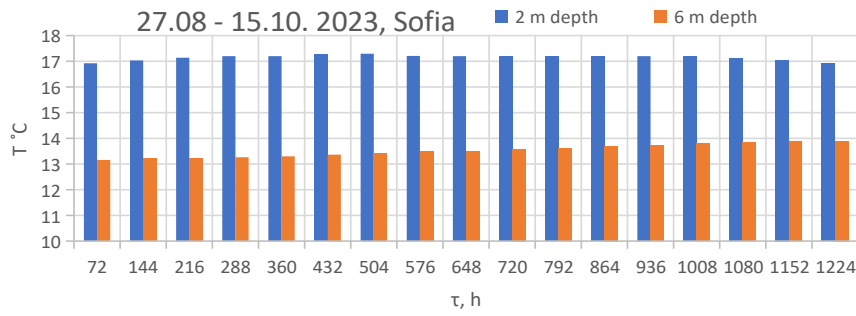


Figure 1. Temperature data obtained from dataloggers placed at depths of 2 m and 6 m for an interval of 51 days during the summer season, in a private property in the Gorna Banya area, Sofia, Bulgaria

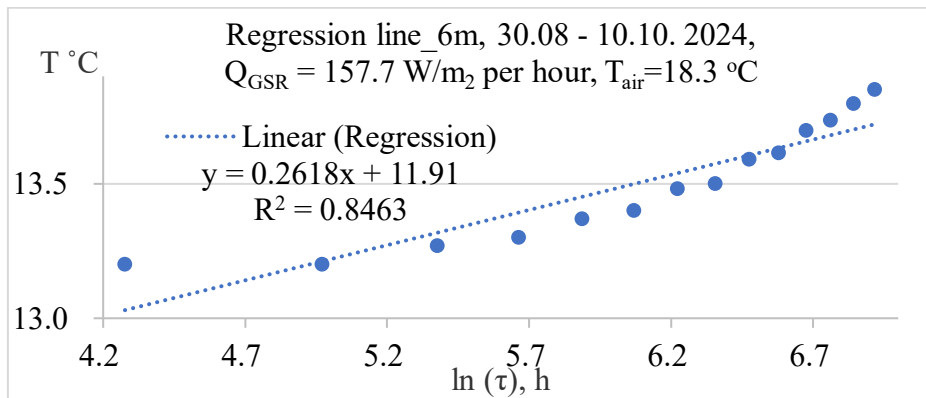


Figure 2. Regression line for 6 m depth by thermal response test method

The average air temperature was 18.3 °C and the average sun ray Q_{GSR} was 157.7 W/m² per hour [84]. Therefore:

$$\lambda_t = Q_{GSR} / 4 \cdot \pi \cdot H \cdot 0.2618 = 7.99 \text{ W/m K} \quad (3)$$

These data are suitable for conducting CFD simulations as the obtained temperature variation data can be entered as input data for the thermal energy accumulator playing the role of a low-temperature permanent source based on phase change material as L-PW waxes and make predictions for charging the ground layers with heat power at a depth of 6 m.

CONCLUSIONS

The heat balance in geothermal energy is a key to the long-term use of this so-called renewable energy source. The main disadvantage of geothermal installations is that the ground cools over time and needs compensation for heat losses from other renewable sources. The literature review points to thermal storage as a solution to temperature fluctuations in GSHP and the different location of PCM in ground heat exchangers is illustrated.

The study shows that horizontal ground heat exchangers with PCM are competitive with vertical ground heat exchangers. A disadvantage of horizontally located heat exchangers in the ground mass is that the area above them cannot be used for

agricultural purposes, and the shallow placement of the horizontal pipes leads to frequent temperature fluctuations.

Applications of phase change materials in geothermal systems are relatively new ideas and not well studied. The small number of studies testified to the lack of information on horizontal heat exchangers with PCM and provided the basis for starting a project "Research on the optimization of geothermal installations, including phase change modules as a renewable source of thermal energy by computational methods of fluid dynamics".

For the purpose of the project the temperature in the ground mass at a depth of 2 m and 6 m for the summer period was measured. From the obtained data, the temperature conductivity of the specific place for a depth of 6 m was determined, as well as the boundary conditions were specified for the CFD simulation of a reservoir with L-PW waxes proposed as a heat accumulator, temperature compensation and low-temperature heat source placed at a depth of more than 2 m.

Acknowledgement: This work is supported by The National Science Fund under Contract № KII-06-M67/4, 13.12.2022.

REFERENCES

1. P. A. Østergaard, N. Duic, Y. Noorollahi, H. Mikulcic, S. Kalogirou, *Renewable Energy*, **146**, 2430 (2020).
2. W. Chu, N. Duić, Q. Wang, *Energy Storage and Saving*, **2**, 1, 325 (2023).
3. R. Cunha, P. Bourne-Webb, *Renewable Sustainable Energy Rev.*, **158**, 112072 (2022).
4. G. Hou, H. Taherian, Y. Song, W. Jiang, D. Chen, *Renewable and Sustainable Energy Reviews*, **154**, 111830 (2022).
5. https://ec.europa.eu/eurostat/databrowser/view/nrg_ind_ren/default/table?lang=en (last update: 20/07/2023).
6. <https://www.nsi.bg/en/content/4201/renewables> (11.01.2024).
7. S. Maddah, M. Goodarzi, M. Safaei, *Alexandria Eng. J.*, **59**, 6, 4037 (2020).
8. X. Yu, X. Zhai, R. Wang, *Energy Convers. Manage.*, **51**, 11, 2162 (2010).
9. A. Pertzborn, G. Nellis, S. Klein, *HVAC&R Research*, **17** (2), 174 (2011).
10. M. Alavy, H. Nguyen, W. Leong, S. Dworkin, *Renewable energy*, **57**, 404 (2013).
11. D. Garber, R. Choudhary, K. Soga, *Building and Environment*, **60**, 66 (2013).
12. R. Lund, D. Ilic, L. Trygg, *J. Cleaner Prod.*, **139**, 219 (2016).
13. J. Han, M. Cui, J. Chen, W. Lv, *Geothermics*, **89**, 101929 (2021).
14. V. Somogyi, V. Sebestyén, G. Nagy, *Renewable and Sustainable Energy Reviews*, **68**, 934 (2017).
15. G. Hou, H. Taherian, Y. Song, W. Jiang, D. Chen, *Renewable and Sustainable Energy Reviews*, **154**, 111830 (2022).
16. H. Lei, C. Dai, *Delta*, **37**, 597 (2013).
17. N. Yildirim, S. Parmanto, G. Akkurt, *Renewable Energy*, **141**, 1080 (2019).
18. Z. Ma, L. Xia, X. Gong, G. Kokogiannakis, S. Wang, Z. Zhou, *Renewable Sustainable Energy Rev.*, **131**, 110001 (2020).
19. J. Muñoz-Criollo, P. Cleall, S. Rees, *Geomech. Energy Environ.*, **6**, 45 (2016).
20. D. Carder, K. Barker, M. Hewitt, D. Ritter, A. Kiff, *Published Project Report PPR302*, **1**, 1,1-114 (2007).
21. S. Rees, Woodhead Publishing, 2016, p.117.
22. S. Gehlin, B. Nordell, *ASHRAE Trans.* **109** (1), 151 (2003).
23. F. Moore, Environmental control systems: Heating, cooling, lighting. New York: McGraw-Hill, 1993. D. Garber: <https://www.buildingenclosureonline.com/blogs/14-the-be-blog/post/85233-comparing-solar-heat-gain-coefficients-shgc-and-shading-coefficients-sc>.
24. J. Warner, Feasibility Study of a Novel Ground Heat Exchanger using Phase-Change Materials, Master's Thesis, University of Tennessee, 2019.
25. G. Monteyne, S. Javed, G. Vandersteen, *Int. J. Heat Mass Transfer*, **69**, 129 (2014).
26. S. Gehlin, J. Spitler, *Proc. 9th Int. Conference of Thermal Energy Storage, Warsaw, Poland*, 381 (2003).
27. B. Sanner, G. Hellström, J. Spitler, S. Gehlin, in: *Proceedings World Geothermal Congress*, **1436**, 2005, Int. Geothermal Association, Antalya, Turkey, 2005.
28. F. Reda, N. Arcuri, P. Loiacono, D. Mazzeo, *Energy*, **91**, 294 (2015).
29. M. Mohanraj, Y. Belyayev, S. Jayaraj, A. Kaltayev, *Renewable Sustainable Energy Rev.*, **83**, 124 (2018).
30. M. Mohanraj, Y. Belyayev, S. Jayaraj, A. Kaltayev, *Renewable Sustainable Energy Rev.*, **83**, 90 (2018).
31. V. Trillat-Berdal, B. Souyri, G. Fraisse, *Energy and Buildings*, **38**, 12, 1477 (2006).
32. A. Georgiev, R. Popov, E. Toshkov, *Renewable Energy*, **147**, 2774 (2020).
33. M. Bottarelli, E. Baccega, S. Cesari, G. Emmi, *Renewable Energy*, **189**, 1324 (2022).
34. M. Alteneiji, M. Ali, K. Khan, R. Al-Rub, *Energy Storage and Saving*, **1** (3), 153 (2022).
35. M. Mohanraj, L. Karthick, R. Dhivagar, *Appl. Therm. Eng.*, **196**, 117263 (2021).
36. E. Bonamente, A. Aquino, F. Cotana, *Energy Procedia*, **101**, 1079 (2016).
37. E. Bonamente, A. Aquino, *Energies*, **13** (1), 117 (2019).
38. A. Al-Abidi, S. Mat, K. Sopian, M. Sulaiman, A. Mohammed, *Renewable and Sustainable Energy Reviews*, **20**, 353 (2013).
39. S. Self, B. Reddy, M. Rosen, *Applied Energy*, **101**, 341 (2013).
40. P. Eslami-Nejad, M. Ouzzane, Z. Aidoun, *Applied Energy*, **114**, 611 (2014).
41. D. Ndiaye, M. Bernier, *International J. of Refrigeration*, **35**, 8, 2110 (2012).
42. J. Wang, J. Zhao, N. Liu, *Appl. Mech. and Materials. Trans Tech Publications Ltd.*, **577**, 44 (2014).
43. H. Andresen, Y. Li, *Energy Procedia*, **70**, 155 (2015).
44. S. Jegadheeswaran, S. Pohekar, *Renewable and Sustainable Energy Reviews*, **13** (9), 2225 (2009).
45. J. Selker, D. Or, Oregon State University, 2021.
46. P. Cui, W. Yang, W. Zhang, K. Zhu, J. Spitler, M. Yu, *Energy Built Environ.*, Elsevier, 2022.
47. L. Boban, D. Miše, S. Herceg, V. Soldo, *Energies*, **14**, 8, 2134 (2021).
48. <https://www.mobilityengineeringtech.com/component/content/article/adt/pub/features/articles/33767> [accessed: 01.02.2019].
49. H. Javadi, J. Urchueguía, B. Badenes, M. Mateo, A. Ghafar, O. Chaudhari, G. Zirgulis, L. Lemus, *Renewable Energy*, **194**, 788 (2022).
50. H. Javadi, J. Urchueguía, S. Ajarostaghi, B. Badenes, *Energies*, **13**, 19, 5156 (2020).
51. M. Alizadeh, S. Sadrameli, *Renewable and Sustainable Energy Reviews*, **58**, 619 (2016).
52. R. Zeinelabdein, S. Omer, G. Gan, *Renewable and Sustainable Energy Reviews*, **82**, 2843 (2018).

53. K. Faraj, M. Khaled, J. Faraj, F. Hachem, C. Castelain, *Renewable and Sustainable Energy Reviews*, **119**, 109579 (2020).
54. M. Mochane, T. Mokhena, T. Motaung, L. Linganiso, *Journal of Thermal Analysis and Calorimetry*, **139**, 2951 (2020).
55. E. Bonamente, A. Aquino, *Energies*, **10**, 11, 1854 (2017).
56. Á. Pardiñas, M. Alonso, R. Diz, K. Kvalsvik, J. Fernández-Seara, *Energy and Buildings*, **140**, 28 (2017).
57. C. Pagkalos, G. Dogkas, M. Koukou, J. Konstantaras, K. Lymperis, M. Vrachopoulos, *Int. J. Thermofluids*, **1**, 100006 (2020).
58. P. Nico, Y. Zhang, X. Liu, C. Doughty, 1364, USDOE Geothermal Data Repository, United States, LBNL, Berkeley, CA, United States, 2022.
59. A. Alkhwildi, R. Elhashmi, A. Chiasson, *Geothermics*, **86**, 101864 (2020).
60. D. Qian, Z. O'Neill, Z., X. Liu, ORNL, Oak Ridge, TN, United States, 2020.
61. A. Aljabr, A. Chiasson, A. Alhajjaji, *Geothermics*, **96**, 102197 (2021).
62. G. Righetti, L. Doretto, C. Zilio, G. Longo, S. Mancin, *Int. J. Thermofluids*, **5**, 100035 (2020).
63. W. Yang, R. Xu, B. Yang, J. Yang, *Energy*, **174**, 216(2019).
64. Z. Zhou, Q. Liu, Y. Tao, Y. Peng, T. Zhou Y. Wang, *Appl. Therm. Eng.*, **222**, 119925 (2023).
65. M. Zhang, X. Liu, K. Biswas, J. Warner, *Appl. Therm. Eng.*, **162**, 114297 (2019).
66. J. Pássaro, A. Rebola, L. Coelho, J. Conde, *Int. J. Thermofluids*, **16**, 100245 (2022).
67. K. Yang, B. Liu, N. Du, J. Liu, Y. He, Y. Li, Y. Li, Q. Zhao, *J. Energy Storage*, **61**, 106822 (2023).
68. M. Mousa, A. Bayomy, M. Saghir, *Energies*, **13**, 18, 4699 (2020).
69. M. Mousa, A. Bayomy, M. Saghir, *Int. J. Thermofluids*, **10**, 100094 (2021).
70. M. Mousa, A. Bayomy, M. Saghir, *Applied Thermal Engineering*, **210**, 118381 (2022).
71. D. Qi, L. Pu, F. Sun, Y. Li, *Appl. Therm. Eng.*, **106**, 1023 (2016).
72. Z. Cao, G. Zhang, Y. Liu, X. Zhao, *Appl. Therm. Eng.*, **216**, 119144 (2022).
73. Y. Lyne, H. Paksoy, M. Farid, *Int. J. Energy Res.*, **43**, 9, 4148 (2019).
74. F. Chen, J. Mao, C. Li, P. Hou, Y. Li, Z. Xing, S. Chen, *Appl. Therm. Eng.*, **141**, 467 (2018).
75. H. Teamah, M. Lightstone, *Energy Build.*, **199**, 235 (2019).
76. C. Kutlu, Y. Su, Q. Lyu, S. Riffat, *Renewable Energy*, **206**, 848 (2023).
77. C. Zeng, Y. Yuan, F. Haghghat, K. Panchabikesan, X. Cao, L. Yang, Z. Leng, *J. Energy Storage*, **45**, 103726 (2022).
78. P. Dehdezi, M. Hall, A. Dawson, *Appl. Mech. Materials, Trans Tech Publications Ltd.*, **110**, 1191 (2012).
79. X. Bao, X. Qi, H. Cui, W. Tang, X. Chen, *Renewable Energy*, **185**, 790(2022).
80. G. Emmi, M. Bottarelli, *Renewable Energy*, **206**, 828 (2023).
81. J. Patel, J. Andharia, A. Georgiev, D. Dzhonova, S. Maiti, T. Petrova, K. Stefanova, I. Trayanov, S . Panyovska, *Bulg. Chem. Commun.*, **52**, Special issue C. 53 (2020).
82. J. Patel, J. Andharia, A. Georgiev, D. Dzhonova, S. Maiti, T. Petrova, K. Stefanova, I. Trayanov, S . Panyovska, *Springer, Cham*, 155 (2022).
83. Reference for station "Sofia - AIS IAOS/Pavlovo"
<https://www.eea.government.bg/kav/reports/air/qRreport/10/01#param-data>

Removal of methylene blue from aqueous solution by loquats nuclei

N. Samghouli, L. Rghioui*, S. Sebbahi, A. El Hajji, L. Guennoun, R. Khaoulaf, M. Serghini Idrissi, S. El Hajjaji

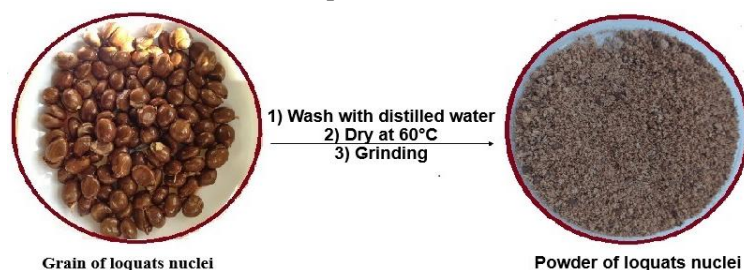
Laboratory of Spectroscopy, Molecular Modeling, Materials, Nanomaterials, Water and Environment, (LS3MN2E-CERNE2D), Department of Chemistry, Faculty of Sciences, Mohammed V University in Rabat, Av Ibn Battouta, BP1014, Rabat 10000, Morocco

Received: February 05, 2025; Revised: May 14, 2025

The aim of this paper is to study the performance of loquats nuclei in the removal of methylene blue (MB) from aqueous solutions. To achieve this, we conducted studies on adsorption kinetics, thermodynamics and isotherms. The adsorbent was characterized by X-ray diffraction (XRD), Fourier-transform infrared spectroscopy (FTIR) and surface charge measurements. Adsorption tests were carried out by varying different parameters such as MB concentration, adsorbent mass, particle size, contact time and solution pH. The experimental results showed that the adsorption capacity of loquats nuclei for MB can reach up to 90% ($q_m=8.728$ mg/g). Based on the correlation coefficients R^2 , the equilibrium data fitted well with pseudo-second order model ($R^2= 0.999$) and Freundlich isotherm ($R^2=0.993$). The adsorption equilibrium study showed that MB is adsorbed in multilayers on heterogeneous surfaces and the adsorption process is controlled by chemisorption. The thermodynamic study indicates that the adsorption of MB was spontaneous, exothermic and leads to an organized surface.

Keywords: Loquats nuclei, methylene blue, adsorption, pseudo-second-order, Freundlich, thermodynamic study.

Graphical abstract



INTRODUCTION

The release of dyes into the environment raises concerns for both toxicological and aesthetic reasons [1]. Industries such as textiles, leather, paper, plastics, etc., are some of the sources of dye effluents [2].

During the past three decades, several physical, chemical and biological bleaching methods have been reported. Adsorption is an economically feasible process for the removal and/or discoloration of dyes from textile effluents.

Researchers have demonstrated that a wide variety of natural materials have the ability to remove large amounts of organic pollutants and heavy metals present in water [3-14]. Currently, activated carbon is considered one of the most versatile adsorbents, and many studies showed its effectiveness; however, its use remains limited due to difficulties of its regeneration and its high cost.

An alternative solution is to utilize other efficient and more economical adsorbent materials.

This work falls within this framework. More specifically, we aim to contribute to the recovery of biomass. We have chosen to study the loquats nuclei (agro-food waste and lignocellulosic material). These nuclei can be used for the manufacture of activated carbon [15], bio-adsorbents for dyes [16, 17], substrates of bacterial fermentation [18, 19], for their anti-cancer properties due to their richness in amygdalin [20], and as pesticides [21].

Our focus is on investigating their potential for use in their natural state in the adsorption of methylene blue in aqueous solution. This work is relevant and innovative because it falls within the framework of the valorization of low-cost biomass that could be integrated into the water decontamination sector. In addition, the adsorption process used here is environmentally friendly and

* To whom all correspondence should be sent:
E-mail: rghiouilofti@gmail.com

does not require much energy compared to other processes (coagulation, oxidation, precipitation, filtration, electrochemical processes, etc.)

EXPERIMENTAL

Adsorbent: Loquats nuclei

Loquats nuclei are lignocellulosic materials with fibrous structures, mainly composed of organic and mineral substances (ash) [22]. They are usually accompanied by a certain amount of water [23, 24]. The organic substances consist primarily of four types of polymers, namely cellulose, hemicelluloses, lignin and pectin. The first two polymers are also referred to as carbohydrates or holocelluloses.

The loquats nuclei used in this work are sourced from Berkane region along the Zeggel Valley in Morocco. They were washed several times with distilled water until the smell disappeared and the rinse water was clear, and then dried in the oven at 60°C for 24 h. After grinding, they were sieved to retain only the fraction between 0.250 and 0.315 mm.

Adsorbate: Methylene blue

The adsorbate that we want to remove is methylene blue (MB), an organic compound with the chemical formula $C_{16}H_{18}N_3S^+Cl^-$ (Figure 1). Its molar mass is 319.85g/mol. Methylene blue belongs to the xanthenes family and is classified as a cationic dye ($C_{16}H_{18}N_3S^+$), which is preferentially adsorbed by the acid sites of the adsorbents. This dye was chosen as a representative model for medium-sized organic pollutants. Methylene blue was used without any purification, and solutions were prepared by dissolving the amounts of the dye in distilled water.

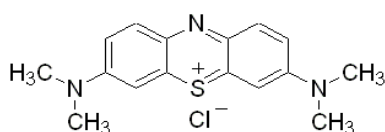


Fig. 1. Chemical structure of MB

X-ray diffraction. The powder diagram of loquats nuclei was recorded using a Siemens D5000 diffractometer with Cu $K\alpha_1$ radiation ($\lambda = 1,5406 \text{ \AA}$) operating at 45 kV and 40 mA within the 2θ range of 5-60°. Data were collected at a rate of 0.067°/min at 298K. The XRD patterns were identified by comparison with JCPDS standards.

Infrared spectroscopy. Infrared spectrum of loquats nuclei was collected on a Bruker-Tensor 27 spectrophotometer equipped with an ATR module fitted with a diamond crystal as the attenuated total reflection element. The spectrophotometer scanned

the spectral range 4000 - 500 cm^{-1} with a resolution of up to 4 cm^{-1} .

Point of zero charge pH_{pzc} . In order to determine the point of zero charge (pH_{PZC}), we used the same protocol described in the literature [25]. It consisted of placing 50 ml of NaCl (0.01 M) in a closed flask and adjusting the pH to values between 2 and 12 by adding NaOH or HCl solutions (0.1 M). We then added to each vial 0.15 g of adsorbent at room temperature for 48 h, and then the final pH was determined. On a graph of $pH_f = f(pH_i)$, the intersection of the curve with the first bisector gives the isoelectric point.

Adsorption experiments

To follow the kinetics and adsorption isotherms of MB on loquats nuclei, the adsorbent was placed in 50 mL of a solution of methylene blue at different concentrations. The mixture, at a well-determined pH, was stirred at room temperature. The solid was separated by centrifugation and the filtrate was analyzed by measuring the absorbance using a Mapada 1600 UV-visible spectrophotometer at the wavelength corresponding to the maximum absorption (664 nm for MB).

The sorption yield was evaluated by determining the adsorption capacity of the adsorbent noted q_a or the retention rate of the adsorbate according to the following equations:

$$q_a = \frac{(C_0 - C_e)}{m} V \quad (1)$$

$$R\% = \frac{(C_0 - C_e)}{C_0} 100 \quad (2)$$

where C_0 and C_e (mg.L^{-1}) are the initial and equilibrium concentration of MB solution respectively, V refers to the volume of the solution (L) and m is the adsorbent mass (g).

Kinetic modeling

In order to analyze the adsorption kinetics of MB onto loquats nuclei, different kinetic models have been tested: pseudo-first-order, pseudo-second-order, intra-particle diffusion and Elovich model. These models are represented by equations 3, 4, 5 and 6, respectively [26]:

$$\log(q_e - q_t) = \log(q_e) - \left(\frac{K_1 t}{2,303} \right) \quad (3)$$

$$\frac{t}{q_t} = \frac{1}{K_2 q_e^2} + \frac{1}{q_e} t \quad (4)$$

$$q_t = K_i t^{1/2} + C \quad (5)$$

$$q_t = \frac{1}{\beta} \text{Ln}(\alpha\beta) + \frac{1}{\beta} \text{Lnt} \quad (6)$$

where q_e and q_t (mg.g^{-1}) are the amounts adsorbed at equilibrium and at time t , respectively. K_1 (min^{-1}),

K_2 ($\text{g}\cdot\text{mg}^{-1}\cdot\text{min}^{-1}$) and K_1 ($\text{mg}/\text{g}\ \text{min}^{1/2}$) are the rate constants of the pseudo-first order, the pseudo-second order and the intraparticle diffusion, respectively. C is the intercept. α is the initial adsorption rate constant ($\text{mg}\cdot\text{g}^{-1}\cdot\text{min}^{-1}$) and β is Elovich's parameter ($\text{g}\cdot\text{mg}^{-1}$) associated with the degree of coverage of adsorbent surface and energy of chemisorption.

Isotherm modeling

For the adsorption equilibrium study, the following models were chosen: Langmuir, Freundlich, Temkin, and Dubinin-Radushkevich. The linear form of the Langmuir isotherm model is depicted by [9]:

$$\frac{1}{Q_e} = \frac{1}{bQ_m} \frac{1}{C_e} + \frac{1}{Q_m} \quad (7)$$

where Q_e is the quantity of MB adsorbed per unit mass of adsorbent at equilibrium ($\text{mg}\cdot\text{g}^{-1}$), Q_m is the maximum adsorbed quantity ($\text{mg}\cdot\text{g}^{-1}$), C_e is the MB concentration at equilibrium (mg/L), b is the thermodynamic constant of the characteristic adsorption equilibrium of the adsorbent, depending on the temperature and the experimental conditions ($\text{L}\cdot\text{mg}^{-1}$).

In the Langmuir model, to determine whether the adsorption is favorable or not, it is imperative to estimate a dimensionless constant called the separation factor or equilibrium parameter, denoted R_L . The equation of R_L is:

$$R_L = \frac{1}{1 + b \times C_0} \quad (8)$$

where C_0 represents the MB initial concentration (mg/L).

If $R_L > 1$, adsorption is unfavorable; if $R_L = 1$, it is linear adsorption; if $0 < R_L < 1$, adsorption is favorable and if $R_L = 0$, adsorption is irreversible.

The Freundlich model is based on an empirical equation that describes the variation of energies with the adsorbed quantity. This distribution of interaction energies is explained by heterogeneity of adsorption sites. This model admits the existence of interactions between the adsorbed molecules. According to the linear form, the Freundlich model can be expressed as [9]:

$$\ln(Q_e) = \frac{1}{n} \ln(C_e) + \ln(K) \quad (9)$$

where K is related to the adsorption capacity ($\text{mg}\cdot\text{g}^{-1}$) and $1/n$ represents the empirical parameter of the adsorption intensity.

Temkin equation is based on the effect of some direct adsorbent-adsorbate interactive relation on sorption isotherm. Due to these interactions, the heat

of adsorption decreases linearly with the increase in the rate of coverage of the adsorbent's surface.

The linear Temkin equation is [9]:

$$Q_e = \frac{RT}{b_T} \ln K_T + \frac{RT}{b_T} \ln C_e \quad (10)$$

where b_T is Temkin isotherm constant (J/mol) and R is the ideal gas constant ($R=8,314\text{J}/\text{mol}\cdot\text{K}$)

The Dubinin-Radushkevich isotherm, unlike the Langmuir isotherm, does not assume a homogeneous surface or constant adsorption potential. This isotherm model is represented by the following equation [27]:

$$\ln q_e = \ln q_m - \beta \varepsilon^2 \quad (11)$$

where ε is the Polanyi potential: $\varepsilon = RT \ln(1 + 1/C_e)$. β gives the mean free energy E (Kj/mol) of sorption per molecule of the sorbate when it is transferred to the surface of the solid from infinity in the solution and can be computed using the relationship [28]:

$$E = \frac{1}{(2\beta)^{0.5}} \quad (12)$$

This parameter gives information about chemical or physical adsorption.

Thermodynamic study

The thermodynamic parameters of the adsorption of MB on loquats nuclei are determined from the study of the adsorption reaction at different temperatures (293, 308, 318, 328 and 333K) using the following equation:

$$\Delta G^0 = \Delta H^0 - T\Delta S^0 \quad (13)$$

ΔG^0 is the standard Gibbs free energy (KJ/mol) and T is the temperature (K).

The standard enthalpy ΔH^0 (KJ/mol) and entropy changes ΔS^0 ($\text{KJ}/\text{K}\cdot\text{mol}$) of adsorption can be determined from the following Van't Hoff equation:

$$\ln(K_d) = \frac{\Delta S^0}{R} - \frac{\Delta H^0}{RT} \quad (14)$$

with $K_d = q_e/C_e$.

K_d is the distribution coefficient, q_e is the quantity adsorbed at equilibrium (mg/g), C_e is the concentration of the adsorbate in the solution at equilibrium (mg/L) and R is the ideal gas constant [29].

RESULTS AND DISCUSSION

The surface morphology of loquats nuclei was also examined by El Marouani *et al.* [30]. The authors concluded that the material is organized in a few agglomerates of blisters of various sizes and geometries on the surface.

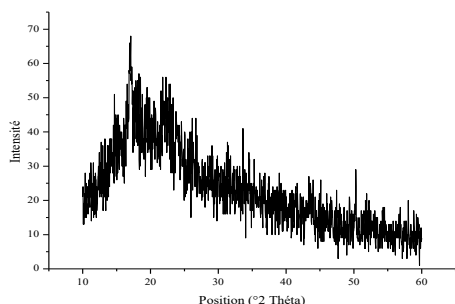


Fig. 2a. X-ray diffraction patterns of loquats nuclei

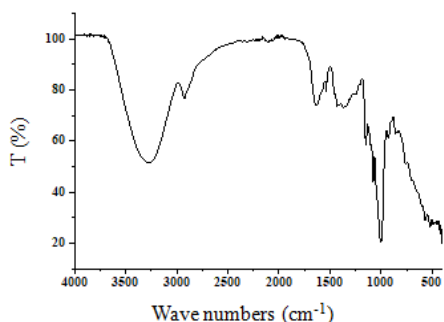


Fig. 2b. Infrared spectrum of loquats nuclei

Point of zero charge (pH_{PZC}). The point of zero charge (pH_{PZC}) is one of the parameters that characterize the adsorbents. It is the pH value at which the surface charge of the adsorbent is equal to zero. If the pH of the medium is lower than pH_{PZC}, the surface of the adsorbent is positively charged. If the pH is higher than pH_{PZC}, the surface is negatively charged. The pH_{PZC} value is obtained from the intersection of the first bisector with the curve giving the final pH as a function of the initial pH. As it can be seen in Figure 3, the pH_{PZC} of loquats nuclei is equal to 6.83.

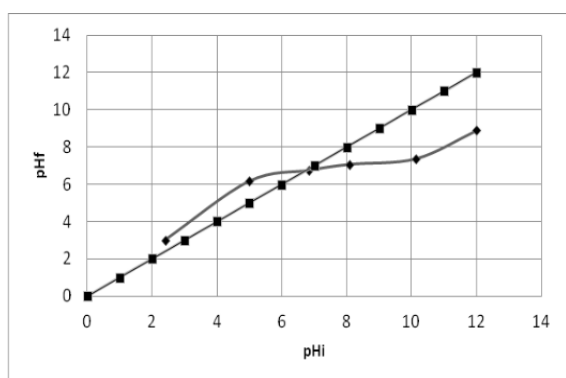


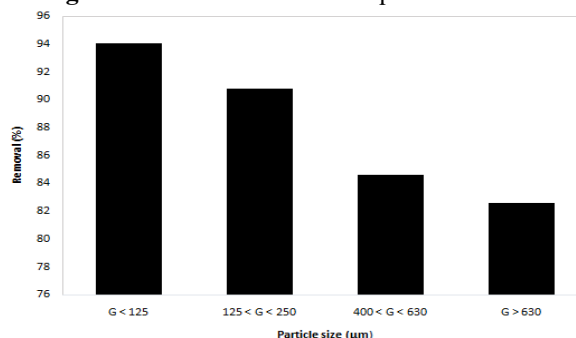
Fig. 3. Point of zero charge (pH_{PZC}) of loquats nuclei

Adsorption of methylene blue by loquats nuclei

Effect of parameters. The adsorption process is controlled by several factors. In this study, the particle size, adsorbent dose, contact time, pH, and initial concentration of methylene blue were taken into account.

a) *Particle size effect.* Particle size is an important factor that affects the adsorption capacity. The retention rate was evaluated for various particle sizes of loquats nuclei (Figure 4). As shown in the figure, the percentage of MB retention decreases as particle size increases. This result can be explained by the fact that smaller particles provide a greater surface area for methylene blue adsorption. Similar results have been reported by other authors [29, 31]. The grain size selected for the remainder of our study was less than 125 μm .

Fig. 4. Particle size effect of loquats nuclei



b) *Adsorbent dose.* The study of the effect of adsorbent mass was carried out by changing the initial mass of the adsorbent from 20 to 120 mg. The volume of the solution was 50 mL (Figure 5).

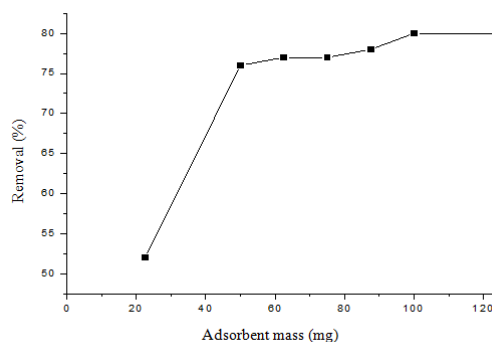


Fig. 5. Effect of the adsorbent mass

From this figure it can be observed that the percentage of MB adsorption increased from 52 to 86% with an increase of the adsorbent dose from 22.5 to 100 mg. This can be explained by the availability of surface sites with the increase of the adsorbent dose [10, 11]. Beyond this value, the retention capacity did not exhibit any variation. Therefore, 100 mg of the adsorbent was selected as the optimal dose.

c) *Effect of contact time.* The effect of contact time on the percentage removal of MB by loquats nuclei was investigated at an initial dye concentration of 5 mg/L and adsorbent dose of 100 mg. The results are presented in Figure 6.

This figure shows that the percentage removal of MB increased from 0% to 87% at 40 min. After this

time, the percentage removal doesn't exhibit significant changes. The adsorption rate is fast at the beginning of the process and becomes increasingly slow until the stirring time equilibrium is reached. The rapid adsorption kinetics during the first minutes of reaction can be attributed to the fact that, at the start of adsorption, the number of active sites available at the surface of the adsorbent material is much greater than that of the sites remaining after 20 min. According to the figure, 40 min is sufficient to achieve high MB removal.

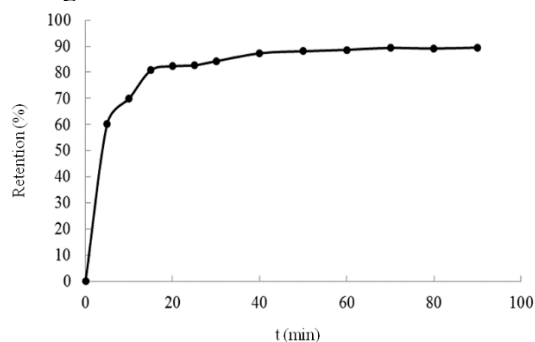


Fig. 6. Effect of contact time

d) Effect of solution pH on dye adsorption. The effect of pH on the MB adsorption onto loquats nuclei was studied by changing pH values from 3 to 12. These values were adjusted by addition of HCl or NaOH. The results are plotted in Figure 7.

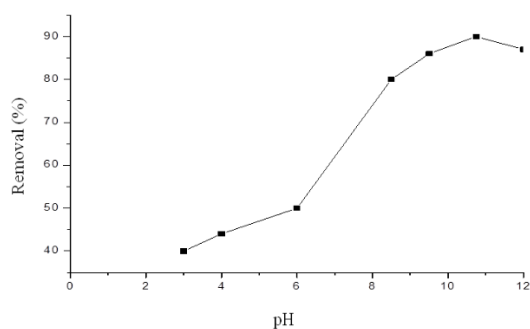


Fig. 7. Effect of pH on MB adsorption by loquats nuclei

From this figure, it can be seen that the adsorption capacity of MB increases when the pH increases, reaching high values in basic medium. This could be explained by the fact that at $\text{pH} < \text{pH}_{\text{PZC}}$, the surface

of the adsorbent is positively charged, which weakens the interaction between methylene blue ions (cationic pollutant) and the adsorbent sites. When $\text{pH} > \text{pH}_{\text{PZC}}$, the surface of the adsorbent is negatively charged, generating a strong interaction between the dye ions and the surface sites. Similar results were obtained in previous works [11, 32]. Subsequently, the experiments were carried out at the initial pH of 10.75.

e) Effect of methylene blue concentration. The effect of the initial adsorbate concentration on the MB adsorption rate was studied by varying the adsorbate concentration from 5 to 20 mg/L. The pH was maintained at 10.75. The results obtained are shown in Figure 8.

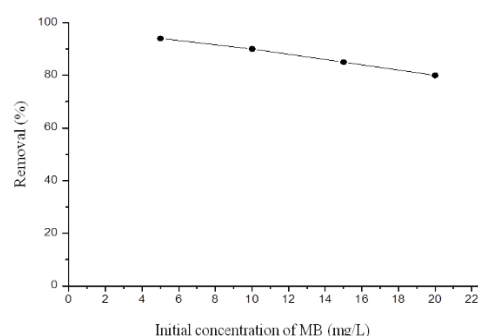


Fig. 8. Effect of the initial concentration of MB

As can be seen, a slight decrease in the retention rate is observed with increasing concentration. This can be explained by the fact that at lower concentrations, all the MB present in the adsorption medium can interact with the bonding sites on the adsorbent surface. The decrease in the retention rate with the increase in concentration is due to the initial saturation of the adsorption sites. The same results were reported previously [10, 11, 33].

Kinetic study. Figures 9-12 show the results obtained for the different kinetic models tested in this study. The values of the correlation coefficients, as well as the corresponding kinetic parameters deduced from the slope and the y-intercept of the various curves, are given in Table 1.

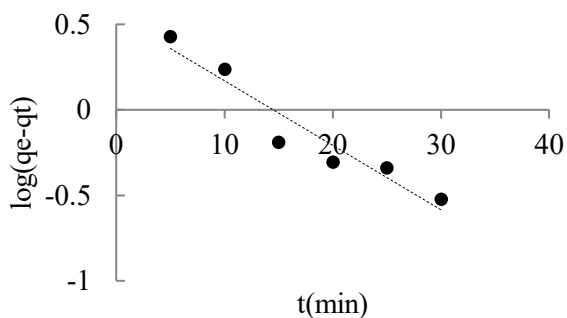


Fig. 9. Pseudo-first order kinetic plots for the adsorption of MB by loquats nuclei

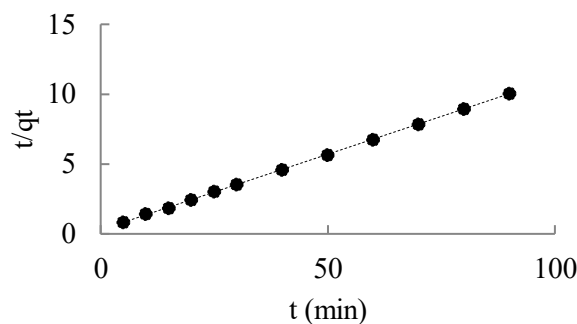


Fig. 10. Pseudo-second order kinetic plots for the adsorption of MB by loquats nuclei

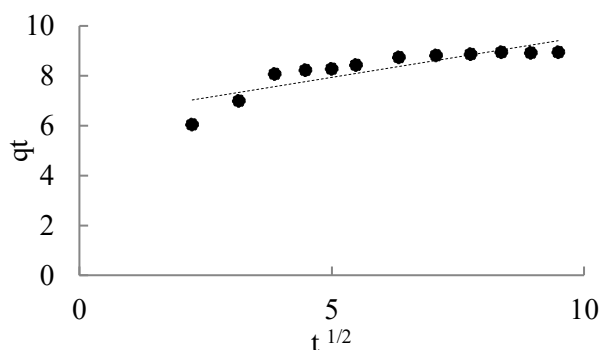


Fig. 11. Intra-particle diffusion model plots for the adsorption of MB by loquats nuclei

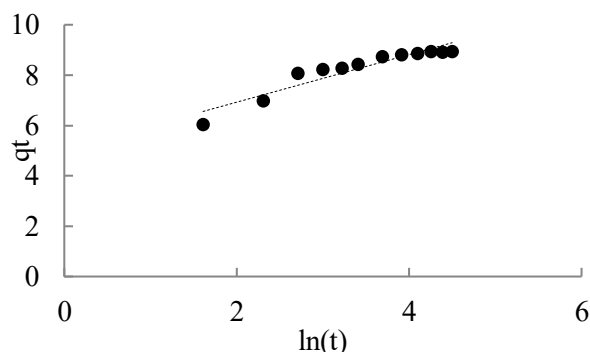


Fig. 12. Elovich equation model plots for the adsorption of MB by loquats nuclei

Table 1. Kinetic parameters for MB adsorption by loquats nuclei

Kinetic models	Parameters	
Pseudo-first-order model	R^2	0.919
	k_1 (min^{-1})	0.085
	$q_{e \text{ calc}}$ (mg/g)	3.524
Pseudo-second order model	R^2	0.999
	k_2 ($\text{g} \cdot \text{mg}^{-1} \cdot \text{min}^{-1}$)	0.041
	$q_{e \text{ calc}}$ (mg/g)	9.259
	$q_{e \text{ exp}}$ (mg/g)	8.728
	$\Delta q = q_{e \text{ calc}} - q_{e \text{ exp}}$ (mg/g)	0.531
Intra-particle diffusion model	R^2	0.740
	K_i ($\text{mg} \cdot \text{g}^{-1} \cdot \text{min}^{-0.5}$)	0.327
	C	6.297
Elovich equation	α (mg/g min)	195.547
	β (g/mg)	1.059
	R^2	0.886

According to Table 1 and Figures 9-12, we concluded that the mechanism of the MB adsorption onto loquats nuclei can be described by the pseudo-

second-order model. Indeed, we noted that the R^2 correlation coefficient is higher than those of the other models and is very close to 1. Moreover, the quantities adsorbed at equilibrium, calculated from this model, agree very well with those obtained experimentally.

Adsorption equilibrium study. The linear representations of the experimental values of MB adsorption on loquats nuclei are shown in Figures 13-16 and the corresponding parameters are given in Table 2.

As shown in Table 2, the Freundlich equation represents the adsorption process very well, the value of the correlation coefficient is close to 1 ($R^2=0.993$), indicating a very good mathematical fit. The Freundlich model is the most adequate to describe the adsorption of MB on loquats nuclei, suggesting that the adsorption of MB occurs in multilayers on heterogeneous surfaces. In addition, the values of K and n indicate good adsorption capacity.

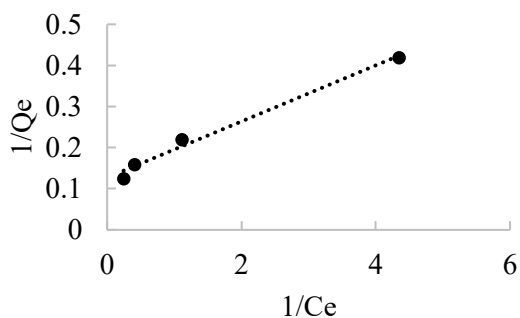


Fig. 13. Linear representation of Langmuir isotherm.

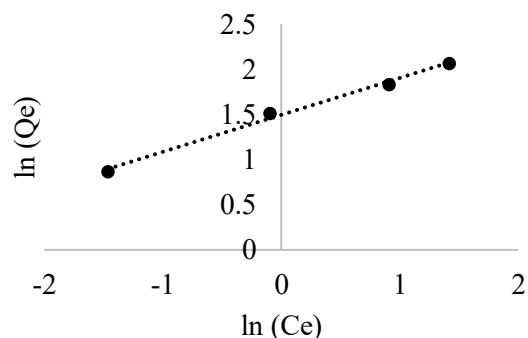


Fig. 14. Linear representation of Freundlich isotherm.

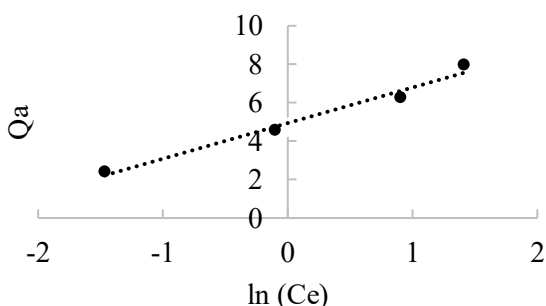


Fig. 15. Linear representation of Temkin isotherm.

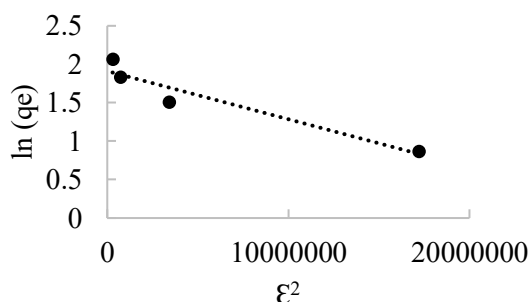


Fig. 16. Linear representation of Dubinin-Radushkevich isotherm.

Table 2. Linear isotherms parameters

Isotherm	Parameters	
Langmuir	$q_{m,cal}$ ($mg \cdot g^{-1}$)	7.874
	B	1.868
	R_L	0.026
	R^2	0.987
	n	0.409
Freundlich	K	4.464
	R^2	0.993
Temkin	b_T (J/mol)	1.854
	K_T (L/g)	8.360
	R^2	0.980
Dubinin-Radushkevich	E (KJ/mol)	$11.785 \cdot 10^6$
	q_s (mg/g)	6.753
	β (mol^2/K_j^2)	6.10^{-8}
	R^2	0.917

On the other hand, the b_T value estimated by the Temkin model (Table 2) is very low, indicating weak interactions between the adsorbent and the adsorbate. Finally, the high mean free energy value calculated from the Dubinin-Radushkevich model (Table 2) indicates that the mechanism is controlled by chemisorption [5].

Thermodynamic study. The values of ΔH° and ΔS° were obtained, respectively, from the slope and intercept of the curve of $\ln(K_d)$ as a function of $1/T$ (Figure 17).

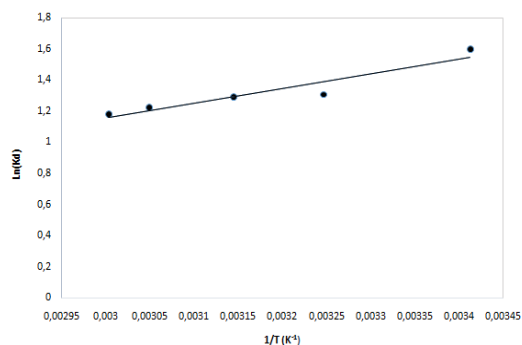


Fig. 17. Representation of $\ln(K_d)$ as a function of $1/T$

Table 3. Thermodynamic parameters of the adsorption of MB on loquats nuclei

T(K)	q_e (mg/g)	ΔG° (KJ/mol)	ΔH° (KJ/mol)	ΔS° (J/K.mol)
293	9.0804	-3.889		
308	8.8082	-3.347		
318	8.7902	-3.411	-7.831	-13.857
328	8.7171	-3.335		
333	8.6704	-3.272		

Table 3 gives the thermodynamic parameters of the adsorption of MB on loquats nuclei. The negative values of ΔG° indicate that the adsorption of MB by

the loquats nuclei is spontaneous. Moreover, the negative value of ΔH° confirms that the adsorption process is exothermic. The negative value of ΔS° indicates that the order of distribution of the dye molecules on the adsorbent is important compared to that in the solution. This also suggests a probability of thermodynamically favorable adsorption [34].

Comparison with other adsorbents. The adsorption quantity (q_e) of MB by loquats nuclei has been compared with other adsorbents reported in the literature, which are listed in Table 4. From this Table, it can be considered that the loquats nuclei tested here is effective in the removal of MB from aqueous solutions and, moreover, it may be used as an alternative to expensive commercial adsorbents.

Table 4. Comparison of adsorbed quantity (Q_e) of MB onto loquats nuclei with those for other reported adsorbents

Adsorbent	Adsorbed quantity q_e exp. (mg/g)	Ref.
Pure cellulose	0.11	35
Modified cellulose	0.35	35
Thuya lignin	3.55	8
Algerian data stones	4.9	36
Loquats nuclei	8.728	This study

Adsorption mechanisms. The adsorption mechanism mainly depends on the surface of the loquats nuclei and the structure of methylene blue. Two mechanisms can be proposed in this work: Firstly, the percentage elimination of MB increases considerably in basic medium. In this environment, the adsorbent surface is negatively charged ($pH > pH_{PZC}$), and methylene blue is a cationic dye, suggesting an electrostatic interaction mechanism between the adsorbent and the adsorbate. Secondly, the surface of the loquats nuclei contains alcoholic OH functional groups [30]. Hydrogen bonds can form between the nitrogen of the MB and the hydrogen of the OH groups.

CONCLUSIONS

The present study investigated the efficiency of loquats nuclei in the removal of MB from aqueous solutions. Infrared and XRD analysis were performed to characterize the adsorbent. The point of zero charge (PZC) was also determined.

The adsorption tests were carried out by varying the adsorbent mass, particle size, initial concentration of the adsorbate, contact time and pH of the adsorbate solution. The optimal conditions are: $m=100$ mg of loquats nuclei, particle size less

than $125 \mu m$, 5 mg/L of dye, 40 min of contact time, and pH of dye solution= 10.75 .

The kinetic study of MB adsorption on this adsorbent is relatively fast, with an equilibrium time of 40 min . The retention of methylene blue is described by pseudo-second order kinetics. Freundlich model best represents the experimental values, indicating that MB is adsorbed in multilayers on heterogeneous surfaces. The thermodynamic study indicates that the adsorption process is favorable, exothermic and spontaneous.

Two mechanisms of MB adsorption by the loquats nuclei were proposed: (i) electrostatic interaction mechanism and (ii) hydrogen bond formation mechanism between the nitrogen atoms of the dye and the OH groups of the adsorbent.

From this study, we can conclude that loquats nuclei are effective biosorbents for the removal of MB from aqueous solution.

REFERENCES

1. H. Metivier-Pignon, C. Faur-Brasquet, P. L. Cloirec, *Sep. Purif. Technol.*, **31(1)**, 3 (2003). [https://doi.org/10.1016/S1383-5866\(02\)00147-8](https://doi.org/10.1016/S1383-5866(02)00147-8)
2. K. Ravikumar, B. Deebika, K. Balu, *J. Hazard. Mater.*, **122**, 75 (2005). <https://doi.org/10.1016/j.jhazmat.2005.03.008>
3. M. El Marouani, J. El Jastimi, N. El Hrech, A. El Hajji, L. Rghioui, S. Sebbahi, S. El Hajjaji, F. Kifani-Sahban, *J. Mater. Environ. Sci.*, **8(12)**, 4313 (2017). <https://doi.org/10.26872/jmes.2017.8.12.454>
4. I. Enniya, L. Rghioui, A. Jourani, *Sustainable Chemistry and Pharmacy*, **7**, 9 (2018). <https://doi.org/10.1016/j.scp.2017.11.003>
5. M. El Marouani, K. Azoulay, I. Bencheikh, L. El Fakir, L. Rghioui, A. El Hajji, S. Sebbahi, S., El Hajjaji, F. Kifani-Sahban, *J. Mater. Environ. Sci.*, **9(8)**, 2387 (2018).
6. Y. El Boundati, K. Ziat, A. Naji, M. Saidi and L. Rghioui, *Int. J. Adv. Res.*, **6(11)**, 300 (2018). <https://doi.org/10.21474/IJAR01/7999>
7. S.S. Nayak, N.A. Mirgane, V.S. Shivankar, K.B. Pathade, G.C. Wadhawa, *Mater. Today Proc.*, **37(2)**, 2302 (2021). <https://doi.org/10.1016/j.matpr.2020.07.728>
8. M. Saber, L. EL Hamdaoui, M. EL Moussaouiti and M. Tabyaoui, *Cellulose Chemistry and Technology*, **56(1-2)**, 69 (2022). <https://doi.org/10.35812/CelluloseChemTechnol.2022.56.06>
9. M. El Khomri, N. El Messaoudi, A. Dbik, S. Bentahar, Y. Fernine, A. Bouich, A. Lacherai, A. Jada, *Emergent Materials*, **5(6)**, 1679 (2022). <https://doi.org/10.1007/s42247-022-00390-y>
10. S. A. Gupta, Y. Vishesh, N. Sarvshrestha, A. S. Bhardwaj, P. A. Kumar, N. S. Topare, S. Raut-Jadhav, S. A. Bokil, A. Khan, *Materials Today: Proceedings*, **57**, 1500 (2022). <https://doi.org/10.1016/j.matpr.2021.12.044>

11. M. Sh. Gohr, A. I. Abd-Elhamid, A. A. El-Shanshory, H. M. A. Soliman, *Journal of Molecular Liquids*, **364**, 118227 (2022). <https://doi.org/10.1016/j.molliq.2021.118227>
12. H. Li, V. L. Budarin, J. H. Clark, M. North, X. Wu, *Journal of Hazardous Materials*, **436**, 129174 (2022). <https://doi.org/10.1016/j.jhazmat.2022.129174>
13. S. Zuhara, S. Pradhan, Y. Zakaria, A. R. Shetty and G. McKay, *Molecules*, **28(3)**, 1511 (2023). <https://doi.org/10.3390/molecules28031511>
14. El. Ratiki, F. Abida, A. Ouass, I. Khadouddi, Z. Hatim, E. H. Rifi, A. Kheribech, *Mor. J. Chem.*, **11(2)**, 318 (2023). <https://doi.org/10.48317/IMIST.P>
15. H. Sütücü, H. Demiral, *J. Anal. Appl. Pyrolysis*, **84(1)**, 47 (2009). <https://doi.org/10.1016/j.jaap.2008.10.008>
16. O. Aksakal, H. Ucun, Y. Kaya, *Water Sci. Technol.*, **59(8)**, 1631 (2009). <https://doi.org/10.2166/wst.2009.130>
17. O. Hamdaoui, *Desalination*, **271**, 279 (2011). <https://doi.org/10.1016/j.desal.2010.12.043>
18. M. Taskin, S. Erdal, O. Canli, *Food Sci. Biotechnol.*, **19**, 1069 (2010). <https://doi.org/10.1007/s10068-010-0150-7>
19. Z. Guanjie, Y. Zhiqiang, S. Xian-Ai, G. Yanghao, *New Biotechnology*, **25**, S94 (2009). <https://doi.org/10.1016/j.nbt.2009.06.373>
20. Y. Kawahito, M. Kondo, S. Sachmudah, K. Sibano, M. Sasaki, M. Goto, *Separation and Purification Technology*, **61(2)**, 130 (2008). <https://doi.org/10.1016/j.seppur.2007.09.022>
21. I. Baekelmans, R. H. Brown, I. M. Harvey, Patent Publication N° WO2005077188 A1 2005.
22. M. Jebrane, Thesis, University of Bordeaux 1, France, 2009.
23. P. Martin, Bois et production, Cedapus Editions, 1992.
24. C. Ake, Thesis, University of Technology of Compiègne, France, 1984.
25. K. Azoulay, I. Bencheikh, A. Moufti, A. Dahchour, J. Mabrouki, S. El Hajjaji, *Chemical Data Collections*, **27**, 100385 (2020). <https://doi.org/10.1016/j.cdc.2020.100385>
26. K. C. Nebagha, K. Ziat, L. Rghioui, M. Khayet, A. Naji, M. Saidi, *J. Mater. Environ. Sci.*, **6(10)**, 2694 (2015).
27. V. Puccia, M. J. Avena, *Colloid and Interface Science Communications*, **41**, 100376 (2021). <https://doi.org/10.1016/j.colcom.2021.100376>
28. S. M. Hassany, M. H. Chaudhary, *Appl. Radiat. Isot.*, **47(4)**, 467 (1996). [https://doi.org/10.1016/0969-8043\(95\)00310-X](https://doi.org/10.1016/0969-8043(95)00310-X)
29. K. C. Nebagha, K. Ziat, L. Rghioui, M. Khayet, M. Saidi, K. Aboumaria, A. El Hourch, S. Sebti, *J. Mater. Environ. Sci.*, **6(11)**, 3022 (2015).
30. M. El Marouani, S. Bentahar, L. El Hamdaoui, L. Trif, R. Zerrouki, G. Costa, F. Kifani-Sahban, *Biointerface Research in Applied Chemistry*, **11(2)**, 9027 (2021). <https://doi.org/10.33263/BRIAC112.90279043>
31. J. Ali, E. M. Bakhsh, N. Houssain, M. Bilal, K. Akhtar, T. M. Fagieh, E. Y. Danish, A. M. Asiri, X. Su, S. B. Khan, *Industrial Crops and Products*, **179**, 114676 (2022). <https://doi.org/10.1016/j.indcrop.2022.114676>
32. L. Kasmi, M. Soussi El-Begrani, A. Ben Ali, M. M. M. Hajaji, S. Tazi and S. Haloui, *Biosci. Biotechn. Res. Asia*, **18(1)**, 71 (2021). <http://dx.doi.org/10.13005/bbra/2897>
33. S. T. Nipa, N. R. Shefa, S. Parvin, M. A. Khatun, M. J. Alam, S. Chowdhury, M. A. R. Khan, S. M. A. Z. Shawon, B. K. Biswas, M. W. Rahman, *Results in Engineering*, **17**, 100857 (2023). <https://doi.org/10.1016/j.rineng.2022.100857>
34. B. Mahjoub, M. C. Ncibi, M. Seffen, *Can. J. Chem. Eng.*, **86(1)**, 23 (2008). <https://doi.org/10.1002/cjce.20005>
35. R. Bouhdadi, S. Benhadi, S. Molina, B. George, M. El Moussaouiti et al., *Maderas*, **13**, 105 (2011), <https://doi.org/10.4067/S0718-221X2011000100009>
36. O. Khelifi, I. Mehrez, W. Ben Salah, F. Ben Salah, M. Younsi, M. Nacef, A. M. Affoune, *Larhyss J.*, **13(4)**, 135 (2016).

Comparative analysis of the effect of cricket powder and spirulina in model meat systems as substitutes for soy in raw pork products

M. M. Momchilova^{1*}, D. N. Gradinarska-Ivanova², K. I. Valkova-Yorgova², D. G. Yordanov²

¹Department of Food Technologies, Agricultural Academy, Institute of Food Preservation and Quality, 154 Vasil Aprilov Blvd., 4000 Plovdiv, Bulgaria

²Department of Meat and Fish Technology, Technological Faculty, University of Food Technologies, 26 Maritsa Blvd., 4000 Plovdiv, Bulgaria

Received: February 19, 2025; Accepted: May 10, 2025

This study focused on comparing and assessing the effects of substituting soy protein in raw semi-finished pork products with alternative protein sources, such as cricket powder and spirulina powder. Changes in the physicochemical, technological, and microbiological properties of the model meat systems were examined. The inclusion of spirulina powder resulted in reduced hardness along with increased springiness and cohesiveness, while the addition of cricket powder led to lower adhesiveness and improved chewiness and gumminess. The experimental samples exhibited good emulsion stability, albeit with slightly lower values compared to those containing soy protein. Incorporating the studied protein sources, either individually or in combination, as replacements for soy protein, enhanced the nutritional profile of the model meat systems by increasing fiber content and improving oxidative stability.

Keywords: Meat products, protein, color, textural traits, emulsion stability

INTRODUCTION

The global population's steady increase has brought about a heightened demand for protein-dense foods, compelling the food industry and researchers to explore sustainable approaches to meet this need [1-4]. Meat products are a well-known source of high-quality protein with a favorable balance of amino acids [5]. However, the continuation of current trends in meat consumption is projected to double the demand for animal proteins, intensifying the strain on environmental resources and ecosystems. In addition to this challenge, crises such as the COVID-19 pandemic, geopolitical conflicts, climate change, and pollution have further driven efforts to identify alternative food sources as part of the solution to global food insecurity. Plant-derived proteins have gained popularity as replacements for meat proteins in various food applications. Their health benefits, absence of cholesterol, and cost-effectiveness make them attractive for use in meat products [6-8]. Among these, soy protein is the most extensively utilized in the food sector due to its superior protein content and functional properties, including excellent water retention and emulsification, which enhance the technological quality of meat products [9-11]. Algae have also emerged as an intriguing alternative protein source, attracting attention for their nutritional benefits [12]. They contain all

essential amino acids required by humans and, in some cases, surpass traditional sources such as meat, dairy, soy, and grains in protein quality [13]. Beyond their protein content, algae are rich in bioactive compounds that offer potential health-promoting effects [14, 15]. Spirulina, a blue-green alga, is particularly noteworthy due to its high protein concentration-ranging from 60% to 70%/-and its ease of cultivation and processing [16-18].

Edible insects represent another emerging protein source, known for their abundance in essential nutrients such as protein, fiber, fatty acids, vitamins, and minerals [19-21]. Insects are increasingly seen as a sustainable option to alleviate the environmental pressures caused by traditional livestock farming [22]. For instance, the house cricket (*Acheta domestica*), widely consumed in Southeast Asia, provides a protein content of 20–25 g per 100 g of fresh weight, comparable to that of conventional meat. Crickets are often processed into protein-rich flour, containing 50% - 60% protein, which can be incorporated into various food formulations [23, 24].

This study investigates the potential of substituting soy protein in raw semi-finished pork products with alternative protein sources, namely cricket flour and spirulina powder. The research examines the effects of these replacements on the physicochemical, technological, and microbiological characteristics of model meat systems.

* To whom all correspondence should be sent:
E-mail: masha821982@abv.bg

MATERIALS AND METHODS

The following recipe was used in the experiment: lean pork meat (shoulder blade): 500 g/kg; semi-fat pork: 500 g/kg; water: 200 g/kg; soy protein: 10 g/kg, and sodium chloride: 18 g/kg. Seven experimental samples were prepared for the study with different concentrations of soy, spirulina and cricket powder protein according to Table 1. Before their addition, they had been hydrated in water in a 1:3 w/v ratio. The protein additives (soy and spirulina) were purchased from retail shops, the cricket powder was supplied by EntoSynergy Ltd. (Balgarevo, Bulgaria), and the meat raw materials by the Lovech Meat Processing Company within Boni Holding, Bulgaria.

Table 1. Modeled substitution composition in the raw meat systems

Sample name	Ingredient ratios, g/kg ⁻¹		
	Soy protein, (X1)	Spirulina powder, (X2)	Cricket powder, (X3)
S	10.0	0.0	0.0
Sp	0.0	10.0	0.0
CP	0.0	0.0	10.0
SSp	5.0	5.0	0.0
SCP	5.0	0.0	5.0
SpCP	0.0	5.0	5.0
SSpCP	3.33	3.33	3.33

Note: Samples: S- (control sample with soy protein); Sp- (sample with spirulina powder); CP- (sample with cricket powder); SSp- (sample with soy protein and spirulina powder); SCP- (sample with soy protein and cricket powder); SpCP- (sample with spirulina powder and cricket powder); SSpCP- (sample with soy protein, spirulina powder and cricket powder).

The samples were prepared as follows: the meat was ground on a meat grinder with a grid diameter of 6 mm, and then divided into seven equal parts. After that, the necessary salting materials, water, and a protein supplement, respectively, were added to each part in a mixer; 60 g meatballs were formed from the meat batter obtained and then packed on PVC plates and stored at 0±4 °C. At the 24th hour, the raw meatballs were analyzed according to the following parameters: overall chemical composition, pH, water activity (a_w), oxidative and emulsifying capacity, and textural and microbiological characteristics.

Proximate composition

The water content was determined by drying the samples at 104±1 °C to constant weight using a KERN MLS-A moisture balance (Kern & Sohn GmbH, Germany). The protein content was

determined by the Kjeldahl method [25]; the fat content by the Soxhlet method [26]; and the mineral, carbohydrate and dietary fiber contents were analyzed according to [27-29]. The sodium chloride content was determined by Mohr's method [30]. The energy value was calculated using arithmetic mean values of the overall chemical composition according to European Parliament and Council Regulation (EU) No 1169/2011 of 25 October 2011 on the provision of food information to consumers.

pH, a_w and color

The pH determination was carried out on an aqueous extract of the sample (1:9 w/v), using a pH meter (Milwaukee MW102 PRO+ 2-in-1 pH and temperature meter with ATC). The water activity (a_w) was measured using HygroPalm – HP23 at 22-25 °C. The color parameters were determined spectrophotometrically using a Minolta chroma meter (model CR 410, Osaka, Japan) in the CIELab system.

Emulsion stability

For determination of the emulsion stability, the method described by Zorba and Kurt [31] was used. Thirty grams of each sample were weighed into a centrifuge tube and heated on a water bath at 70 °C for 30 min. Immediately after heating, the tubes were centrifuged at 2000 min⁻¹ for 10 min, and the separated water and oil were weighed and used to calculate the emulsion stability (ES).

Texture profile analysis (TPA)

A TA-XT Plus texture analyzer (Stable Micro Systems, Surrey, GB) was used for the analysis of the texture profile of the samples, under the following measurement conditions: sample size: 40±2 mm in diameter and 25±2 mm in height; diameter of the compression cylinder: 50 mm, compression speed: 2 mm/s; degree of deformation: 8 mm; and relaxation time between two compressions: 5 s. The hardness, springiness, cohesiveness, gumminess, chewiness, and adhesiveness of the samples were calculated on the basis of the values obtained [32-34].

Oxidative stability (TBARS and antioxidant capacity)

The content of the thiobarbituric acid reactive substances was measured according to the method described by Cabral *et al.* [35].

The antioxidant capacity was determined and evaluated on the basis of the free radical scavenging activity (DPPH). The DPPH determination was based on the method described by Brand-Williams

et al. [36] and Petrova et al. [37] with the following modification: methanol solution of DPPH (6×10^{-5} M) in a 1:9 (v/v) ratio was added to 250 μ L of water extract of the sample in a 1:3 ratio. After 20 min in the dark at room temperature, the 515 nm absorption of the prepared reaction mixture was measured (Evolution 201 UV Visible spectrophotometer, Thermo Scientific). A water-soluble vitamin E analogue was used as a standard, and the results obtained were presented as Trolox equivalents (TE) in μ mol per 100 g sample.

Microbiological analysis

The total microbial load of the samples on the 1st and 5th day was studied through the following microbiological parameters: total bacteria count according to [38] and presence of molds and yeasts according to [38]. The samples were prepared in accordance with [40].

Statistical analysis

All the data obtained were statistically analyzed by one-way analysis of variance (ANOVA) using the Statgraphics 16 software product. Significant ($P < 0.05$) differences between the treatments were determined using Duncan’s post hoc test. All experiments were performed in triplicate, and the data presented in the tables and figures were expressed as means \pm standard deviation (SD).

RESULTS AND DISCUSSION

Proximate composition

No significant differences ($P > 0.05$) were found in the water content values between the experimental samples, except for sample SpCP, for which a higher value was reported compared to sample S (control

sample) ($P < 0.05$) (Table 2). Also, no significant differences were found in the protein, fat and carbohydrate contents between the control and experimental samples, which was probably due to the low concentration in which they were added. The results obtained were in agreement with data presented by other authors who used spirulina to replace soy protein in raw sausages and beef burgers [41, 42]. The higher dietary fiber content found in the experimental samples compared to the control sample ($P < 0.05$) was related to the chitin contained in the cricket powder [43] and possibly, the polysaccharide composition of the algae. The mineral content of the studied samples also increased with the addition of spirulina and cricket powder and was the highest in the SpCP sample. Similar results were obtained by authors who investigated the possibility of including algae and insect powder in meat products with a view to improving their nutritional quality and reducing the sodium chloride content [44-47].

pH and water activity (a_w)

The data obtained showed statistically significant differences between the samples, both on the first day and on the fifth day of their cold storage (Table 3). On the first day, the control sample S had the lowest pH value (6.19), most probably owing to the higher pH values of the cricket and spirulina powders. The pH value of the cricket powder sample CP (6.21) was closest to the control sample S, and the highest pH was reported for sample Sp (6.37). A tendency to lower pH was observed in all samples on the 5th day of their cold storage, maintaining the established differences in the values between the individual samples.

Table 2. Proximate composition and energy value of the raw model meat systems

Samples	Parameter							
	Moisture content, %	Proteins, %	Fats, %	Carbohydrates, %	Dietary fiber, %	NaCl, %	Ash, %	Energy value, KJ/kcal
S	65.89 \pm 3.06 ^a	12.74 \pm 0.84 ^a	14.93 \pm 0.1 ^a	0.55 \pm 0.02 ^a	8.6 \pm 1.3 ^a	1.82 \pm 0.03 ^a	2.14 \pm 0.2 ^a	857/205
Sp	68.48 \pm 1.6 ^{ab}	13.42 \pm 0.59 ^a	14.42 \pm 0.56 ^a	0.45 \pm 0.03 ^a	10.3 \pm 0.42 ^{bc}	2.03 \pm 0.02 ^f	2.48 \pm 0.9 ^{ab}	867/207
CP	68.04 \pm 0.66 ^{ab}	13.1 \pm 0.1 ^a	14.72 \pm 0.05 ^a	0.53 \pm 0.06 ^a	9.42 \pm 0.47 ^{ab}	1.96 \pm 0.09 ^{bc}	3.06 \pm 0.8 ^{ab}	860/206
SSp	67.04 \pm 0.3 ^{ab}	12.98 \pm 0.79 ^a	14.68 \pm 0.31 ^a	0.49 \pm 0.04 ^a	10.38 \pm 0.4 ^{bc}	1.85 \pm 0.04 ^{ab}	2.32 \pm 0.6 ^a	864/207
SCP	66.69 \pm 0.55 ^{ab}	12.29 \pm 1.29 ^a	14.63 \pm 0.3 ^a	0.45 \pm 0.07 ^a	8.82 \pm 1.07 ^a	1.87 \pm 0.09 ^{ab}	2.26 \pm 0.7 ^a	837/200
SpCP	69.03 \pm 1.54 ^b	13.47 \pm 0.23 ^a	14.52 \pm 0.46 ^a	0.49 \pm 0.09 ^a	10.39 \pm 0.5 ^{bc}	1.92 \pm 0.8 ^{abc}	3.54 \pm 0.4 ^b	867/207
SSpCP	66.59 \pm 1.65 ^{ab}	13.31 \pm 0.25 ^a	14.8 \pm 1.12 ^a	0.58 \pm 0.07 ^a	11.04 \pm 1.15 ^c	1.92 \pm 0.08 ^{abc}	2.85 \pm 0.5 ^{ab}	881/211

Note: *The results are presented as mean values for the respective sample after triple measurements of the respective parameter. **a-f: Values bearing the same superscripts are not statistically different ($P > 0.05$). ***Samples: S- (control sample with soy protein); Sp- (sample with spirulina powder); CP- (sample with cricket powder); SSp- (sample with soy protein and spirulina powder); SCP- (sample with soy protein and cricket powder); SpCP- (sample with spirulina powder and cricket powder); SSpCP- (sample with soy protein, spirulina powder and cricket powder).

Table 3. Changes in pH and a_w in the model meat systems

Period (days)	pH						
	S	Sp	CP	SSp	SCP	Sp.CP	SSpCP
1	6.19±0.08 ^a	6.37±0.09 ^b	6.21±0.05 ^a	6.28±0.07 ^{ab}	6.23±0.05 ^{ab}	6.3±0.09 ^{ab}	6.24±0.05 ^a
5	6.03±0.03 ^a	6.3±0.09 ^c	6.18±0.06 ^{bc}	6.24±0.08 ^c	6.2±0.09 ^{bc}	6.22±0.03 ^c	6.08±0.08 ^{ab}
a _w							
1	0.869±0.001 ^b	0.872±0.005 ^b	0.852±0.001 ^a	0.87±0.002 ^b	0.868±0.015 ^b	0.872±0.003 ^b	0.871±0.003 ^b

Note: The results are presented as mean values for the respective sample after triple measurements of the respective parameter. ^{a-c}: Values bearing the same superscripts are not statistically different (P>0.05). Samples: S- (control sample with soy protein); Sp- (sample with spirulina powder); CP- (sample with cricket powder); SSp- (sample with soy protein and spirulina powder); SCP- (sample with soy protein and cricket powder); SpCP- (sample with spirulina powder and cricket powder); SSpCP- (sample with soy protein, spirulina powder and cricket powder).

Table 4. Color characteristics of the model meat systems

Parameter	Sample						
	S	Sp.	CP	SSp.	SCP	SpCP	SSpCP
L*	55.08±8.33 ^c	36.19±6.36 ^a	52.13±12.52 ^{bc}	46.96±3.98 ^{abc}	59.35±5.98 ^c	40.96±2.54 ^{ab}	50.71±8.66 ^{bc}
a*	8.69±1.65 ^{bc}	-6.38±1.53 ^a	7.71±1.04 ^b	-4.99±2.75 ^a	11.6±3.46 ^c	-3.59±2.62 ^a	-4.3±0.76 ^a
b*	8.86±1.53 ^{bcd}	4.74±0.94 ^a	10.03±1.92 ^{cd}	8.19±2.88 ^{abc}	12.12±2.75 ^d	7.48±0.83 ^{abc}	6.3±2.82 ^{ab}
C	12.42±2.14 ^{bc}	6.95±2.65 ^a	12.72±2.03 ^{cd}	9.5±1.98 ^{abc}	16.8±4.32 ^d	8.45±0.54 ^{ab}	7.69±0.14 ^a
h	45.64±3.39 ^a	134.17±9.39 ^c	52.52±2.66 ^a	133.57±11.01 ^c	46.65±2.88 ^a	113.88±12.99 ^b	126.53±9.62 ^{bc}

Note: *The results are presented as mean values for the respective sample after five measurements of the respective parameter. ** ^{a-d}: Values bearing the same superscripts are not statistically different (P>0.05). ***Samples: S- (control sample with soy protein); Sp- (sample with spirulina powder); CP- (sample with cricket powder); SSp- (sample with soy protein and spirulina powder); SCP- (sample with soy protein and cricket powder); SpCP- (sample with spirulina powder and cricket powder); SSpCP- (sample with soy protein, spirulina powder and cricket powder).

From a technological point of view, it is important to point out that the use of additives that can increase the pH of the meat batter is desirable with a view to reducing losses during subsequent heat treatment and improving the consistency of the finished product.

As regards the water activity (a_w) values, no statistical differences were found between the samples (P>0.05), except for the sample prepared with complete replacement of the soy protein with cricket powder (P< 0.05), where a slightly lower value (0.852) was reported.

Color parameters

The L* color lightness values of the model meat systems ranged from 36.19 in sample Sp to 59.35 in sample SCP (Table 4). The experimental samples were statistically different (P<0.05) from the control sample as a result of both the type of additives used and their amount. The comparison of control sample S with cricket powder sample CP showed a decrease in the L* value, which was consistent with the data reported in [47]. The lower L* values of the spirulina samples were due to its dark green color, and a statistical difference was also observed between

individual samples depending on the amount added. Lower color component values (L*, a* and b*) were also obtained by other authors [41], who investigated the possibility of soy protein substitution with various plant proteins and algae, including chlorella and spirulina. The negative values measured for a* in the spirulina samples were attributed to the pigments phycocyanin (blue color) and chlorophyll (green color) present in the composition of *Spirulina platensis* [42, 49, 50].

The cricket powder sample (CP) also showed a decrease in the red component a* compared to the control sample, which some researchers attributed to the greenish hues that cricket powder imparts to the meat batter [48, 51]. The comparison of the control sample with the cricket powder sample indicated that the use of cricket powder resulted in an increase in the yellow color component also reported by Kolev et al. [52].

The lowest h value was measured in the control sample S followed by the sample prepared with 50% soy protein and 50% cricket powder, i.e. SCP, with no statistical difference between them (P>0.05) (Table 4). In the samples made with spirulina powder, however, the opposite effect was observed:

the greater the amount of spirulina added to replace the soy protein, the higher was the value found for the color hue (h).

Oxidative stability (TBARS and DPPH)

Oxidative stability is one of the most important parameters determining the quality of meat products [53-55] and TBARS content, expressed as mg MDA/kg sample, is considered a parameter that can be used to measure the secondary products of lipid oxidation [56]. The TBARS data obtained (Table 5) on the first day of sample storage demonstrated oxidative changes ranging from 0.14 mg MDA.kg⁻¹ in sample CP to 0.74 mg MDA.kg⁻¹ in control sample S.

The comparison of the cricket powder samples with the control sample showed significantly (P<0.05) lower MDA results in the experimental samples, both on the first and on the fifth day of storage. The results obtained coincided with the data reported by other authors, according to which oxidative stability is a result of the antioxidant

potential of edible insect powder [57-59]. Lower MDA values were also measured in the spirulina samples compared to the control sample (P<0.05). Similarly to these results, the authors of [60] also found lower lipid oxidation levels in raw sausages made with the addition of spirulina extracts.

The results of the antioxidant capacity (DPPH) analysis indicated that the values obtained for DPPH in the experimental samples were significantly (P<0.05) higher than those in the control sample (Table 5). The higher antioxidant activity in sample Sp could be attributed to the polyphenols, flavonoids, tannins and polysaccharides contained in spirulina [61, 62]. Similarly to the results obtained in this study, the authors of [63] observed an increase in the antioxidant potential and storage stability of pork meatballs made with insect powder addition. According to other authors [64, 65], the antioxidant capacity of edible insects is mainly due to the phenolic compounds they contain.

Table 5. Oxidative stability and antioxidant capacity (TBARS and DPPH) of the model meat systems

Period (days)	TBARS, mg MDA/kg ⁻¹						
	S	Sp	CP	SSp	SCP	Sp.CP	SSpCP
1	0.74±0.09 ^c	0.34±0.06 ^b	0.14±0.04 ^a	0.4±0.03 ^b	0.19±0.04 ^a	0.35±0.08 ^b	0.38±0.09 ^b
5	0.83±0.06 ^d	0.48±0.04 ^{b^c}	0.34±0.07 ^a	0.52±0.09 ^c	0.4±0.05 ^{ab}	0.4±0.06 ^{ab}	0.59±0.08 ^c
	DPPH, μmol TE 100 g						
1	30±3.2 ^a	74±3.1 ^b	136±2.2 ^f	125±2.8 ^c	106±2.1 ^d	98±1.9 ^c	176±3.6 ^g

Note: *The results are presented as mean values for the respective sample after triple measurements of the respective parameter. ** a-g: Values bearing the same superscripts are not statistically different (P>0.05). ***Samples: S- (control sample with soy protein); Sp- (sample with spirulina powder); CP- (sample with cricket powder); SSp- (sample with soy protein and spirulina powder); SCP- (sample with soy protein and cricket powder); SpCP- (sample with spirulina powder and cricket powder); SSpCP- (sample with soy protein, spirulina powder and cricket powder).

Table 6. Texture parameters and emulsion stability of the model meat systems

Samples	Parameter						
	Hardness (N)	Springiness	Cohesiveness	Gumminess	Chewiness (N)	Adhesiveness (Nmm)	ES, %
S	18.02±0.73 ^d	0.71±0 ^{ab}	0.48±0.03 ^{ab}	2.2±0.16 ^b	1.56±0.11 ^b	-1.56±0.1 ^{bc}	98.32±0.3 ^d
Sp	10.4±0.02 ^a	0.86±0.04 ^c	0.56±0.02 ^c	1.48±0.03 ^a	1.27±0.08 ^{ab}	-1.98±0.25 ^{ab}	98.02±0.5 ^{cd}
CP	15.77±2.53 ^{cd}	0.7±0.05 ^{ab}	0.47±0.02 ^a	1.94±0.3 ^{ab}	1.35±0.25 ^{ab}	-1.17±0.09 ^c	97.58±0.27 ^{bcd}
SSp	13.43±1.79 ^{abc}	0.72±0.02 ^{ab}	0.5±0.01 ^{ab}	1.73±0.41 ^a	1.14±0.13 ^a	-2.46±0.65 ^a	97.15±0.7 ^b
SCP	13.01±0.73 ^{abc}	0.68±0.06 ^a	0.49±0.01 ^{ab}	1.7±0.1 ^a	1.16±0.08 ^a	-1.5±0.2 ^{bc}	97.05±0.32 ^b
SpCP	14.44±2.5 ^{bc}	0.72±0.03 ^{ab}	0.48±0.05 ^{ab}	1.81±0.41 ^{ab}	1.3±0.34 ^{ab}	-1.76±0.54 ^{abc}	97.47±0.5 ^{bc}
SSpCP	11.16±2.83 ^{ab}	0.76±0.05 ^b	0.52±0.03 ^{bc}	1.59±0.18 ^a	1.21±0.2 ^a	-1.59±0.62 ^{bc}	96.13±0.14 ^a

Note: *The results are presented as mean values for the respective sample after three measurements of the respective parameter. ** a-d: Values bearing the same superscripts are not statistically different (P>0.05). ***Samples: S- (control sample with soy protein); Sp- (sample with spirulina powder); CP- (sample with cricket powder); SSp- (sample with soy protein and spirulina powder); SCP- (sample with soy protein and cricket powder); SpCP- (sample with spirulina powder and cricket powder); SSpCP- (sample with soy protein, spirulina powder and cricket powder).

Emulsion stability and textural characteristics

The choice and quantity of protein sources used resulted in variations in emulsion capacity and alterations in the texture of the experimental samples (Table 6). All samples demonstrated high emulsion stability, two of them - control sample S and spirulina sample Sp - achieving values exceeding 98%. The excellent emulsion stability observed in algae-based samples can be attributed to their high protein content which provides emulsifying properties comparable to or better than those of whey proteins, soy proteins, and sodium caseinate [66-68]. In contrast, the cricket powder sample CP displayed a slightly lower emulsion stability than sample S, with a value of 97.58% (P<0.05). The lowest stability value was recorded for sample SSpCP at 96.13% (P<0.05). According to Pires *et al.* [69], when emulsion stability falls to 85–88% or below, issues related to consistency and structure can arise in the final sausage products.

The texture analysis revealed that control sample S exhibited the highest hardness value at 18.02 N. Incorporating various plant-based proteins and fibers, such as soy, wheat, and other cereals, tends to increase the hardness of meat matrices [70]. Similarly, the inclusion of cricket powder contributed to a rise in hardness, aligning with findings by Kim *et al.* [46], who studied the effects of cricket powder in sausages. Conversely, unlike soy and cricket powder, the addition of spirulina to raw semi-finished meat products resulted in reduced hardness (Table 6). Sample Sp, where spirulina entirely replaced soy protein, displayed the lowest

hardness value (P<0.05) while achieving the highest springiness and cohesiveness values.

The highest gumminess and chewiness values, which are secondary parameters related to hardness, were reported for the control sample S (with soy protein) [71, 72]. The texture profile data obtained showed that control sample S (with soy protein) required the greatest chewing force when consumed, followed by the sample with complete replacement of soy protein with cricket powder (CP).

The highest adhesiveness was measured in the sample with equal soy protein and spirulina amounts (SSp), whereas lower values were found in the soy protein and cricket powder samples (SCP) (Table 6).

Microbiological characteristics

The microbiological characteristics of the samples of raw semi-finished products were monitored on the 1st and 5th day of their cold storage (Table 7).

Regarding the total bacteria count (TBC) on the 1st day of storage, no statistically significant difference (P>0.05) was observed between the individual samples. During their storage up to the 5th day, the bacteria count grew in all samples, with the lowest value recorded in sample Sp (P<0.05). Spirulina has been reported to have the ability to inhibit the growth of certain microorganisms, both pathogenic and food spoilage ones [73].

On the 1st day of storage, no presence of molds and yeasts was detected in experimental samples CP and SCP, while the highest number was reported in the control sample S (Table 7).

Table 7. Microbiological characteristics of the model meat systems on the 1st and 5th day of cold storage

Storage period (days)	S	Sp.	CP	SSp.	SCP	SpCP	SSpCP
TBC, log cfu/g							
1	3.12±0.14 ^{aA}	2.96±0.42 ^{aA}	3.11±0.42 ^{aA}	3.85±0.12 ^{bA}	3.2±0.17 ^{aA}	3.86±0.15 ^{bA}	4.20±0.42 ^{bA}
5	5.08±0.7 ^{bB}	4.18±0.14 ^{aB}	4.67±0.21 ^{abB}	6.11±0.58 ^{cB}	5.23±0.28 ^{bB}	6.11±0.78 ^{cB}	6.04±0.54 ^{cB}
Molds and yeasts, log cfu/g							
1	2.61±0.12 ^{bA}	2.08±0.68 ^{bA}	0.00±0.00 ^{aA}	2.12±0.84 ^{aA}	0.00±0.00 ^{aA}	2.08±0.98 ^{bA}	2.29±0.67 ^{bA}
5	3.38±0.88 ^{bA}	3.12±0.78 ^{abB}	3.08±0.41 ^{abB}	3.30±0.64 ^{bB}	2.00±0.65 ^{aB}	3.26±0.25 ^{bB}	3.63±0.82 ^{bB}

Note: *The results are presented as mean values for the respective sample after three measurements of the respective parameter. ** ^{a-c}: Values in rows bearing the same superscripts are not statistically different (P>0.05). *** ^{A-B}: Values in columns bearing the same superscripts were not statistically different (P>0.05). **** Samples: S- (control sample with soy protein); Sp- (sample with spirulina powder); CP- (sample with cricket powder); SSp- (sample with soy protein and spirulina powder); SCP- (sample with soy protein and cricket powder); SpCP- (sample with spirulina powder and cricket powder); SSpCP- (sample with soy protein, spirulina powder and cricket powder).

On the 5th day of storage, an increase in the number of molds and yeasts in the samples was observed, and, again, the lowest values were reported for samples CP and SCP. The difference in the number of molds and yeasts in the samples probably resulted from the microbiological status of the additives used, but this did not lead to any significant microbiological deficiencies.

CONCLUSION

The comparative analysis led to the conclusion that the use of spirulina and cricket powder, in combination or alone, as soy protein substitutes in model meat systems, resulted in products with a balanced nutritional composition and a higher fiber content. The experimental samples studied had good emulsion stability, although with slightly lower values compared to the control sample produced using soy protein, and significantly improved oxidative stability. The addition of spirulina caused a decrease in the hardness parameter and an increase in springiness and cohesiveness, whereas the addition of cricket powder led to a decrease in adhesiveness and improved chewiness and gumminess. The effect of the alternative protein sources used in the meat systems included pronounced changes in the color characteristics of the raw semi-finished products studied, but their perception and evaluation by consumers remain to be investigated in a complex sensory study of ready-to-eat semi-finished products in the context of the changing food ecosystem and innovations.

Acknowledgements: The research was carried out under project TN 15 of the Agricultural Academy, task 1, entitled "Investigation of the possibilities of using different protein sources in semi-finished meat products. Effect on the quality characteristics and technological properties". The researchers also thank the Boni Holding company, Bulgaria, for the meat raw materials supplied.

REFERENCES

1. C. Anzani, F. Boukid, L. Drummond, A. M. Mullen, C. Alvarez, *Food Res. Int.*, **137**, 109575 (2020).
2. M. Toldra, P. Taberner, D. Parés, C. Carretero, *Meat Sci.*, **182**, 108640 (2021).
3. O. Yuliarti, T. J. K. Kovis, N. J. Yi, *J. Food Eng.*, **288**, 110138 (2021).
4. M. Momchilova, D. Gradinarska-Ivanova, D. Yordanov, G. Zsivanovits, N. Pats, *Meat Technol.*, **65**, 25 (2024).
5. P. Williams, *Nutr. Diet.*, **64**, 113-119 (2007).
6. F. A. L. Carvalho, M. Pateiro, R. Dominguez, S. Barba-Orellana, J. Mattar, S. Rimac Brnčić, F.J. Barba, J. M. Lorenzo, *JFPP.*, **43**, e13935 (2019).
7. F. J. Marti-Quijal, S. Zamuz, I. Tomašević, G. Rocchetti, L. Lucini, K. Marszałek, F.J. Barba, J. M. Lorenzo, *J. Sci. Food Agric.*, **99**, 3672 (2019).
8. S. Zamuz, L. Purriños, F. Galvez, N. Zdolec, V. Muchenje, F. J. Barba, J. M. Lorenzo, *JFPP.*, **43**, e13940 (2019).
9. L. D. He, X. N. Guo, K. X. Zhu, *Food Hydrocoll.*, **87**, 187 (2019).
10. K. M. Kang, S. H., Lee, H. Y. Kim, *Food Sci. Anim. Resour.*, **42**, 73 (2022).
11. P. Qin, T. Wang, Y. Luo, *J. Agric. Food Res.*, **7**, 100265 (2022).
12. F. J. Barba, *Food Res. Int.*, **99**, 969 (2017).
13. J. Lorenzo, R. Agregán, P. Munekata, D. Franco, J. Carballo, S. Şahin, F. Barba, *Mar. Drugs*, **15**, 360 (2017).
14. O. Parniakov, E. Apicella, M. Koubaa, F. J. Barba, N. Grimi, N. Lebovka, G. Pataro, G. Ferrari, E. Vorobiev, *Bioresour. Technol.*, **198**, 262 (2015).
15. J. Matos, C. Cardoso, N. M. Bandarra, C. Afonso, *Food Funct.*, **8**, 2672 (2017).
16. P. Spolaore, C. Joannis-Cassan, E. Duran, A. Isambert, *JBB.*, **101**, 87 (2006).
17. I. Priyadarshani, B. Rath, *J. Algal Biomass Util.*, **3**, 89 (2012).
18. A. K. Koyande, K. W. Chew, K. Rambabu, Y. Tao, D. T. Chu, P. L. Show, *Food Sci. Hum. Wellness.*, **8**, 16 (2019).
19. M. Bawa, S. Songsermpong, C. Kaewtapee, W. Chanput, *J. Insect Sci.*, **20**, 10 (2020).
20. X. Han, B. Li, E. Puolanne, M. Heinonen, *Foods*, **12**, 1262 (2023).
21. F. Zhang, X. Li, X. Liang, B. Kong, F. Sun, C. Cao, H. Gong, H. Zhang, Q. Lui, *Food Res. Int.*, **176**, 113846 (2024).
22. K. Lange, Y. Nakamura, *JFB.*, **14**, 4 (2021).
23. M. Igual, P. García-Segovia, J. Martínez-Monzó, *J. Food Eng.*, **282**, 110032 (2020).
24. N. Kolev, D. Vlahova-Vangelova, D. Balev, D. Gradinarska, S. Dragoev, *JMAB.*, **25**, 15 (2022).
25. BDS EN ISO (2006) Animal feeding stuffs - Determination of nitrogen content and calculation of crude protein content - Part 1: Kjeldahl method (BDS EN ISO 5983-1:2006). Geneva: International Organization for Standardization.
26. BDS (1992) Meat and meat products. Determination of fats (BDS 8549:1992). Sofia: Bulgarian Institute for Standardization.
27. BDS (1980) Meat and meat products. Determination of ash content (BDS 9373:1980). Sofia: Bulgarian Institute for Standardization.
28. BDS (1984) Meat products. Method for determination of starch content (BDS 5713:1984). Sofia: Bulgarian Institute for Standardization.
29. AOAC (1986) Total Dietary Fiber in Foods - Enzymatic-Gravimetric Method (AOAC 985.29). Rockville, MD: AOAC International.
30. BDS (1993) Meat and meat products. Determination of sodium chloride (BDS 7168:1993). Sofia: Bulgarian Institute for Standardization.
31. Ö. Zorba, Ş. Kurt, *Meat Sci.*, **73**, 611 (2006).

32. M. C. Bourne, *Food Technol.*, **32**, 62 (1978).
33. M. Bourne, *Food Texture and Viscosity: Concept and Measurement*, 2nd edn., London, Academic Press, Elsevier, 2002.
34. E. J. Kim, V. K. Corrigan, D. I. Hedderley, L. Motoi, A. J., Wilson, M. P. Morgenstern, *J. Texture Stud.*, **40**, 457 (2009).
35. N.O. Cabral, R.F. Oliveira, F. C., Henry, D. B. de Oliveira, A. C. do Santos Junior, J. A. M. Junior, M. L. L. Martines *Food Sci. Technol.*, **42**, 1 (2021).
36. W. Brand-Williams, M. E. Cuvelier, C. L.W.T. Berset, *LWT-Food sci technol.*, **28**, 25-30 (1995).
37. K. Petrova, P. Ivanova, K. I. Mihalev, D. Georgiev, *JMAB*, **19**, 221 (2016).
38. BDS EN ISO (2013) Microbiology of the food chain. Horizontal method for enumeration of microorganisms. Part 1: Colony count at 30°C by pour plate technique (BDS EN ISO 4833-1:2013). Geneva, International Organization for Standardization.
39. BDS EN ISO (2011) Microbiology of food and animal feeding stuffs — Horizontal method for the enumeration of yeasts and moulds — Part 1: Colony count technique in products with water activity greater than 0.95 (BDS EN ISO 21527-1:2011). Geneva: International Organization for Standardization.
40. BDS EN ISO (2004) Microbiology of food and animal feeding stuffs. Preparation of test samples, initial suspension and decimal dilutions for microbiological examination. Part 2: Specific rules for the preparation of meat and meat products (BDS EN ISO 6887-2:2004). Geneva: International Organization for Standardization.
41. T. Žugčić, R. Abdelkebir, F. J. Barba, A. Rezek-Jambrak, F. Gálvez, S. Zamuz, D. Granato, J. M. Lorenzo, *JFST.*, **55**, 4544 (2018).
42. F. J. Marti-Quijal, S. Zamuz, I. Tomašević, B. Gómez, G. Rocchetti, L. Lucini, F. Remize, F. J. Barba, J. M. Lorenzo, *LWT-Food sci technol.*, **110**, 316 (2019).
43. D. Wang, Y. Bai, J. Li, C. Zhang, *Insect Sci.*, **11**, 275 (2004).
44. Y. S. Choi, J. S. Kum, K. H. Jeon, J. D. Park, H.W. Choi, K. E. Hwang, T. J. Jeong, Y. B. Kim, C. J. Kim, *Food Sci. Anim. Resour.*, **35**, 748 (2015).
45. Y. S. Park, Y. S. Choi, K. E. Hwang, T. K., Kim, C. W. Lee, D. M. Shin, S. G. Han, *Korean J Food Sci Anim Resour.*, **37**, 351 (2017).
46. H. W. Kim, D. Setyabrata, Y. J. Lee, O. G. Jones, Y. H. B. Kim, *IFSET*, **38**, 116 (2016).
47. B. M. Cabrol, M. Glišić, M. Baltić, D. Jovanović, Ć. Siladi, S. Simunović, I. Tomašević, A. Raymundo, *Meat Sci.*, **198**, 109123 (2023).
48. I. Ho, A. Peterson, J. Madden, E. Huang, S. Amin, A. Lammert, *Foods*, **11**, 3128 (2022).
49. E. D. G. Danesi, C. D. O. Rangel-Yagui, J. C. M. D. Carvalho, S. Sato, *Biomass Bioenergy*, **26**, 329 (2004).
50. D. A. Marrez, M. M. Naguib, Y. Y. Sultan, Z. Y. Daw, A. M. Higazy, *IJAR.*, **1**, 951 (2013).
51. K. Smarzyński, P. Sarbak, S. Musiał, P. Jeżowski, M. Piątek, P. Ł. Kowalczewski, *Open Agric.*, **4**, 159 (2019).
52. N. Kolev, D. Vlahova-Vangelova, D. Balev, S. Dragoev, K. Dimov, E. Petkov, T. Popova, *Foods*, **13**, 2194 (2024).
53. S. K. Devatkal, P. Thorat, M. Manjunatha, *JFST*, **51**, 2685 (2014).
54. M. A. Shah, S. J. D. Bosco, S. A. Mir, *Meat Sci.*, **98**, 21 (2014).
55. R. Domínguez, M. Pateiro, P. E. Munkata, W. Zhang, P. Garcia-Oliveira, M. Carpena, M. A. Prieto, B. Bohrer, J. M. Lorenzo, *Antioxidants*, **11**, 60 (2021).
56. H. Phetsang, W. Panpipat, I. Undeland, A. Panya, N. Phonsatta, M. Chaijan, *Food Chem.*, **364**, 130365 (2021).
57. S. M. Kim, C. W. An, J. A. Han, *Korean J. Food Sci. Technol.*, **51**, 537 (2019).
58. J. H., Jeon, S. E., Jung, Y. K., Hong, D. H., Lee, T. S. Shin, *JALS.*, **58**, 51 (2024).
59. D. Vlahova-Vangelova, D. Balev, N. Kolev, S. Dragoev, E. Petkov, T. Popova, *Ag.*, **14**, 436 (2024).
60. A. Luo, J. Feng, B. Hu, J. Lv, C. Y. O. Chen, S. Xie, *J. Food Sci.*, **82**, 2591 (2017).
61. I. López-López, S. Bastida, C. Ruiz-Capillas, L. Bravo, M. T. Larrea, F. Sánchez-Muniz, S. Cofrades, F. Jiménez-Colmenero, *Meat Sci.*, **83**, 492 (2009).
62. A. Luo, J. Feng, B. Hu, J. Lv, Q. Liu, F. Nan, C.-Y. Chen, O., S. Xie, *J. Appl. Phycol.*, **30**, 1667 (2018).
63. N. Choi, S. Park, Y. Park, G. Park, S. Oh, Y. A. Kim, Y. Lim, S. Jang, Y. Kim, K. S. Ahn, X. Feng, J. Choi, *Food Sci. Anim. Resour.*, **44**, 817 (2024).
64. D. Aiello, M. Barbera D. Bongiorno, M. Cammarata, V. Censi, S. Indelicato, F. Mazzotti, A. Napoli, D. Piazzese, F. Saiano, *Mol.*, **28**, 699 (2023).
65. J. A. Torres-Castillo, F. E. Olazarán-Santibáñez, *Front. Nutr.*, **10**, 1133342 (2023).
66. A. Schwenzfeier, A. Helbig, P. A., Wierenga, H. Gruppen, *Food Hydrocoll.*, **30**, 258 (2013).
67. A. V. Ursu, A. Marcati, T. Sayd, V. Sante-Lhoutellier, G. Djelveh, P. Michaud, *Bioresour. Technol.*, **157**, 134 (2014).
68. F. Ba, A. V. Ursu, C. Laroche, G. Djelveh, *Bioresour. Technol.*, **200**, 147 (2016).
69. M. A. Pires, P. E. S. Munkata, J. C. Baldin, Y. J. P. Rocha, L.T. Carvalho, I. R. Santos, J. C. Barros, M. A. Trindade, *Food Struct.*, **14**, 1 (2017).
70. J. M. Fernández-Ginés, J. Fernández-López, E. Sayas-Barberá, J. A. Pérez-Alvarez, *J. Food Sci.*, **70**, 37 (2005).
71. M. D. Selgas, E. Cáceres, M. L. García, *Food Sci. Technol. Int.*, **11**, 41 (2005).
72. N. Ktari, S. Smaoui, I. Trabelsi, M. Nasri, R. B. Salah, *Meat Sci.*, **96**, 521 (2014).
73. P. Kaushik A. Chauhan, *Indian J. Microbiol.*, **48**, 348 (2008).

Electrodeposition of Mo-Se thin films and influence of the main factors on their composition

V. A. Majidzade^{1*}, S. F. Jafarova¹, S. P. Javadova¹, A. N. Azizova², S. D. Dadashova¹, A. Sh. Aliyev¹, D. B. Tagiyev¹

¹Ministry of Science and Education of Republic of Azerbaijan, Institute of Catalysis and Inorganic Chemistry named after M. Nagiyev, AZ 1143, H. Javid Ave. 113, Baku, Azerbaijan

²Azerbaijan Medical University, Scientific Research Centre, Baku, Azerbaijan

Received: February 14, 2025; Revised: March 07, 2025

The effects of electrolyte composition and electrolysis regime on the composition of MoSe₂ thin semiconductor films electrodeposited from an aqueous electrolyte containing Na₂MoO₄, H₂SeO₃, and tartaric acid were studied. The results show that with an increase in the concentration of H₂SeO₃, the amount of molybdenum in the obtained films decreases. An increase in the electrolysis time differently affects the composition of the deposited films depending on the current density. An increase in the electrolyte temperature, current density, concentration of Na₂MoO₄, and tartaric acid has a positive effect on the rise of the molybdenum content in the composition of thin films. Using the information gathered, the optimal electrolyte composition and electrochemical deposition technique were determined in order to produce thin films of MoSe₂ with stoichiometric composition.

Keywords: electrodeposition; solar cells; MoSe₂ thin films; semiconductors; tartaric acid

INTRODUCTION

Molybdenum dichalcogenides are semiconductors that act as efficient electrodes in preparing photoelectrochemical solar cells. In them, each layer formed by molybdenum and dichalcogenide atoms is bound by a covalent bond and located in a hexagonal lattice which in the horizontal direction is similar to the structure of graphene. Furthermore, these substances are regarded as layered materials with strong covalent bonding having weak van der Waals interactions between layers.

Obtaining such semiconductors in the form of thin films is extremely important since the use of thin-film materials reduces the material consumption of devices for various purposes.

Compared with MoS₂ [1], MoSe₂ has not caught as much attention, but it also exhibits interesting properties including a direct band gap (1.55 eV) and higher optical absorption [2-5]. MoSe₂ is the only molybdenum chalcogenide that exhibits solid-state cell efficiencies greater than 6%. Its properties make it useful for applications in field-effect transistors (FET), memory devices, photodetectors [6], solar cells [7], electrocatalysts for hydrogen evolution reactions [8], and lithium-ion batteries. The main advantage of these semiconductors is the prevention of corrosion, in other words, phototransistors are associated with the nonbonding d-d orbital of Mo atoms [9].

MoSe₂ is obtained by chemical deposition, hydrothermal synthesis, chemical vapor deposition (CVD), electrodeposition, atomic layer deposition (ALD), molecular-beam epitaxy (MBE), pulsed electrodeposition (PED) [10-18], etc. Compared to the above, the electrochemical deposition method is relatively simple and very economical [19-23]. Its use does not require expensive equipment (including vacuum equipment) and high-temperature annealing operations are excluded. In addition, the method is very environmentally friendly, has high selectivity, and allows deposition on electrode substrates with complex shapes and large sizes. Electrodeposition in potentiostatic or galvanostatic mode makes it possible to obtain thin-film structures.

Thus, the goal of this work is to study the kinetics and mechanism of co-electrodeposition of molybdenum with selenium from tartrate electrolytes, the influence of various factors on the composition and quality of the obtained Mo-Se thin films.

EXPERIMENTAL

Cyclic polarization curves were recorded using an IVIUMSTAT electrochemical interface potentiostat to study the kinetics and mechanism of the process of co-electrodeposition of molybdenum with selenium. In this case, a glass three-electrode electrochemical cell with a volume of 100 ml was

* To whom all correspondence should be sent:
E-mail: yuska_80@mail.ru

used. A nickel plate with an area of 2 cm² was used as a working electrode. The reference electrode was a silver chloride electrode, and the auxiliary electrode was a platinum plate with an area of 4 cm².

The salt of tartaric acid was dissolved in redistilled water for the preparation of the electrolyte. Then, Na₂MoO₄×2H₂O (chemically pure grade, Qualikems Fine Chem Pvt. Ltd., India) and H₂SeO₃ (analytical grade, OOO “Reachem”, Russia) were separately dissolved in the prepared aqueous solution of tartaric acid. The electrolyte has the following composition: (0.15 - 0.27) M Na₂MoO₄ × 2H₂O + 0.007 M C₄H₆O₆ (tartaric acid) and (0.00625 - 0.00125) M H₂SeO₃ + 0.007 M C₄H₆O₆.

X-ray diffraction measurement (XRD) of the obtained thin layers was carried out using a diffractometer "D2 Phaser" from Bruker (filter CuK_α, Ni). The studies of the morphology, relief, and determination of the elemental composition of the electrodeposited Mo-Se samples were carried out by energy-dispersive X-ray spectroscopy (EDX) using “Carl Zeiss Sigma” scanning electron microscope (SEM), as well as by a photocalorimetric method [24].

Prior to the experiments, the surface of Ni electrodes was mechanically ground, treated with dilute

HNO₃ for 30 sec to remove oxide layers, immersed in alcohol or acetone, and finally washed with redistilled water. Electrochemical polishing of the Ni electrodes was carried out in a solution consisting of 55 ml of H₂SO₄, 55 ml of H₃PO₄, and 50 ml of H₂O (T = 293-303K, i = 50 A/dm², τ=180 s), after which the electrodes were rinsed with redistilled water [25]. Electrochemical deposition was carried out in both galvanostatic and potentiostatic modes.

RESULTS AND DISCUSSION

We have previously studied the mechanism and kinetics of the process of electroreduction of molybdate and selenite ions on a Pt electrode [26, 27].

At first, the potentiodynamic polarization curves of the initial components of the test electrolyte were recorded to determine the potential range for the co-deposition of molybdenum with selenium on the Ni electrode (Figs. 1, 2).

In Fig. 1, starting from a stationary potential of -0.13 V, a plateau is observed in the potential range of -0.13(-0.45) V, where electroreduction of molybdate ions occurs according to the Mo (VI) → Mo (IV) → Mo (II) scheme. In the plateau part (1), electroreduction of Mo (VI) ions to Mo (IV) occurs, and in (2), electroreduction of Mo (IV) to Mo (II)

takes place. After -0.45 V, reduction of Mo (II) to Mo (0) occurs. On the reverse direction of the cyclic polarization curve, Mo (0) is oxidized to Mo (IV) and Mo (VI) (peaks 3 and 4), respectively.

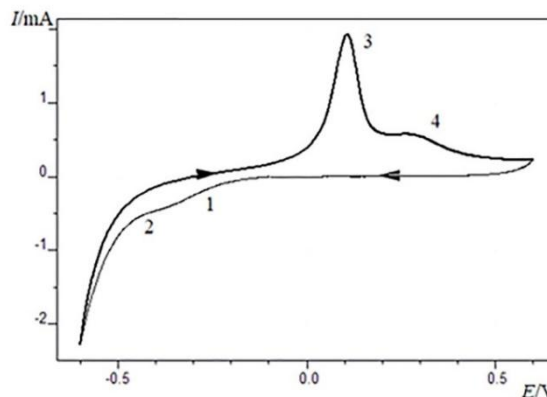


Fig. 1. Cyclic polarization curve of electroreduction of molybdate ions on Ni electrodes. Electrolyte (M): 0.18 Na₂MoO₄×2H₂O + 0.007 C₄H₆O₆; T=298K, E_v=0.04 V/c.

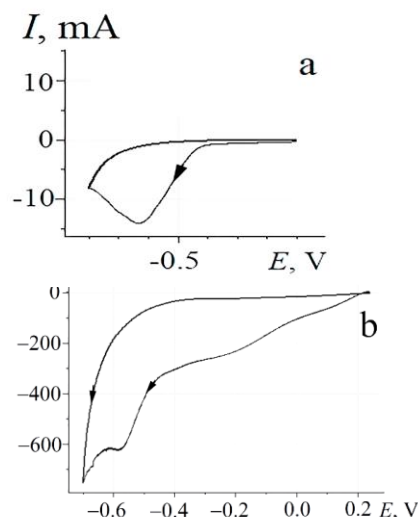


Fig. 2. Cyclic polarization curve of electroreduction of selenite ions on Ni (a) and Ni/Se (b) electrodes. Electrolyte (M): 0.005 H₂SeO₃ + 0.007 C₄H₆O₆; T=298K, E_v=0.04 V/c.

Starting from a stationary potential of 0.24 V, we studied the electroreduction of selenite ions on the surface of Ni (Fig. 2a) and Ni/Se (Fig. 2b), respectively. By studying the mechanism of electroreduction of selenite ions on the Ni electrode it was found that reduction to the selenide ion occurs up to -0.65 V. After -0.65 V, we assume that nickel selenide is formed. Since the formation of Ni-Se is not our goal, we have not studied this in more detail. On the Ni/Se surface (Fig. 2b), the selenite ion is stepwise electroreduced and, besides the above steps, a plateau is observed in the potential intervals -0.05 - (-0.4) V, which indicates the electroreduction of selenite ions to selenium.

The polarization curves of the co-electrodeposition of Mo and Se are shown in Fig. 3.

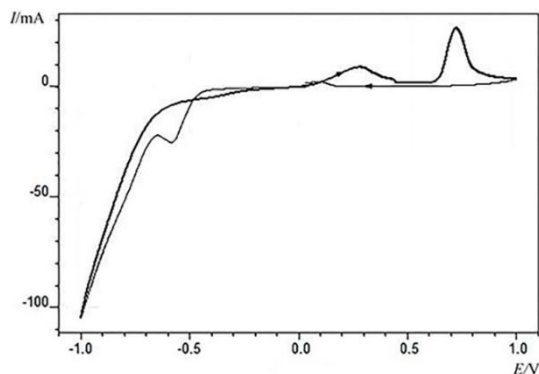


Fig. 3. Cyclic polarization curve of electrodeposition of thin Mo-Se films on Ni electrodes. Electrolyte (M): 0.18 $\text{Na}_2\text{MoO}_4 \times 2\text{H}_2\text{O}$ + 0.005 H_2SeO_3 + 0.007 $\text{C}_4\text{H}_6\text{O}_6$; $T=298\text{K}$, $E_v=0.04 \text{ V/c}$.

As is seen from the figure, on the surface of the Ni electrode, co-deposition occurs in one step in the potential range of 0.03 - (-1.0) V, starting from a stationary potential. A peak starting from -0.4 V and extending to -0.65 V appears on the curve corresponding to Mo-Se co-deposition. Starting from -0.4 V potential, molybdenum and selenium are immediately deposited together due to the formation of Se^{2-} ions in the electrolyte.

The small anodic peak appearing in the 0.1 V zone is related to the reduction of selenite ions. The investigation of the samples obtained on the Ni electrodes by the X-ray phase method, potentiostatic (carried out at -0.58 - (-0.63) V potentials), and galvanostatic (carried out at a current density of 12.5 mA/cm^2) deposition also proves the above (Fig. 4a). In addition, the results of EDX analysis indicate the deposition of both components (Fig. 4c).

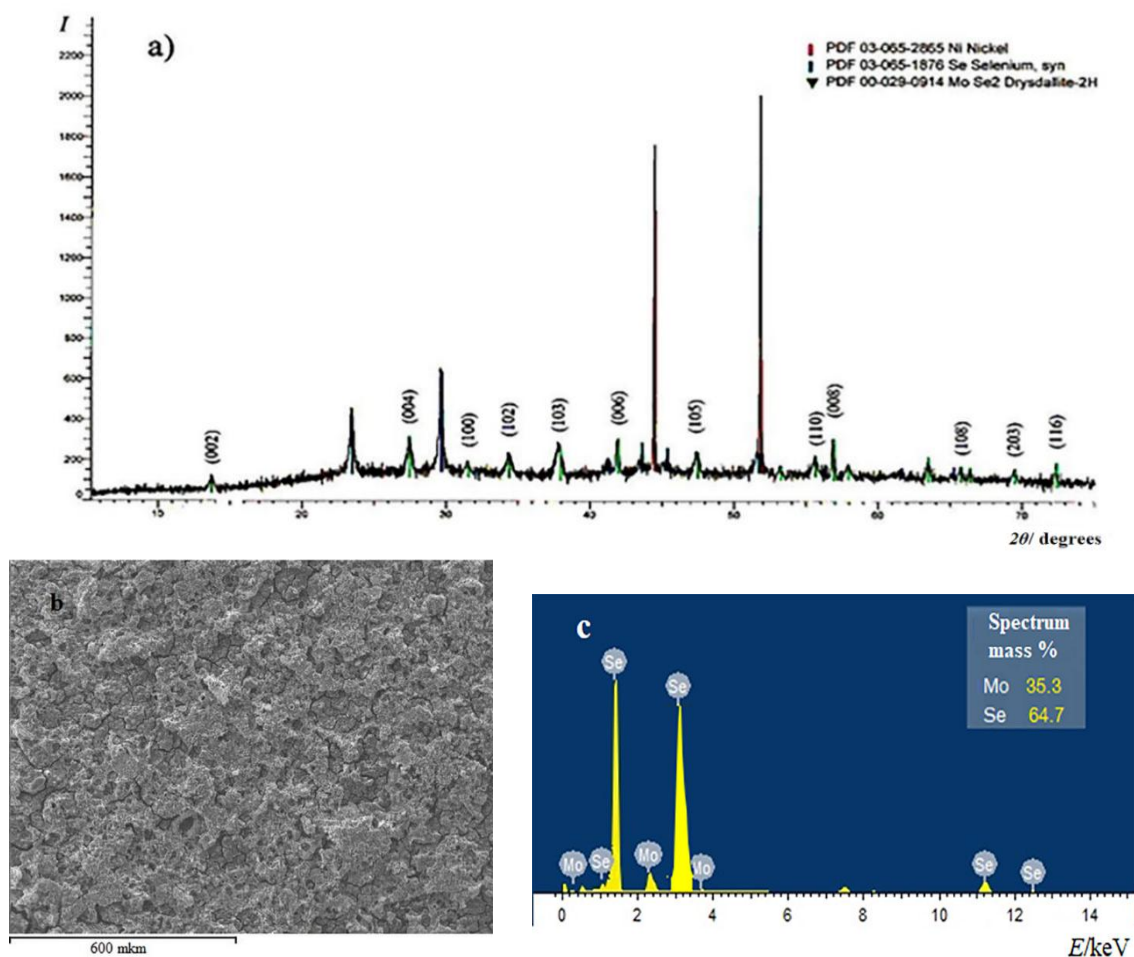


Fig. 4. X-ray diffraction pattern (a), morphology (b) and energy dispersive spectrum (elemental composition) (c) of thin MoSe_2 films deposited from electrolyte (M): 0.18 $\text{Na}_2\text{MoO}_4 \times 2\text{H}_2\text{O}$ + 0.005 H_2SeO_3 + 0.007 $\text{C}_4\text{H}_6\text{O}_6$; $T=298\text{K}$, time of electrolysis 26 h.

Compared to the reference map (PDF 00-029-0914) of MoSe₂, all reflections correspond to planes connected with the 2H-MoSe₂ phase, also called drysdallite [28]. Diffraction peaks (002), (004), (100), (102), (103), (006), (105), (110), (008), (203), (116) observed on the X-ray diffraction pattern (Fig. 3a) at 2θ angles close to ~ 14 °, ~ 28 °, ~ 32 °, ~ 34 °, ~ 38 °, ~ 42 °, ~ 47 °, ~ 53 °, ~ 56 °, ~ 57 °, ~ 66 °, ~ 70 °, and ~ 72 °, respectively, are characteristic of the hexagonal structure of MoSe₂. The distinct peaks observed at 2θ, 44.5°, and 52° belong to the Ni substrate. Here, the deposited MoSe₂ thin films are oriented parallel to the substrate [29-31]. This is the preferred orientation for solar cell applications because perpendicular orientation to the substrate causes high resistance.

Fig. 4(b) shows the morphology of the surface obtained by SEM. The figure demonstrates the uniform deposition of thin Mo-Se films on the electrode surface, resembling flowers with noticeable porosity. In addition, the grain size changes with time. For example, in 19-h samples, grains with a size of 40-50 μm are observed, and in 25-26-h samples the grain size is up to 100 μm. They are homogeneous with a small amount of Se [32, 33].

According to the results of the EDX analysis (Fig. 4c), the films mainly consist of Mo and Se. As is known, the study of the kinetics and mechanism of an electrochemical process plays an important role in the further research of the films.

Finding the potential region of the co-deposition of molybdenum with selenium gives us the opportunity to study the influence of some main factors (concentration of the initial components, temperature, current density, and electrolysis time) on the composition of the obtained films for determination of the optimal electrolyte composition and electrolysis mode. For this purpose, samples of thin films were obtained on Ni electrodes by galvanostatic electrodeposition.

Fig. 5 shows the dependence of the molybdenum content in the obtained thin films on the current density at different concentrations of the initial components within the range of 5-15 mA/cm² current densities.

The results obtained by SEM and photocalorimetric analysis show that thin films with a composition close to stoichiometry are formed from all the above-mentioned electrolytes at different current densities. However, higher-grade films are deposited from an electrolyte with the composition 0.18 Na₂MoO₄ × 2H₂O + 0.005 H₂SeO₃ + 0.007 C₄H₆O₆ at a current density of 12.5 mA/cm². In this case, the amounts of molybdenum and selenium in the deposits are 35.3 % and 64.7 %, respectively (stoichiometric composition: 37.8% Mo and 62.2% Se).

Dispite the fact that with an increase in the current density up to 15 mA/cm², the content of molybdenum in the deposits increases to 50%, both the uniform deposition and the adhesion of the films to the electrode surface deteriorate, and, as a result, the obtained deposits are covering the bottom of the electrochemical cell.

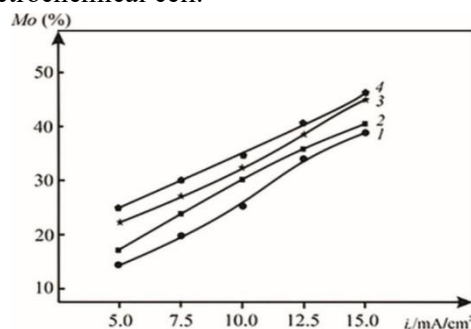


Fig. 5. Dependence of the molybdenum content in electrodeposited thin films on the current density. T = 298K, electrolyte (M): 1. 0.15 Na₂MoO₄ × 2H₂O + 0.00625 H₂SeO₃ + 0.007 C₄H₆O₆; 2. 0.18 Na₂MoO₄ × 2H₂O + 0.005 H₂SeO₃ + 0.007 C₄H₆O₆; 3. 0.24 Na₂MoO₄ × 2H₂O + 0.0025 H₂SeO₃ + 0.007 C₄H₆O₆; 4. 0.27 Na₂MoO₄ × 2H₂O + 0.00125 H₂SeO₃ + 0.007 C₄H₆O₆

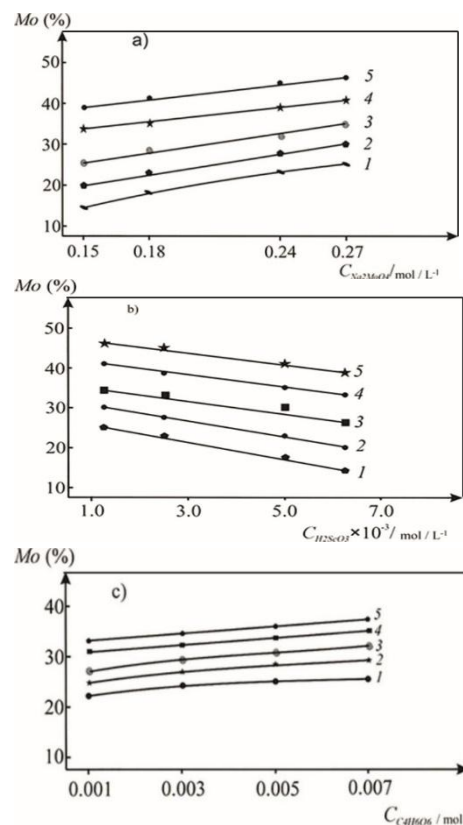


Fig. 6. Dependence of the molybdenum content in electrodeposited thin films on the concentration Na₂MoO₄ × 2H₂O (a), H₂SeO₃ (b) and C₄H₆O₆ (c) in electrolyte (M): Na₂MoO₄ × 2H₂O + H₂SeO₃ + C₄H₆O₆. Current density (mA/cm²): 1-5.0; 2-7.5; 3-10.0; 4-12.5; 5-15.0. T=298K.

The effect of the concentrations of the main components ($\text{Na}_2\text{MoO}_4 \times 2\text{H}_2\text{O}$; H_2SeO_3 ; $\text{C}_4\text{H}_6\text{O}_6$) constituting the electrolyte was studied separately. The concentration of $\text{Na}_2\text{MoO}_4 \times 2\text{H}_2\text{O}$ was 0.15 - 0.27 M, that of H_2SeO_3 $1.25 \times 10^{-3} - 6.25 \times 10^{-3}$ M, and of $\text{C}_4\text{H}_6\text{O}_6$ $10^{-3} - 7 \times 10^{-3}$ M (Fig. 6). As is seen from Figs. 6 (a) and (c), an increase in the concentration of $\text{Na}_2\text{MoO}_4 \times 2\text{H}_2\text{O}$ and $\text{C}_4\text{H}_6\text{O}_6$ in the electrolyte positively affects the composition and quality of the obtained deposits, which cannot be said about H_2SeO_3 . With an increase in the concentration of H_2SeO_3 in the electrolyte, the molybdenum content in the deposits noticeably decreases: from 46.9 % to 39.6 % at 15 mA/cm², and from 24.8 % to 14.8 % at 5 mA/cm². A composition close to the stoichiometric is observed at 0.005 M concentration and at 12.5 mA/cm² current density (Fig. 6b). With an increase in the concentration of tartaric acid in the electrolyte from 0.001 to 0.007 M, the molybdenum content in semiconductor thin films increases depending on the current density: from 22.5 % to 25.4 % at 5 mA/cm², and from 32.8 % to 38.5 % at 15 mA/cm².

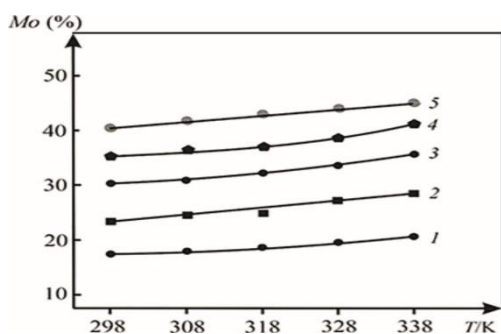


Fig. 7. Dependence of the molybdenum content in thin films on the temperature of the electrolyte. Electrolyte (M): 0.18 $\text{Na}_2\text{MoO}_4 \times 2\text{H}_2\text{O}$ + 0.005 H_2SeO_3 + 0.007 $\text{C}_4\text{H}_6\text{O}_6$. Current density (mA/cm²): 1- 5.0; 2- 7.5; 3- 10.0; 4- 12.5; 5- 15.0

The effect of the electrolyte temperature on the molybdenum content in the obtained thin films was studied in the range of 298-338 K. With an increase in the electrolyte temperature, no intensive change in the proportion of molybdenum in the composition of the cathode films is observed (Fig. 7). A slight increase in the molybdenum content from 35.3 to 41.6 % occurs at an optimal current density of 12.5 mA/cm². The quality, adhesion, and stoichiometry of the electrodeposited films deteriorate with increasing temperature. Therefore, to obtain a uniform, crystalline film with good adhesion, the optimal temperature was chosen as 298 - 308 K.

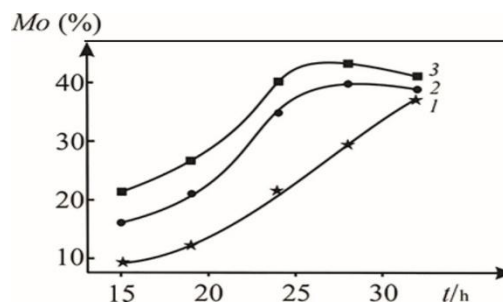


Fig. 8. Dependence of the molybdenum content in thin films on the time of electrolysis. Electrolyte (M): 0.18 $\text{Na}_2\text{MoO}_4 \times 2\text{H}_2\text{O}$ + 0.005 H_2SeO_3 + 0.007 $\text{C}_4\text{H}_6\text{O}_6$. temperature 298 K; current density (mA/cm²): 1- 7.5; 2- 12.5; 3- 15.0.

The results of studying the effect of the electrolysis time on the co-electrodeposition of molybdenum and selenium are shown in Figure 8. As is seen from the figure, at low current densities, the amount of molybdenum in the deposited films sharply increases on increasing the electrolysis time. This also occurs on increasing the current density. But after 24-28 h of electrolysis, the amount of deposited molybdenum in the composition of the film on the electrode surface decreases (Fig. 8, curves 2 and 3). This is due to the poor adhesion of the obtained films to the electrode surface, since, the electrode surface is unevenly covered in poor adhesion and films are deposited on the bottom of the cell.

The study of the effect of the above factors on the co-electrodeposition of molybdenum with selenium showed that electrolysis should be carried out with the following electrolyte composition and electrolysis mode to obtain a uniform, crystalline film close to the stoichiometric composition of MoSe_2 : electrolyte (M): 0.18 $\text{Na}_2\text{MoO}_4 \times 2\text{H}_2\text{O}$ + 0.005 H_2SeO_3 + 0.007 $\text{C}_4\text{H}_6\text{O}_6$; electrolyte temperature 298-308 K; current density 12.5 mA/cm² and electrolysis time 24-28 h. In this mode, the thickness of the deposited thin films is 2-5 μm .

CONCLUSION

The co-deposition process of molybdenum with selenium from tartaric acid electrolytes was investigated by an electrochemical method using Ni electrodes.

It was found that thin films with stoichiometry close to that of MoSe_2 are produced with the optimal electrolyte composition of 0.18 $\text{Na}_2\text{MoO}_4 \times 2\text{H}_2\text{O}$ + 0.005 H_2SeO_3 + 0.007 $\text{C}_4\text{H}_6\text{O}_6$; T=298-308 K; current density - 12.5 mA/cm²; electrolysis time 24-28 h.

Acknowledgement: This work was accomplished with the financial support of the Azerbaijan National Academy of Sciences within the framework of scientific research programs in priority areas.

REFERENCES

1. A.Sh. Aliyev, M. Elrouby, S.F. Cafarova, *Mat. Sci. Semicon. Proc.*, **32**, 31 (2015).
2. S. Tongay, J. Zhou, C. Ataca, K. Lo, T.S. Matthews, J. Li, J.C. Grossman, J. Wu, *Nano Lett.*, **12**, 5576 (2012) DOI: <https://doi.org/10.1021/nl302584w>.
3. M. Bernardi, M. Palummo, J.C. Grossman, *Nano Lett.* **13**, 3664 (2013) DOI: <https://doi.org/10.1021/nl401544y>.
4. H.I. Jeong, S. Park, H.I. Yang, W. Choi, *Mater. Lett.* **253**, 209 (2019) DOI: <http://doi.org/10.1016/j.matlet.2019.06.072>
5. B.K. Choi, M. Kim, K.-H. Jung, J. Kim, K.-S. Yu, Y.J. Chang, *Nanoscale Res. Lett.* **12**, 492 (2017) DOI: <https://doi.org/10.1186/s11671-017-2266-7>
6. A. Balati, A. Bazilio, A. Shahriar, K. Nash, H.J. Shipley, *Mater. Sci. Semicond. Process.* **99**, 68 (2019) DOI: <https://doi.org/10.1016/j.mssp.2019.04.017>
7. J. Bi, J. Ao, L. Yao, Y. Zhang, G. Sun, W. Liu, F. Liu, W. Li, *Mater. Sci. Semicond. Process.* **121**, 105275 (2021) DOI: <https://doi.org/10.1016/j.mssp.2020.105275>
8. Y. Li, Ch. Wang, A. Abdukayum, L. Feng, *Electrochim. Acta.* **503**, 144891 (2024) DOI: <https://doi.org/10.1016/j.electacta.2024.144891>
9. T.J.S. Anand, C. Sanjeeviraja, M. Jayachandran, *Vacuum*, **60**, 431 (2001) DOI: <https://doi.org/10.1016/S0042-207X%2800%2900225-6>
10. L. Jiao, H.J. Liu, J.L. Chen, Y. Yi, W.G. Chen, Y. Cai, J.N. Wang, X.Q. Dai, N. Wang, W.K. Ho, M.H. Xie, *New J. Phys.*, **17**, 053023 (2015)
11. M. Titze, B. Li, P.M. Ajayan, H. Li, Conference on Lasers and Electro-Optics, San Jose, California United States, 13-18 May 2018, Article ID FF1D.3. DOI: https://doi.org/10.1364/CLEO_QELS.2018.FF1D.3
12. S.M. Delphine, M. Jayachandran, C. Sanjeeviraja, *Mater. Res. Bull.*, **40**, 135 (2005) DOI: <https://doi.org/10.1016/j.materresbull.2004.09.008>
13. C.F. Tsang, M.A. Ledina, J.L. Stickney, *J. Electroanal. Chem.* **793**, 242 (2017) DOI: https://www.cheric.org/research/tech/periodicals/doi.php?art_seq=1558222
14. T. Chouki, B. Donkova, B. Aktarla, P. Stefanov, S. Emin, *Mater. Today Commun.* **26**, 101976 (2021) DOI: <https://doi.org/10.1016/j.mtcomm.2020.101976>
15. H. Mittal, M. Khanuja, *Mater. Today: Proceedings.*, **28**, Part 1, 314 (2020) DOI: <http://dx.doi.org/10.1016/j.matpr.2020.02.156>
16. M. Manuraj, S. Jyothilakshmi, K.N. Narayanan Unni, R.B. Rakhi, *J. Mater Sci: Mater Electron.* **31**, 20571 (2020) DOI: <https://doi.org/10.1007/s10854-020-04577-z>
17. T.J.S Anand, T. Mahalingam, C. Sanjeevi Raja, M. Jayachandran, M.J. Chockalingam, Proc. SPIE 3789, Solar Optical Materials XVI, Denver, CO, United States 11 October 1999. DOI: <https://doi.org/10.1117/12.367559>
18. N. Dukstiene, K. Kazancev, I. Proscivevas, A. Guobiene, *J Solid State Electrochem.* **8**, 330 (2004) DOI: <https://doi.org/10.1007/s10008-003-0457-x>
19. A.Sh. Aliyev, Sh.O. Eminov, N.Sh. Soltanova, V.A. Majidzade, D.A. Kuliyeve, H.D. Jalilova, D.B. Tagiyev, *Chemical Problems* **14**, 139 (2016)
20. V.A. Majidzade, A.Sh. Aliyev, İ. Qasimoglu, P.H. Quliyev, D.B. Tagiyev, *Inorganic Materials.* **55**, 979 (2019) DOI: <https://doi.org/10.1134/S0020168519100108>
21. V.A. Majidzade, S.F. Jafarova, I. Kasimoglu, Sh.O. Eminov, A.Sh. Aliyev, A.N. Azizova, D.B. Tagiyev, *Inorganic Materials.* **57**, 331 (2021) DOI: <https://doi.org/10.1134/S0020168521040105>
22. S.P. Javadova, V.A. Majidzade, A.Sh. Aliyev, A.N. Azizova, D.B. Tagiyev, *J. Electrochem. Sci. Eng.* **11**, 51 (2021) DOI: <https://doi.org/10.5599/jese.914>
23. V.A. Majidzade, S.P. Mammadova, E.S. Petkucheva, E.P. Slavcheva, A.Sh. Aliyev, D.B. Tagiyev, *Bulg. Chem. Commun.* **52**, Special Issue E, 73 (2020)
24. A.K. Babko, A.T. Pilipenko, Colorimetric analysis, Goskhimizdat, Moscow, Leningrad, 1951.
25. V.F. Barkovsky, T.B. Gorodentseva, N.B. Toporova, Fundamentals of physical and chemical methods of analysis, M: Higher school, Russia, 1983.
26. V.A. Majidzade, A.Sh. Aliyev, D.M. Babanly, M. Elrouby, D.B. Tagiyev, *Acta Chim. Slov.*, **66**, 155 (2019) DOI: <http://dx.doi.org/10.17344/acsi.2018.4733>
27. V.A. Majidzade, A.Sh. Aliyev, P.H. Guliyev, Y.N. Babayev, M. Elrouby, D.B. Tagiyev, *J. Electrochem. Sci. Eng.* **8**, 197 (2018) DOI: <http://dx.doi.org/10.5599/jese.490>
28. B. Mendoza-Sánchez, J. Coelho, A. Pokle, V. Nicolosi, *Electrochim. Acta.* **192**, 1 (2016) DOI: <https://doi.org/10.1016/j.electacta.2016.01.114>
29. N. Neugebohrn, M.S. Hammer, M.H. Sayed, P. Michalowski, C. Stroth, J. Parisi, M. Richter, *J. Alloys Compd.* **725**, 69 (2017) DOI: <https://doi.org/10.1016/j.jallcom.2017.06.340>
30. J.-H. Yoon, J.-H. Kim, W.M. Kim, J.-K. Park, Y.-J. Baik, T.-Y. Seong, J.-H. Jeong, *Prog. Photovolt: Res. Appl.* **22**, 90 (2014) DOI: <https://doi.org/10.1002/pip.2377>
31. S.Y. Hu, C.H. Liang, K.K. Tiong, Y.C. Lee, Y.S. Huang, *J. Cryst. Growth*, **285**, 408 (2005) DOI: <https://doi.org/10.1016/j.jcrysgro.2005.08.054>
32. J. Wu, B. Li, Y. Shao, X. Wu, W. Zhao, *Environ. Chem. Lett.* **18**, 2141 (2020) DOI: <https://doi.org/10.1007/s10311-020-01048-z>
33. N. Liu, W. Choi, H. Kim, C. Jung, J. Kim, S.H. Choo, Y. Kwon, B.-S. An, S. Hong, S. So, C.-W. Yang, J. Hur, S. Kim, *Nanoscale.* **12**, 6991 (2020) DOI: <https://doi.org/10.1039/C9NR10418F>

¹Research on the potential of postbiotics in soaps for improving their quality and functionality

N. Delinska^{1*}, M. Perifanova-Nemska¹, D. Blazheva², A. Slavchev²

¹Department of Technology of Tobacco, Sugar, Vegetable and Essential Oils, Technological Faculty, University of Food Technologies, 26 Maritza Blvd., Plovdiv, Bulgaria

²Department of Microbiology and Biotechnology, Technological Faculty, University of Food Technologies, 26 Maritza Blvd., Plovdiv, Bulgaria

Received: March 17, 2025; Revised: May 13, 2025

Postbiotics are metabolites of probiotic microorganisms that, unlike probiotics, do not contain live cells. This gives them greater stability and safety, making them promising for use in soap formulations. Postbiotics can enrich soaps with new functionalities, e.g., supporting the maintenance of the skin microbiome, improving hydration levels and strengthening the skin's barrier function. The present study examines their compatibility with soap ingredients and their potential as innovative cosmetic ingredients. The study aims to investigate how postbiotics can provide soaps with additional skin benefits, positioning them as innovative products in the personal care market.

Keywords: postbiotics, soaps, skin benefits

INTRODUCTION

In recent years, the personal care industry has undergone significant changes in consumer preferences. There is a growing preference for products with high-quality, safe and environmentally sustainable ingredients. In response to these demands, companies are developing innovative solutions, incorporating biodegradable packaging, organic ingredients and adopting ethical production standards. Within this context, postbiotics are emerging as a valuable and promising cosmetic ingredient.

Soap formulation presents a challenge when incorporating active ingredients due to the high pH and the need for chemical stability and ingredient compatibility. However, to achieve the desired functionality and market appeal of soaps, various additives are used, including emollients, moisturizers, antibacterial agents and bioactive compounds [1–11].

Postbiotics also have the potential to be incorporated as an effective and innovative ingredient in soaps. They are non-living microorganisms and/or their metabolites that provide health benefits to the host [12]. These ingredients do not require viability, exhibit greater stability under various conditions, and are not subject to the same regulatory requirements for microbiological safety as probiotics, according to Cosmetics Regulation No 1223:2009 [13] and ISO 17516:2014 [14].

With the growing understanding of the skin

microbiome, postbiotics are establishing themselves as a valuable resource in cosmetics [15–18]. They contain metabolites such as short-chain fatty acids, exopolysaccharides, vitamins, teichoic acids, bacteriocins, enzymes, peptides, etc. [12, 19–21], which are used in the form of lysates, enzymes, extracts, and others [22, 23]. Postbiotics exhibit antioxidant, anti-inflammatory and immunomodulatory properties [18, 24–29], they have a longer shelf life and do not require viability in the topical formula, making them more stable and convenient for use in cosmetic products.

Their mechanisms of action can be direct (affecting skin cells) or indirect (stimulating beneficial microorganisms and inhibiting pathogens) [16]. They contribute to creating conditions that can limit skin infections and inflammation [30–34], support the treatment of acne, eczema and rosacea [15, 35, 36] and help improve skin hydration and barrier function [37–40].

The aim of this study is to examine the potential applications of postbiotics in soaps, with a focus on improving their functionality and impact on the skin. The research focuses on the effect of using postbiotic-enriched soaps on skin hydration and strengthening its microbial defenses.

The study used a postbiotic derived from *Limosilactobacillus reuteri*, a microorganism known for its ability to produce reuterin – a potent antimicrobial metabolite that effectively inhibits various pathogens [41–44]. In addition to reuterin, certain strains of *L. reuteri* are also sources of other antimicrobial compounds, including lactic acid,

* To whom all correspondence should be sent:
E-mail: nikolaja@abv.bg

acetic acid, ethanol, and reutericyclin [45]. Among the other bioactive substances, characteristic of this species are compounds that help restore skin balance and reduce inflammation [45–47]. The stability of the postbiotic across a wide pH range, combined with its beneficial properties, makes it a suitable functional ingredient for inclusion in soaps.

MATERIALS AND METHODS

Materials

The studies were conducted on solid and liquid soaps produced using a cold method, with postbiotics at different concentrations. A probiotic strain of *L. reuteri* was used, provided by the private collection of Cryobiotica Ltd.

Culture medium for obtaining the postbiotic concentrate: A solution of skimmed milk powder was prepared and whey protein was added until a concentration of 50% was reached. The resulting solution was then diluted to 15%, and 0.45% of yeast extract was added. The prepared culture medium was sterilized at 121°C for 20 min.

The formulation of the solid soap included palm oil, coconut oil (N. Pavlos, S. A. Pettas, Greece) and varying concentrations of *L. reuteri*. The saponification agent used was NaOH in the form of microbeads with a concentration of 98-99% (manufacturer: INOVYN Europe Limited). For the liquid soap, coconut oil and varying concentrations of *L. reuteri* postbiotic were used. The saponification agent used was 90%KOH in flakes (importer: Safik-Alkan Himsnab AD; manufacturer: SPOLCHEMIE, Czech Republic).

Methods

The probiotic microorganism *L. reuteri* was cultured in a medium for obtaining postbiotic concentrates at 37°C for 16-18 hours. The resulting culture medium was heated to 45°C, homogenized in a batch homogenizer at 400 bar, and then lyophilized in a Biobase BK-FD18P freeze dryer for 24 hours. The culture medium was previously frozen to -42 °C. Lyophilization was carried out at a working pressure of 20 Pa. The final product contains 1-4% of water.

The saponification of the oil mixture for the solid soaps was carried out in laboratory conditions using sodium hydroxide, following the method described in [48]. The appropriate amount of postbiotic concentrate was added to the soap mass. After thorough mixing, the soap mixture was poured into silicone molds and stored at room temperature (25°C) for a period of three to four weeks.

A formulation for the production of liquid soaps with coconut oil and *L. reuteri* postbiotic was also developed. The saponification of the oil mixtures

was performed in laboratory conditions. The liquid soap mass was cooled to a temperature of 20±2°C for 24 hours and then dispensed into bottles. A control sample (without postbiotic) was also prepared for analysis.

The soap analysis included the determination of the following physical and chemical parameters: moisture content (ISO 672:1978) [49]; free caustic alkali content (ISO 456:1973) [50]; total fatty matter content (ISO 685:2020) [51]; foaming ability (ISO 696:1975) [52]; pH (ISO 4316:1977) [53] and sensory characteristics. The sensory analysis involved evaluating the opinions of the panelists after the application of the products. The test was designed to compare the effects of different soaps (solid and liquid, with and without postbiotics) on the skin. It aimed to examine how these differences affect key indicators such as skin hydration, sensation of softness, lack of irritation, as well as foaming, hardness, soap durability and overall perception after product use.

The consumer test involved 30 panelists with healthy skin, aged between 25 and 60 years, 70% of whom were women and 60% having normal skin (as determined through self-assessment). The test was conducted in home conditions over a period of 30 days, with each product being used twice daily – in the morning and evening – for washing the hands.

Hydration was measured through the subjective feeling of moisture retention in the skin after each use. This indicator reflects how the skin feels after applying the soap – whether it is smooth, soft and comfortable, or dry and tight. The absence of irritation was assessed by observing signs of redness, itching, or other skin reactions. Foaming was evaluated based on the quantity and density of the foam, while hardness and durability referred to the soap's endurance during use and its ability to maintain its shape. The overall perception summarized the ratings for all of these characteristics.

Data were collected through surveys completed after the use of each product, with ratings given on a scale from 1 to 5. This methodology ensured a detailed and objective evaluation of the products based on real consumer experiences.

RESULTS AND DISCUSSION

Tables 1 and 2 present the results of the analysis of solid and liquid soaps, respectively. №1A and №2A are control samples (without postbiotic), while samples №1B, №2B, №1C and №2C contain 0.1% and 0.2% of postbiotic preparation, respectively.

The results indicated that the addition of *L. reuteri* postbiotics to solid soaps affects some of

their physicochemical properties. The foaming capacity decreased by approximately 6-7%, which could be due to interactions between the postbiotic and surfactant components. The moisture content in the samples ranged between 18.1% and 20.4%, with the postbiotic-containing samples retaining more moisture compared to the control. This suggests a potential hydrating effect of the postbiotic.

The addition of postbiotics did not significantly affect the pH or the content of free alkalis, indicating that the saponification process is complete and the stability of the product is not compromised. The fatty acid content slightly decreased with an increase in postbiotic concentration, but the differences were not significant.

In conclusion, the postbiotic can be incorporated into solid soap formulations, contributing to a potentially enhanced hydrating effect without compromising the primary characteristics of the product.

The solid soap samples have different colors, as seen in Figure 1. This is a result of the variations in the amount of postbiotic contained in them.

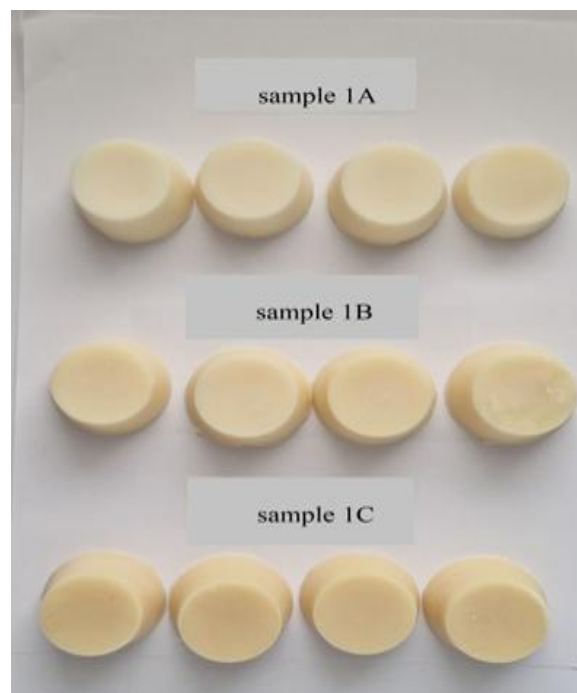


Fig. 1. Solid soap samples – (1A) control, (1B) and (1C) containing 0.1% and 0.2% postbiotic, respectively.

The darkest color is observed in sample №1C which contains the highest amount of postbiotic (0.2%). The control sample №1A stands out with a clean and lighter color.

Table 1. Results of the analyzed solid soap samples.

Sample	Moisture content, %	Total fatty matter content, %	Foaming ability, cm ³ after 30 s	pH	Free alkali, %
№1A	18.1±0.1	61.2±0.3	150.0±5.0	10.1±0.1	0.06±0.003
№1B	19.5±0.2	62.3±0.3	140.0±3.0	10.2±0.1	0.04±0.002
№1C	20.4±0.2	63.5±0.2	140.0±4.0	10.3±0.1	0±0.004

Table 2. Results of the analyzed liquid soap samples.

Sample	Free alkali, %	Foaming ability, cm ³ after 30 s	pH	Appearance
№2A	0	210.0±6.0	9.2±0.1	Transparent liquid
№2B	0	200.0±6.0	9.2±0.1	Semi-transparent liquid
№2C	0	180.0±3.0	9.0±0.1	Semi-transparent liquid

Table 3. Consumer test results for solid soaps

Sample	Hydration	Lack of irritation	Foaming ability	Hardness	Overall perception
№1A	avg. 3.20	4.50	4.30	4.60	3.75
№1B	avg. 3.60	4.50	4.30	4.50	4.05
№1C	avg. 3.80	4.90	4.10	4.60	4.10

The results of the analysis of the liquid soaps indicated that the addition of *L. reuteri* postbiotic leads to changes in some of their characteristics. The foaming ability decreased with an increase in the postbiotic concentration – sample №2B showed a decrease of approximately 5%, while sample №2C experienced a 14% reduction compared to the control sample №2A.

The pH values of all samples remained within a narrow range (9.0-9.2), indicating that the addition of postbiotics does not significantly affect the alkalinity of the product. All samples have zero free alkali content, confirming the complete saponification of the oils.

A significant difference was observed in the appearance of the samples. While the control sample №2A is a transparent liquid, the postbiotic-containing samples №2B and №2C are semi-transparent (Figure 2). This indicates that the addition of postbiotics affects the optical properties of the liquid soap, likely due to the solubility or interactions of the postbiotic preparation with the other components. The difference in adding postbiotics to liquid soaps is mainly expressed in the reduction of foaming ability and the change in the appearance of the product.

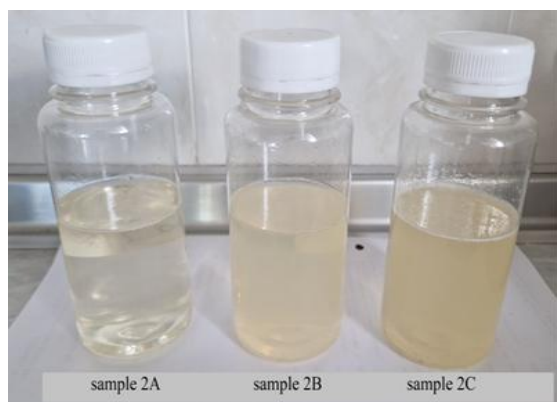


Fig. 2. Liquid soap samples – (2A) control, (2B) and (2C) containing 0.1% and 0.2% of postbiotic, respectively.

In conclusion, the addition of *L. reuteri* postbiotic to soap formulations did not lead to significant changes in the main physicochemical properties of the soap. Good compatibility with the ingredients was observed, without compromising the product's quality. This makes the postbiotic suitable for inclusion in soap formulations.

Table 4. Consumer test results for liquid soaps

Sample		Hydration	Lack of irritation	Foaming ability	Overall perception
№2A	avg.	3.50	4.40	4.70	3.90
№2B	avg.	3.60	4.60	4.60	4.10
№2C	avg.	3.70	4.50	4.60	4.10

The data presented in Table 3 come from consumer tests on solid soaps with postbiotics. The evaluated indicators determine the quality and overall perception of the soap by users. These factors play an important role in product evaluation, as they reflect both functional and aesthetic characteristics, which are significant to the end consumer.

Participants noted a difference in the moisture feeling after using soaps with postbiotics compared to those without. Products with higher concentrations of postbiotics demonstrated better ability to keep the skin smooth and soft after use. Sample №1C showed the highest value (3.80), indicating better hydration compared to samples №1A (3.20) and №1B (3.60). This suggests that the postbiotic in sample №1C may have a stronger effect on skin hydration.

Perceptions of irritation were relatively consistent for all samples (between 4.50 and 4.90), indicating that the addition of postbiotic does not lead to skin irritation. None of the products caused redness or itching in participants. This shows good tolerance for all tested soaps.

Regarding the foaming ability, samples №1A and №1B received the same rating (4.30), while sample №1C had a slightly lower value (4.10). This could suggest that the addition of postbiotic slightly reduces the foaming ability.

No significant changes in the hardness or erosion of the soaps were observed with the increasing concentration of postbiotic. The overall product rating combines all aspects of the consumers' perceptions regarding the soap's qualities and can be considered as an indicator of overall satisfaction with the product.

The majority of participants gave a high rating for the 'overall perception' of the soaps with postbiotics, highlighting the better feeling of hydration and skin comfort compared to the other samples.

In summary, the postbiotic has a positive effect on hydration and does not cause irritation while slightly reducing foamability, but it does not significantly impact the hardness or erosion of the soap.

Table 4 presents data from the sensory evaluation tests for the three liquid soap samples.

The participants in the test indicated that regular use of the product with postbiotics contributes to visibly better hydrated and smoother skin compared to the control sample. The products with postbiotics (№2B and №2C) received high ratings for the absence of irritation, as consumers did not experience redness or itching. The foaming ability of these products was rated as providing additional comfort and hydration.

CONCLUSION

Postbiotics represent an innovative and effective ingredient that can be integrated into soap formulations, opening new opportunities for development in the cosmetics industry. The results of the study show that the addition of postbiotics to soaps does not lead to unwanted changes in their core qualities, but may provide additional skin benefits, such as hydration and strengthening of the skin barrier. Although soaps are rinse-off products, the inclusion of a postbiotic suggests the potential for continued skin benefits after regular use, as a result of a cumulative effect. The use of postbiotics adds additional functionality and may contribute to successful market positioning of the products. Based on the promising results, further instrumental studies are needed to confirm the dermatological effects and the optimal conditions for the application of postbiotics in soap formulation.

Acknowledgement: This research is supported by the Bulgarian Ministry of Education and Science under the National program “Young Scientists and Postdoctoral Students - 2”.

REFERENCES

1. O. Adigun, C. Manful, N. P. Vidal, A. Mumtaz, T. H. Pham, P. Stewart, M. Nadeem, D. Keough, R. Thomas, *Antioxidants*, **8**, 536 (2019), doi: org/10.3390/antiox8110536.
2. A. K. Arsa, Z. Achmad, *J. Techno*, **7**, 163 (2021).
3. S. Dwiyantri, S. Sulandjari, D. S. Megasari, N. Kusstanti, M. Faidah, S. Usodoningtyas, *Int. Joint Conf. Sci. Eng. (IJCSE)*, **196**, 348 (2020), doi: 10.2991/aer.k.201124.063.
4. H. Mawarti, M. Rajin, A. Zakaria, D. E. Purwati, *Proc. 2nd ASEAN Plus Three Graduate Research Congress (2nd AGRC)*, Bangkok, February 5-7, 2014, p. 370.
5. B. T. Pamungkas, A. Safitri, F. Rezaldi, M. Andry, L. D. Agustiansyah, M. F. Fadillah, F. Hidayanto, H. Hariadi, *BIOTIK: Jurnal Ilmiah Biologi Teknologi dan Kependidikan*, **10**, 179 (2022).
6. Y. E. Pratama, S. Melia, E. Purwati, *Proc. IOP Conf. Ser.: Earth Environ. Sci.*, **694**, 012075 (2021), doi: 10.1088/1755-1315/694/1/012075.
7. I. P. Sany, A. S. Fahmi, *IOP Conf. Ser.: Earth Environ. Sci.*, **246**, 012066 (2019), doi: 10.1088/1755-1315/246/1/012066.
8. S. Félix, J. Araújo, A. M. Pires, A. C. Sousa, *Waste Management*, **66**, 190 (2017).
9. E. D. George, D. J. Raymond, in: Soap manufacturing technology, L. Spitz (ed.), AOCS Press, 2016, p. 55.
10. S. Handayani, S. Kristianingrum, A. Rakhmawati, *Orient. J. Chem.*, **34**, 2410 (2018), doi: 10.13005/ojc/340524.
11. A. D. Susanti, S. Saputro, W. A. Wibowo, *Equilibrium J. Chem. Eng.*, **2**, 53 (2018).
12. S. Salminen, M. C. Collado, A. Endo, C. Hill, S. Lebeer, E. Quigley, M. E. Sandres, R. Shamir, J. R. Swann, H. Szajewska, G. Vinderola, *Nat. Rev. Gastroenterol. Hepatol.*, **18**, 649 (2021), doi: 10.1038/s41575-021-00440-6.
13. Regulation (EC) No 1223/2009 of the European Parliament and of the Council, of 30 November 2009, on Cosmetic Products, *Official Journal of the European Union*, **L342**, 59 (2009).
14. ISO 17516:2014. Cosmetics — Microbiology — Microbiological limits.
15. C. V. De Almeida, E. Antiga, M. Lulli, *Microorganisms*, **11**, 1420 (2023), doi: 10.3390/microorganisms11061420.
16. A. da Silva Vale, G. V. de Melo Pereira, A. C. de Oliveira, D. P. de Carvalho Neto, L. W. Herrmann, S. G. Karp, V. T. Soccol, C. R. Soccol, *Fermentation*, **9**, 264 (2023), doi: 10.3390/fermentation9030264.
17. M. Majeed, S. Majeed, K. Nagabhushanam, L. Mundkur, H. R. Rajalakshmi, K. Shah, K. Beede, *Cosmetics*, **7**, 70 (2020), doi: 10.3390/cosmetics7030070.
18. T. Ciardiello, D. Pinto, L. Marotta, G. Giuliani, F. Rinaldi, *Cosmetics*, **7**, 34 (2020), doi: 10.3390/cosmetics7020034.
19. B. H. Nataraj, S. A. Ali, P. V. Behare, H. Yadav, *Microb. Cell Fact.*, **19**, 1 (2020), doi: 10.1186/s12934-020-01426-w.
20. E. Scott, K. De Paepe, T. Van de Wiele, *Biomolecules*, **12**, 1640 (2022), doi: 10.3390/biom12111640.
21. C. A. M. Wegh, S. Y. Geerlings, J. Knol, G. Roeselers, C. Belzer, *Int. J. Mol. Sci.*, **20**, 4673 (2019), doi: 10.3390/ijms20194673.
22. W. Mohammedsaeed, S. Cruickshank, A. J. McBain, C. A. O'Neill, *Scientific Reports*, **5**, 16147 (2015), doi: 10.1038/srep16147.
23. S. Puebla-Barragan, G. Reid, *Molecules*, **26**, 1249 (2021), doi: 10.3390/molecules26051249.
24. J. Żółkiewicz, A. Marzec, M. Ruszczynski, W. Feleszko, *Nutrients*, **12**, 2189 (2020).
25. B. Liang, D. Xing, *Probiotics Antimicrob. Proteins*, **15**, 1626 (2023), doi: 10.1007/s12602-023-10045-x.
26. H. Cui, C. Feng, T. Zhang, V. Martínez-Ríos, P. Martorell, M. Tortajada, S. Cheng, S. Cheng, Z. Duan, *Sci. Rep.*, **13**, 16879 (2023), doi: 10.1038/s41598-023-43336-y.
27. M. Duarte, A. L. Oliveira, C. Oliveira, M. Pintado, A. Amaro, A. R. Madureira, *Appl. Microbiol.*

- Biotechnol.*, **106**, 5879 (2022), doi: 10.1007/s00253-022-12116-5.
28. A. Martyniak, A. Medyńska-Przęczek, A. Wędrychowicz, S. Skoczeń, P. J. Tomasik, *Biomolecules*, **11**, 1903 (2021), doi: 10.3390/biom11121903.
 29. E. Patil, B. Rawtal, S. Sakharwade, *World J. Pharm. Res.*, **9**, 404 (2020), doi: 10.20959/wjpr202011-18670.
 30. M. Fourrière, T. Latire, D. Souak, M. G. J. Feuilloley, G. Bedoux, *Microorganisms*, **8**, 1752 (2020), doi: 10.3390/microorganisms8111752.
 31. S. Oh, S.-H. Kim, Y. Ko, J.-H. Sim, K. S. Kim, S.-H. Lee, S. Park, Y. J. Kim, *Food Chem. Toxicol.*, **44**, 552 (2006), doi: 10.1016/j.fct.2005.08.008.
 32. L. Huuskonen, H. Anglenius, I. Ahonen, K. Tiihonen, *Microorganisms*, **11**, 1465 (2023), doi: org/10.3390/microorganisms11061465.
 33. N. Golkar, Y. Ashoori, R. Heidari, N. Omidifar, S. N. Abootalebi, M. Mohkam, A. Gholami, *J. Evidence-Based Complementary Altern. Med.*, **4**, 1 (2021), doi: 10.1155/2021/8577116.
 34. I. Castiel, L. Breton, A. Gueniche, *U.S. Patent* 10 238 897 (2019).
 35. M. Jesenak, S. Urbancek, J. Majtan, P. Banovcin, J. Hercogova, *J. Dermatol. Treat.*, **27**, 351 (2016).
 36. H. Cui, C. Guo, Q. Wang, C. Feng, Z. Duan, *Front. Med.*, **9**, 1064460 (2022), doi: 10.3389/fmed.2022.1064460.
 37. J. Kim, Y. Lee, S. Mun, J. Jeong, D.-G. Lee, M. Kim, H. Jo, S. Lee, K. Han, J. Lee, *Int. J. Mol. Sci.*, **24**, 4634 (2023), doi: 10.3390/ijms24054634.
 38. K. M. Kim, J.-W. Song, C.-W. Lee, D.-S. Kim, J. Sohn, S. Lee, *J. Microbiol. Biotechnol.*, **34**, 65 (2023), doi: 10.4014/jmb.2306.06042.
 39. T. Catic, B. Pehlivanovic, N. Pljakic, A. Balicevac, *Med. Arch.*, **76**, 108 (2022), doi: 10.5455/medarh.2022.76.108-114.
 40. L.-C. Lew, M.-T. Liang, *J. Appl. Bacteriol.*, **114**, 1241 (2013), doi: 10.1111/jam.12137.
 41. A. K. Niamah, A. A. Mohammed, N. A. Alhelf, *J. Microbiol. Biotechnol. Food Sci.*, **12**, 4701 (2023).
 42. S. Jeznienė, PhD Thesis, KTU, Kaunas, 2024.
 43. M.-C. Sun, Z.-Y. Hu, D.-D. Li, Y.-X. Chen, J.-H. Xi, C.-H. Zhao, *Foods*, **11**, 4000 (2022).
 44. M. Bakhshi, S. Salari, P. G. N. Almani, S. A. K. Afshari, *Gene Rep.*, **25**, 101369 (2021).
 45. Q. Mu, V. J. Tavella, X. M. Luo, *Front. Microbiol.*, **9**, 757 (2018).
 46. I. Khmaladze, É. Butler, S. Fabre, J. M. Gillbro, *Exp. Dermatol.*, **28**, 822 (2019).
 47. K. Jonas, M. Mukarram, G. Herrick, K. Frasier, V. Li, *Ameri. J. Clin. Med. Re: AJCMR* **150**, **4**, (2024).
 48. M. Perifanova-Nemska, N. Delinska, E. Dimitrova, *8th Int. Conf. Energy Efficiency and Agricultural Engineering (EE&AE)*, **1** (2022), doi: 10.1109/EEAE53789.2022.9831262.
 49. ISO 672:1978. Soaps — Determination of moisture and volatile matter content — Oven method.
 50. ISO 456:1973. Surface active agents — Analysis of soaps — Determination of free caustic alkali.
 51. ISO 685:2020. Analysis of soaps — Determination of total alkali content and total fatty matter content.
 52. ISO 696:1975. Surface active agents — Measurement of foaming power — Modified Ross-Miles method.
 53. ISO 4316:1977. Surface active agents — Determination of pH of aqueous solutions — Potentiometric method.

Sustainable design approach of a hydrogen production supply chain through water electrolysis

E. Ganev¹, D. Nikolova^{2*}, E. Kirilova¹, R. Vladova¹, V. Beschkov¹, T. Valkanova², B. Burdin³, E. Slavcheva³, J. Iliev³

¹*Institute of Chemical Engineering, Bulgarian Academy of Sciences, Acad. G. Bontchev Str., Bl. 103, 1113 Sofia, Bulgaria*

²*Burgas State University "Prof. Dr. Asen Zlatarov", 1, Prof. Yakim Yakimov Blvd., 8010, Burgas, Bulgaria*

³*Institute of Electrochemistry and Energy Systems "Acad. Evgeni Budevski", Bulgarian Academy of Sciences, Acad. G. Bontchev, Str., Bl. 10, 1113 Sofia, Bulgaria*

Received: April 29, 2025; Accepted: May 13, 2025

Among the many alternative energy sources, hydrogen emerges as a key vector in the future energy mix due to its flexibility, high energy content, and significant potential for decarbonization. Among the various hydrogen production methods, electrolysis stands out as a promising and sustainable solution. However, realizing the full potential of hydrogen as a transportation fuel requires the development of an efficient and sustainable supply chain infrastructure capable of addressing the unique challenges associated with production, storage, transportation, and distribution.

This study focuses on developing a mathematical model for the sustainable design of a hydrogen supply chain produced through electrolysis. The proposed model is formulated within the framework of mixed-integer linear programming. A generalized superstructure of a resource-secured hydrogen supply chain, obtained through the electrolysis process, is presented.

Keywords: supply chain, GHG, hydrogen, electrolysis, hydrogen fuel cell vehicle

INTRODUCTION

Globally, hydrogen is well known as a sustainable energy source that can help bring the world closer to achieving net zero emissions (NZE) by 2050. It is also considered a promising energy carrier for decarbonizing a wide range of industrial sectors, transportation, and heating [1]. For this reason, in recent years, the concept of using hydrogen as an energy carrier has been gaining increasing popularity. Significant progress has been made in overcoming the technological and economic barriers to its large-scale implementation, making hydrogen an increasingly accessible solution [2]. Moreover, hydrogen is known as one of the few energy carriers capable of meeting the energy demands of many energy-intensive and hard-to-abate sectors, while its consumption is associated with zero emissions. The use of hydrogen as a fuel is crucial for reducing emissions in the transportation sector.

Depending on the level of hydrogen production "sustainability" and the primary energy source, a "color" classification has been introduced. The technologies for producing so-called "green" hydrogen are identified as the cleanest, resulting in zero emissions. This implies the generation of

hydrogen using renewable energy sources (RES), as it does not involve greenhouse gases and is environmentally clean [3].

This type of hydrogen is considered a potential solution to overcoming the barriers in the transition to a sustainable future. The high cost, uneven distribution, and insufficient amount of energy from RES hinder its commercial use in hydrogen production for the needs of modern industry and transportation. On the other hand, hydrogen production using nuclear energy could also be considered a potential low-carbon technology. Hydrogen production using nuclear energy can generally be achieved through five methods: hybrid thermochemical water splitting, high-temperature steam electrolysis, radiolysis, and electrolysis.

To split water into hydrogen and oxygen, radiolysis uses nuclear radiation; electrolysis uses electricity generated from nuclear energy; high-temperature steam electrolysis and hybrid thermochemical water splitting are referred to as hybrid methods, as they split water using both electricity and high-temperature heat; and thermochemical water splitting directly uses high-temperature heat [4].

*To whom all correspondence should be sent:

E-mail: desislava_nikolova@btu.bg

The low-emission hydrogen market is expected to grow by 70% by 2030 [5]. It is believed that a mixture of 15% by volume of hydrogen and compressed natural gas (CNG) will reduce carbon dioxide (CO₂) emissions from the use of gas by 6% globally. The net zero emissions (NZE) scenario significantly alters hydrogen production. By generating 200 million tons of hydrogen by 2030, it is expected that around 70% of this will be the result of electrolysis, which could lead to a reduction in carbon dioxide emissions. By 2050, approximately 500 million tons of hydrogen will be produced using advanced low-carbon technologies. To achieve these goals, the installed capacity of electrolysis must be maximized from its current level of 0.3 GW to approximately 850 GW and 3600 GW by 2030 and 2050, respectively. Between 2022 and 2030, the generated CO₂ per kg of hydrogen will decrease from 12-13.5 kg to 6-7.5 kg.

Although with great potential, the hydrogen industry is still in its early stages of development and faces various challenges. They include low production efficiency, high storage and transportation costs, and, not least, an unbalanced supply and demand structure. Therefore, it is crucial to develop a model for designing the hydrogen supply chain infrastructure (HSC) to support the sustainable development of the hydrogen industry and its application in the transportation sector. In this context, there has been an increase in research interest in the field of HSC by about 8-9 times [6], Figure 1.

In their developments, the author teams researching this topic have reported literature reviews, studies, analyses, comparisons, research, technological solutions, and mathematical models for optimal design of HSC.

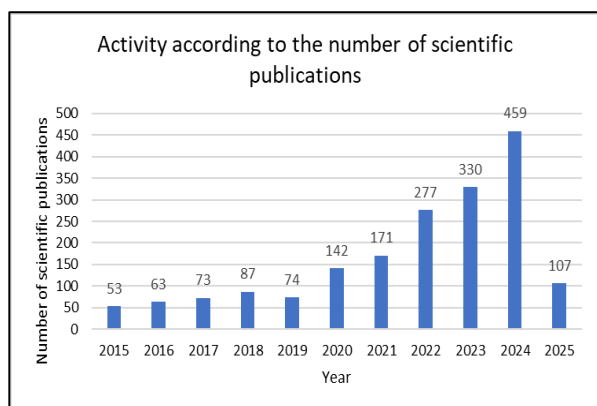


Figure 1. Activity according to the number of scientific publications related to hydrogen supply chain for the period 2015 – 2025.

Studies related to mathematical models describing HSC infrastructure can be divided into

two categories [7]. The first category of research is related to the development of mathematical models for optimal design of the HSC. These models mainly focus on the production, transportation, and storage of hydrogen, offering solutions regarding the location and capacity of the infrastructure. The second category of research mainly focuses on developing mathematical models describing the location of hydrogen refueling stations, aiming to meet the requirements of fuel cell vehicles while considering the capacity of the stations. In cases where refueling stations are considered, the required electrical energy mostly comes from the main power grid, which facilitates decision-making [8]. There are no known developments in the literature offering solutions for the sustainable design of an HSC produced through electrolysis, taking into account the location and capacity of refueling stations.

This study presents a generalized model for the optimal design of an HSC, produced through the electrolysis process, simultaneously considering the three aspects of sustainability—economic, environmental, and social. The developed model is formulated in terms of mixed-integer linear programming (MILP) and could be solved using specialized optimization software, such as GAMS.

COLOR CLASSIFICATION OF HYDROGEN

At standard temperature and pressure, hydrogen is a colorless, non-toxic, tasteless, and highly flammable diatomic gas with the molecular formula H₂. Depending on the method of production, 12 different colors of hydrogen are recognized today [5].

Standard colors of hydrogen

"Green" hydrogen is produced through water electrolysis, which requires electrical energy. When this energy is sourced from renewable energy sources, the hydrogen production process results in zero carbon dioxide emissions. For this reason, green hydrogen is also referred to as clean, low-carbon, or renewable hydrogen. It is well known that green hydrogen plays a vital role in the ongoing energy transition toward more sustainable energy sources. Currently, this type of hydrogen has a high production cost, but the fact that it results in zero carbon emissions still makes it the fuel of the future [9].

"Gray" hydrogen currently represents the majority of hydrogen production. It is most commonly produced through steam methane reforming (SMR), a process that also generates carbon dioxide, which is ultimately released into the atmosphere. Almost 40% of gray hydrogen is a byproduct of various chemical reactions. According

to the International Energy Agency (IEA), approximately 60% of the hydrogen produced is gray [1].

Globally, approximately 2% of coal and 6% of natural gas are used for the production of gray hydrogen, generating 830 million tons of carbon dioxide per year. However, carbon dioxide emissions from gray hydrogen are still lower than those from "black" and "brown" hydrogen production [10].

Black or brown hydrogen is produced from coal. Black hydrogen is derived from bituminous (black) coal, while brown hydrogen comes from lignite (brown) coal. Coal gasification is the method used for hydrogen production. This approach results in significant carbon dioxide emissions, approximately 20 kg of carbon dioxide per kg of hydrogen [5].

During the biomass gasification process, hydrogen is also produced, and some researchers argue that this hydrogen should also be considered "green." This is because biomass is a renewable resource, and its use can contribute to a more sustainable energy system.

"Blue" hydrogen is produced from fossil fuels, but unlike gray hydrogen, its production is associated with the capture and storage of greenhouse gases in underground storage sites. It is sometimes referred to as "carbon-neutral," but in practice, the amount of carbon dioxide captured is less than 100%.

Innovative hydrogen colors

"Turquoise" hydrogen can be produced through the thermal splitting of methane *via* pyrolysis. Compared to methane reforming (SMR - steam methane reforming), methane pyrolysis produces both hydrogen (H₂) and carbon (C) as a byproduct. The carbon produced can be easily stored and utilized. In this way, turquoise hydrogen demonstrates a reduced carbon footprint. Techniques such as plasma, thermal, and catalytic decomposition have been known for years but are still not well studied for industrial-scale hydrogen production.

A common issue with turquoise and blue hydrogen is the use of natural gas. Compared to blue hydrogen, the production of turquoise hydrogen is smaller. Additionally, during the production process of turquoise hydrogen, 3 kg of soot are produced for every 1 kg of hydrogen, which creates a need for a suitable market for the soot [11]. For this reason, compared to blue and green hydrogen, turquoise hydrogen has a smaller commercialization potential in the medium term.

"Pink," "red," and "purple" hydrogen can be compared in terms of production volume with green hydrogen, with one exception - nuclear energy which can be considered a carbon-neutral source instead of renewable electricity [12]. Nuclear energy can be considered a consistent and continuous source of electricity, which supports the production of pink hydrogen. This could lead to stable and flexible energy grids. However, there are challenges associated with the radioactive waste generated during this process.

"Golden" hydrogen is produced through biological processes that transform natural hydrocarbons obtained from deep oil wells. In this case, the richness of nature is combined with technological innovations. Golden hydrogen is a low-carbon hydrogen, but it is less cost-effective compared to green hydrogen in terms of production expenses. It also provides the opportunity for underground storage and utilization of the produced carbon dioxide, making it carbon-neutral.

"Yellow" hydrogen is produced through water electrolysis powered by a mix of electricity from various sources. For example, in 2021, Spain used 23.3% of wind and 21% of nuclear sources to generate yellow hydrogen through electrolysis powered by grid electricity. This was followed by 21% of energy generation from hydropower, 8% from photovoltaic systems, and 1% from water-to-electricity conversion [13]. In another example, Iceland uses 30% of its grid energy from geothermal sources, while 70% comes from hydro sources, leading to nearly zero carbon dioxide emissions.

"White" hydrogen is naturally occurring hydrogen. It is found naturally in geysers, hydrothermal systems, volcanic gases, layers of continental or oceanic crust, or as free gas. Degassing from the Earth's core, the reaction of water with rocks, radiolysis, and the breakdown of organic matter are the responsible processes for naturally occurring hydrogen. White hydrogen is an abundant, carbon-free resource that requires minimal infrastructure to be utilized, thus offering hydrogen energy without carbon emissions. However, there is a lack of sufficient research on white hydrogen.

To achieve the goal of NZE by 2050, green and pink hydrogen are considered key to long-term sustainability. All other forms of hydrogen also play a significant role in transitioning to a low-carbon future to achieve the ultimate goal.

Figure 2 summarizes the color codes of hydrogen in the so-called hydrogen rainbow.

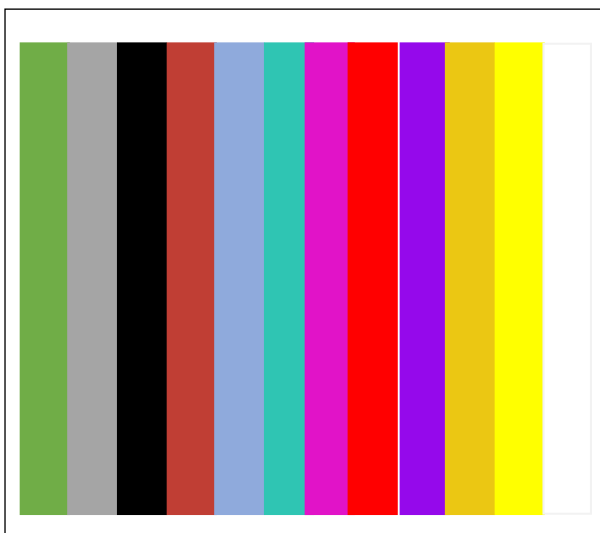


Figure 2. The hydrogen rainbow.

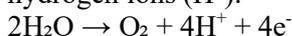
HYDROGEN PRODUCTION THROUGH ELECTROLYSIS

The production of hydrogen through electrolysis involves the following key stages:

1. *Water treatment:* The water is purified and deionized to obtain a clean electrolyte. This ensures that impurities do not interfere with the electrolysis process and helps to improve the efficiency and lifespan of the electrolyzer.

2. *Electrolysis process:* An electric current is passed through the aqueous solution in the electrolyzer. Typically, two electrodes – an anode and a cathode – are immersed in the electrolyte. When the electric current is applied, water molecules break down into hydrogen and oxygen. The reactions occur as follows:

- *At the anode (positive electrode):* Water molecules (H_2O) lose electrons and are oxidized to produce oxygen gas (O_2) and hydrogen ions (H^+):



- *At the cathode (negative electrode):* Hydrogen ions (H^+) gain electrons and are reduced to form hydrogen gas (H_2):



Thus, oxygen is released at the anode, and hydrogen gas is generated at the cathode. These reactions occur simultaneously, resulting in the production of hydrogen and oxygen gases.

3. *Collection of gases:* The produced hydrogen and oxygen gases are collected separately. They can either be used directly for various applications or stored for later use.

- *Hydrogen:* Typically, hydrogen gas is stored under pressure or in liquid form for transportation and storage. It can be used in

industries, energy production, or as fuel in hydrogen-powered vehicles.

- *Oxygen:* Oxygen can be vented into the atmosphere or captured for industrial applications, such as in medical or metallurgical processes.

Electrolysis can be classified into several categories.

According to the type of electrolyte:

1. *Alkaline electrolysis:* Uses an aqueous solution of alkali (usually potassium hydroxide or sodium hydroxide) as the electrolyte. This technology is one of the oldest and most widely used for industrial hydrogen production. Alkaline electrolysis has high efficiency and long component life.

2. *Proton exchange membrane (PEM) electrolysis:* Uses a polymer membrane that conducts protons (hydrogen ions) but not electrons. PEM electrolysis operates at lower temperatures and pressures compared to alkaline electrolysis, making it suitable for small and medium-sized installations. It also offers fast start-up and shut-down, which is beneficial for integration with renewable energy sources.

3. *Solid oxide electrolysis (SOE):* Uses solid oxide ceramic materials as electrolytes. SOE electrolysis operates at very high temperatures (around 800-1000°C), which allows for high efficiency and the potential for cogeneration of heat and electricity. However, this technology is still in the development stage and is not as widely deployed.

According to the type of cell:

1. *Monopolar cell:* Consists of multiple parallel cells connected in series. Each unit has its own anode and cathode, which results in greater flexibility and reliability.

2. *Bipolar cell:* Uses a common bipolar plate between each pair of anode and cathode. This reduces the number of required connections and simplifies the arrangement of the cells, resulting in a more compact design.

According to the type of application:

1. *Industrial electrolysis:* Used for large-scale hydrogen production for industrial purposes, such as in the chemical industry, refineries, and other sectors.

2. *Stationary electrolysis:* Designed for fixed installations, often connected to renewable energy sources such as solar or wind power.

3. *Portable electrolysis:* Small and mobile devices that can produce hydrogen on-site.

According to some authors, hydrogen production through electrolysis amounts to about 2% per year [14].

The production of energy from hydrogen fuel cells is a highly efficient and environmentally friendly method for the direct conversion of the chemical potential of reactants into electrical energy. A hydrogen fuel cell typically consists of separated electrodes (anode and cathode) through a proton exchange membrane (PEM), also referred to as the electrolyte [15] (Figure 3).

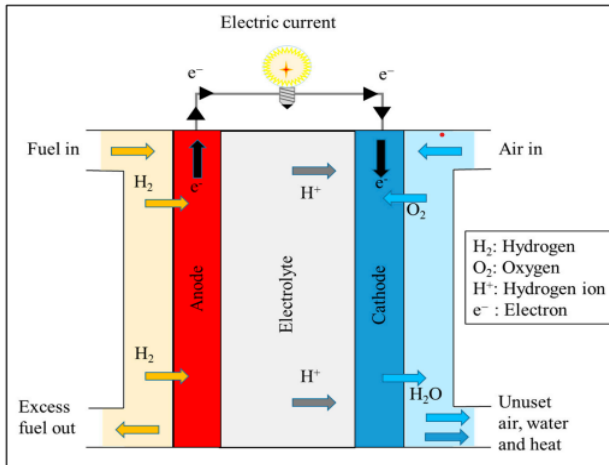


Figure 3. Hydrogen fuel cell [16].

The operating temperature is within the range of 333–353 K. Hydrogen and oxygen enter the fuel cell in the anode and cathode chambers, respectively. Hydrogen acts as an electron donor, while oxygen acts as an electron acceptor. At the anode, protons are formed, which pass through the membrane and react with oxygen at the cathode, resulting in the formation of water vapor and the release of heat.

Despite the numerous advantages of hydrogen energy, challenges still exist for the scientific community that must be addressed in order to achieve the sustainable application of hydrogen in the transportation sector. One possible solution is the development of hydrogen supply chains (HSC) that take into account the economic, environmental, and social aspects of sustainability.

SUPERSTRUCTURE OF A HYDROGEN SUPPLY CHAIN OBTAINED THROUGH ELECTROLYSIS PROCESS

Figure 4 presents a generalized superstructure of the hydrogen supply chain obtained through the electrolysis process. It includes feedstocks, production, storage, end usage, also transport. This structure allows for the identification of key decision points and optimization opportunities across the entire supply chain.

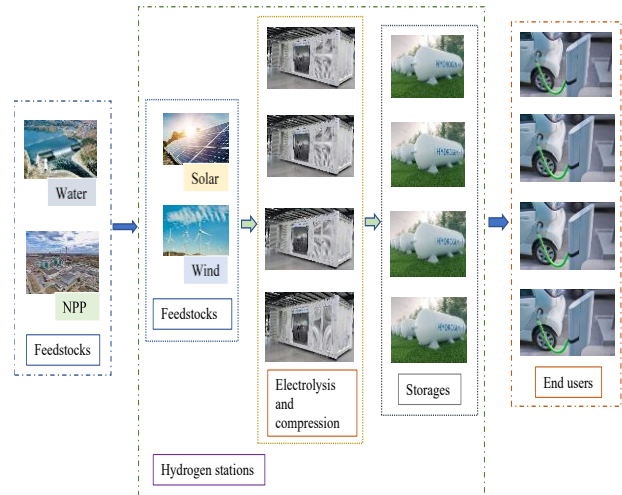


Figure 4. Generalized superstructure of a HSC for the supply of hydrogen produced through the electrolysis process.

AN OPTIMIZATION MODEL FOR DESIGNING A SUSTAINABLE HYDROGEN SUPPLY CHAIN THROUGH ELECTROLYSIS PROCESS

To formulate the mathematical model for the optimal design of a sustainable hydrogen supply chain (HSC), the following data are required:

Necessary data

1. Hydrogen Demand Data:

- Hydrogen demand: the required hydrogen demand (kg H₂) over a specific period, considering the energy needs of industries, transportation, and other sectors.
- Time horizon: The time period over which the hydrogen supply chain is evaluated (e.g., annually, monthly).

2. Hydrogen Production Data:

- Efficiency of electrolysis technologies: Energy efficiency for different electrolyzer types (alkaline, PEM, SOE).
- Electrolyzer capacity: The capacity of each type of electrolyzer (kg H₂/day or year).
- Energy consumption: Energy required for hydrogen production (kWh per kg H₂).
- Renewable energy source availability: The availability of renewable energy sources (solar, wind, hydro) for powering the electrolysis process (kWh/year).

3. Costs Data:

- Capital costs: Initial investment required for hydrogen production, storage, and transportation infrastructure.
- Operating costs: Ongoing costs for maintenance, electricity, labor, and other operational expenses.

- Transportation costs: Costs associated with hydrogen transportation (trucks, etc.).
 - Storage costs: Costs related to hydrogen storage systems (e.g., compression, liquefaction, etc.).
 - Carbon taxes/credits: Cost of CO₂ emissions or potential credits earned through the use of low-carbon technologies.
 - Energy costs: Cost of renewable energy required for electrolysis and cost of hydrogen produced in a nuclear power plant.
4. Environmental Data:
- Carbon emission factors: Emission levels per unit of hydrogen produced, considering the use of renewable and non-renewable energy sources.
 - Energy efficiency and emissions per transportation mode: Emission factors for hydrogen transport via different methods (trucks, etc.).
 - Emissions from storage: Any emissions resulting from storage processes (e.g., leakage, energy consumption).
5. Infrastructure Data:
- Storage capacity: Maximum storage capacity for hydrogen in different storage technologies (kg H₂).
 - Transportation capacity: Maximum hydrogen transportation capacity for the trucks, and other methods of transportation (kg H₂/day).
6. Social and Economic Data:
- Labor costs: Employment and wage data for workforce required in hydrogen production, storage, and transportation sectors.
 - Job creation impact: Estimations on the number of jobs created within the hydrogen supply chain.
 - Economic benefits: Potential for local economic growth, considering the hydrogen value chain's impact on local communities.
7. Regulatory Data:
- Government policies: Regulations, subsidies, or incentives for hydrogen production, transportation, and use, especially for renewable hydrogen.
 - Carbon emission reduction targets: National or regional carbon reduction targets and guidelines for hydrogen production.
8. Technical Constraints:
- Capacity limits for different production, storage, and transportation facilities.
 - Technological advancements: Expected improvements in technology efficiency, storage, or transportation costs.

Goal of optimization

The goal of solving the optimization problem is to be determined the optimal operating conditions, as follows:

1. Structure of the Hydrogen Supply Chain (HSC);
2. Production capacity for hydrogen from electrolysis systems, considering the available renewable energy sources and technological efficiency, to meet the hydrogen demand;
3. Number, location, and capacity of the charging stations that need to be built;
4. Performance of the charging stations;
5. Number, location, and capacity of the hydrogen storage facilities that need to be built;
6. Design of the hydrogen transportation network (trucks, etc.), including the capacity, route selection, and distribution methods;
7. Number of jobs created as a result of the operation of all HSC elements during its operating.
8. Energy source allocation. It is related to the distribution of renewable energy sources (e.g., wind, solar, hydropower) to the electrolysis systems for hydrogen production, maximizing energy utilization and minimizing operational costs.
9. Operational schedules for hydrogen production, storage, and transportation, ensuring system flexibility to handle varying demand patterns, renewable energy availability, and operational downtime.

The solution to this optimization problem provides a comprehensive design that ensures the most efficient, cost-effective, and environmentally friendly hydrogen supply chain while meeting all demand, regulatory, and social considerations.

MATHEMATICAL MODEL

The HSC is considered with a long planning horizon H (10 years). The entire time horizon H is divided into a set of discrete time intervals t . This time interval is divided into several equal subintervals, each with a duration of ∇t .

Over the planning horizon, it is assumed that the hydrogen consumption will change with a forecasted value. The mathematical model describing the optimal configuration of the sustainable hydrogen supply chain (HSC) is given as follows:

$$\text{Model of the environmental impact of HSC e TEI}_t, \\ \text{[kgCO}_2\text{eq /d]}$$

This model takes into account various factors influencing the environment throughout the entire hydrogen supply chain (HSC), including hydrogen production, storage, transportation, and distribution. The goal is to minimize the environmental footprint

of the HSC while ensuring that energy production aligns with sustainability goals and regulatory standards.

These emissions are equal to the sum of the impact of each stage of the life cycle on the environment. Greenhouse gas emissions are typically determined as follows for each time interval $t \in T$ [16]:

$$eTEI_t = eELD_t + eETT_t + eEAPP_t + eEPP_t, \forall t \quad (1)$$

where:

$eTEI_t$ - The total environmental impact of the HSC operation over its entire life cycle, [kgCO₂eq /y];

$eELD_t$ - Total greenhouse gas emissions from the production of diesel fuel, associated with diesel, [kgCO₂eq /y];

$eETT_t$ - Greenhouse gas emissions associated with the transportation of raw materials and product, [kgCO₂eq /y];

$eEAPP_t$ - Greenhouse gas emissions associated with the use of hydrogen as a fuel, [kgCO₂eq /y];

$eEPP_t$ - Greenhouse gas emissions released during hydrogen production through the electrolysis process, [kgCO₂eq /y].

Model of the economic impact of HSC $eTHC_t$, [\$/y]

Annual operating costs include the costs of raw material acquisition, local costs for the final product, production costs of the final products, and transportation costs for raw materials and final products. Production costs take into account both the fixed annual operating costs, which are given as a percentage of the corresponding total capital investment, as well as the net variable cost, which is proportional to the processing amount. Transportation costs account for both fixed distances and distances with variable costs. The economic optimization criterion will be the operating costs of the enterprise, which include the total investment costs for production facilities and the operation of the HSC. This cost is expressed through a dependency for each time interval $t \in T$:

$$eTHC_t = eTIC_t + eTPC_t + eTHH_t + eTHE_t + eTHHH_t + eTMO_t + eTPW_t + eTTC_t + eTTAXB_t + eTHSC_t + eTOEC_t - eT1L_t - eT2L_t - eTH_t, \forall t \quad (2)$$

where:

$eTHC_t$ - Total annual costs of the HSC, [\$/y];

$eTIC_T$ - Total investment costs for the production capacity of the HSC are related to the operational period of exploitation and the buyout of the installation per year, [\$/y]

$eTPC_t$ - Production costs in hydrogen production, [\$/y];

$eTHH_t$ - Costs for raw material purchase – water, [\$/y];

$eTHE_t$ - Costs for raw material purchase – electricity, [\$/y];

$eTHHH_t$ - Costs for hydrogen produced in a nuclear power plant, [\$/y];

$eTMO_t$ - Costs for maintenance and operation of the hydrogen fueling stations, [\$/y];

$eTPW_t$ - Production costs for waste disposal from hydrogen production, [\$/y];

$eTHSC_t$ - Total investment costs for the commercial capacity of the HSC relative to the operational period of operation and the acquisition of the hydrogen station per year, [\$/y];

$eTOEC_t$ - Operating costs for hydrogen retailers, [\$/y];

$eTTC_t$ - Total transportation costs of the HSC [\$/y];

$eTTAXB_t$ - Carbon tax levied according to the total amount of CO₂ generated during the operation of the HSC, [\$/y];

$eT1L_t$ - Government incentives for hydrogen consumption, [\$/y];

$eT2L_t$ - Government incentives for hydrogen production, [\$/y];

eTH_t - Revenue from the sale of produced hydrogen from all installed refueling stations, [\$/y].

Model of the social impact of HSC $eJob_t$, [Number of Jobs/y]

The social impact model for the operation of the HSC defines the expected total number of jobs created (J_t) as a result of the actions of all the elements of the system during its operation:

$$eJob_t = eNJ1_t + eLT_tNJ12_t + eNJ2_t + eLT_tNJ21_t, \forall t \quad (3)$$

where: the terms of (3) are defined according to the relationships for each time interval $t \in T$, [\$/y]:

$eNJ1_t$ - The costs for creating jobs related to the installation of hydrogen production facilities, [\$/y];

eLT_tNJ12_t - The costs for creating jobs related to the operation of the hydrogen facilities, [\$/y];

$eNJ2_t$ - The costs for creating jobs related to the installation of hydrogen refueling stations, [\$/y];

eLT_tNJ21_t - The costs for creating jobs related to the operation of hydrogen refueling stations, [\$/y].

Equation (3) can be considered as a simplified model of the social assessment criterion [17].

Model constraints

The constraints ensuring the feasibility of the obtained optimal solutions are as follows:

- Constraints regarding the capacity of the facilities, limited by the lower and upper boundaries;
- Constraints ensuring the flows admissibility;
- Constraints ensuring the hydrogen fuel needs of all regions;
- Constraints ensuring the necessary quantities of raw materials (water, electricity) for hydrogen production;
- Logistical and transportation constraints;
- Constraints ensuring the material balance for the entire HSC;
- Constraints ensuring the fulfillment of the annual capacities of the facilities;
- Constraints ensuring the satisfaction of product demand;
- Constraints ensuring the increase of social impact during the operation of the HSC as a whole.

Objective function

The optimal operating conditions for the HSC should ensure a minimum of the objective function, which includes:

1. *Environmental Impact Reduction*: The reduction of the overall carbon footprint of the hydrogen supply chain by optimizing the use of renewable energy sources, minimizing emissions from production, storage, and transportation processes.

2. *Cost Minimization*: The minimization of total costs across all stages of the hydrogen supply chain, including production, storage, transportation, and infrastructure development, while considering capital, operating, and maintenance costs.

3. *Social and Economic Objectives*: Maximizing the social and economic benefits of the hydrogen supply chain, such as job creation, economic growth, and local community impacts, while maintaining a balance between environmental sustainability and economic viability.

$$COST = \sum_{t \in T} (LT_t eTHC_t) \quad (4)$$

Find: X_t [Decision variables]

MINIMIZE { $COST(X_t)$ }

→ (Eq. 4) s. t. : {Constraints}

where: LT_t - duration of time intervals $t \in T$, [y].

The optimization problem can be solved using the GAMS application software, and it is possible to use it for making comprehensive intelligent decisions. After modifying the necessary data, the proposed plan can be adapted to different areas.

CONCLUSIONS

1. The color scale for classifying H_2 were generalized, which determines the method of its production. The color codes for H_2 are presented in the so-called hydrogen spectrum. The standard colors for hydrogen are: green, gray, brown, black, and blue, while the new/innovative ones are: turquoise, pink, red, purple, gold, yellow, and white. To achieve the goal of net zero emissions (NZE) by 2050, green and pink H_2 are considered essential for long-term sustainability.

2. The hydrogen production process through electrolysis has been considered. Energy generation from hydrogen fuel cells is a highly efficient and environmentally friendly method for directly converting the chemical potential of the reactants into electrical energy.

3. A generalized structure of the supply chain for hydrogen produced through electrolysis has been proposed. The HSC includes feedstocks, production, storage, end usage, also transport.

4. A model for designing the HSC was proposed, taking into account the three pillars of the sustainability concept: economic, environmental, and social.

5. The environmental criterion includes the impact on the environment during the operation of the considered hydrogen supply chain.

6. The economic criterion includes the operating costs of the enterprise, which consist of the total investment costs for production capacities and the operation of the HSC.

7. The social criterion includes the expected total number of jobs created as a result of the operation of all system elements during its functioning.

8. The developed model is formulated in terms of Mixed-Integer Linear Programming (MILP) and can be solved using specialized optimization software, such as GAMS.

Acknowledgement: This study was carried out with the financial support of Bulgarian Science Fund,

Ministry of Education and Science of the Republic of Bulgaria, Contract KII-06-H89/6/09.12.2024.

REFERENCES

1. IEA (International Energy Agency), Hydrogen, 2023. <https://www.iea.org/energy-system/low-emission-fuels/>
2. O. Schmidt, A. Gambhir, I. Staffell, A. Hawkes, J. Nelson, S. Few, *International Journal of Hydrogen Energy*, **42(52)**, 30470 (2017).
3. D.L. Greene, J.M. Ogden, Z. Lin, *eTransportation*, **6**, 100086 (2020).
4. G.F. Naterer, I. Dincer, C. Zamfirescu, Hydrogen Production from Nuclear Energy, Springer, 2013.
5. S. Tasleem, E. H. Alsharaeh, *Energy Conversion and Management*, **326**, 119500 (2025).
6. SCOPUS, <https://www.scopus.com/>
7. J.A. Riera, R.M. Lima, O.M. Knio, *International Journal of Hydrogen Energy*, **48(37)**, 13731 (2023).
8. W. Shen, H. Li, H. Ding, M. Zeng, C. Xie, X. Zhang, *Energy Science & Engineering*, **13(3)**, 1306 (2025).
9. J.M.M. Arcos, D.M. Santos, *Gases*, **3(1)**, 25 (2023).
10. M. Newborough, G. Cooley, *Fuel Cells Bulletin*, **11**, 16 (2020).
11. Ch. Idrissov, IDTechEx logo, (2023). <https://www.idtechex.com/en/research-article/methane-pyrolysis-unlockingthe-potential-of-turquoise-hydrogen/29395>
12. R. Pinsky, P. Sabharwall, J. Hartvigsen, J. O'Brien, *Progress in Nuclear Energy*, **123**, 103317 (2020).
13. L. Fernandez, Statista, 2023. <https://www.statista.com/statistics/1007877/share-of-electricitygeneration-in-spain/>
14. T. Terlouw, C. Bauer, R. McKenna, M. Mazzotti, *Energy & Environmental Science*, **15(9)**, 3583 (2022).
15. V. Beschkov, E. Ganev, *Energies*, **16(17)**, 6108 (2023).
16. E. Ganev and V. Beschkov, *Bulgarian Chemical Communications*, **54(3)**, 205 (2022).
17. E. Ganev, B. Ivanov, N. Vaklieva-Bancheva, E. Kirilova, Y. Dzhelil, *Energies*, **14(8)**, 2261 (2021).

Optimization approach for the design of a sustainable hydrogen supply chain through steam methane reforming

E. Ganev^{1*}, V. Beschkov¹, E. Kirilova¹, D. Nikolova², R. Vladova¹, M. Dimova-Gabrovska³

¹*Institute of Chemical Engineering, Bulgarian Academy of Sciences, Acad. G. Bontchev, Str., Bl. 103, 1113 Sofia, Bulgaria*

²*Burgas State University "Prof. Dr. Asen Zlatarov", Prof. Yakim Yakimov Blvd. 1, 8010, Burgas, Bulgaria*

³*Department of Prosthetic Dental Medicine, Faculty of Dental Medicine, Medical University – Sofia, 1 Sv. Georgi Sofiyski Str., Sofia 1431, Bulgaria*

Received: April 29, 2025; Revised: June 02, 2025

Hydrogen is emerging as a key energy carrier in the global transition to more sustainable energy systems. There are various technologies for its production, each with its own advantages and disadvantages in terms of efficiency, costs, and environmental impact. More than 97% of the hydrogen produced globally is mainly obtained through steam methane reforming (SMR) of natural gas, which is the most widely used and cheapest method of production. Although the conventional SMR process is energy-intensive and results in significant carbon dioxide emissions, there are opportunities to enhance its sustainability by integrating Carbon Capture, Utilization, and Storage (CCUS) technologies. However, a crucial factor for its large-scale deployment is the development of an efficient and sustainable hydrogen supply chain (HSC) design, where all processes along the chain are optimized while simultaneously satisfying environmental, economic, and social criteria. The present study proposes an optimization model for designing a HSC, focusing on the development of hydrogen refueling stations simultaneously considering all aspects of sustainability. It is formulated in terms of Mixed-Integer Linear Programming (MILP) and includes the necessary parameters, decision variables, and environmental, economic, and social performance of the HSC, along with an objective function and constraints. The model is designed to be proved on a real case study on the territory of the Republic of Bulgaria with its 27 administrative regions.

Keywords: hydrogen production; steam methane reforming; supply chain design; multi-objective optimization; economic, environmental and social criteria

INTRODUCTION

Hydrogen is emerging as a key energy carrier in the global transition to more sustainable energy systems [1]. It offers the potential for decarbonizing various sectors, including transportation, industry, and electricity generation, especially when produced from renewable sources [2].

In the context of growing concerns about climate change and the need to reduce greenhouse gas emissions, sustainable hydrogen production is becoming increasingly important [3].

Global hydrogen consumption is growing rapidly, reaching 95 Mt in 2022, and is expected to reach 180 Mt by 2030. The greenhouse gas emissions generated from the production of 95 Mt of hydrogen in 2022 are over 1,291 Mt CO₂-eq [4].

There are various hydrogen production technologies, each with its own advantages and disadvantages in terms of efficiency, costs, and environmental impact [2]. Today, roughly 95% of all

hydrogen is produced from fossil fuels through the steam methane reforming (SMR) of natural gas [4].

Regardless of the production method used, an efficient and sustainable hydrogen supply chain design is crucial for its large-scale deployment [2]. A well-optimized supply chain should encompass all transportation, and distribution, while considering stages of hydrogen production, storage, all aspects of sustainability, including economic, environmental, and social factors.

The lack of developed infrastructure is often identified as a major barrier to the development of the hydrogen economy. In this context, the optimal design of a sustainable supply chain for hydrogen production via SMR represents an important research challenge.

The aim of this study is to develop a framework for modeling and optimizing a sustainable hydrogen supply chain (HSC) that enables informed decision-making regarding its structure and operation.

By including various storage and transportation options, this study aims to propose an optimization

* To whom all correspondence should be sent:
E-mail: evgeniy_ganev@abv.bg

approach that ensures environmentally and economically efficient hydrogen production and delivery from methane, while achieving social satisfaction for the participants in the supply chain.

The proposed approach will contribute to overcoming the existing challenges and supporting the realization of hydrogen's full potential as a clean energy carrier.

LITERATURE REVIEW

In recent years, the concept of using hydrogen as a potential clean energy carrier has gained significant interest due to the need to achieve energy sustainability and flexibility in production systems [5]. In addition to its role in decarbonizing the transportation and residential sectors, hydrogen enables the efficient production of so-called e-fuels (electrofuels), such as ammonia, methanol, and synthesis gas, when combined with CCUS technology and renewable sources [6].

However, despite the efforts of numerous researchers in developing methods for hydrogen production from renewable sources, the production of "green" hydrogen remains significantly more expensive compared to technologies that use fossil fuels [7].

Among the various production methods, the production of so-called "grey" hydrogen from natural gas through SMR is the most widespread and well-established technology for hydrogen extraction. Global natural gas consumption for this purpose accounts for 6% [8].

The successful implementation of this technology also faces several challenges, with the biggest being the lack of suitable infrastructure.

One way to achieve high efficiency and sustainability in this type of production, as well as to address the aforementioned issues arising during their implementation, is the application of an approach for the optimal design of the hydrogen supply chain, while simultaneously considering environmental, economic, social, and other aspects. The optimal hydrogen supply chain must consider the number, location, and capacity of both production facilities and storage capacities, as well as transportation methods. Additionally, demand, temporal, and spatial factors should be taken into account from the early stages of HSC design.

Mathematical programming is a broadly used approach for optimal design and exploitation of hydrogen supply chains.

A large number of studies propose single-objective and multi-objective optimization models for the design and operation of regional HSC under

deterministic and stochastic conditions, formulated in terms of MILP programming.

Erdoğan & Güler [9] propose a multi-objective optimization approach to simultaneously minimize costs, carbon emissions, and risk in the operation of an HSC for hydrogen production through SMR, combined with water electrolysis. Li *et al.* [3] develop a multi-period MILP model for designing a regional HSC, which takes into account the availability of primary energy sources (e.g., natural gas, coal, biomass, and renewable energy), production technologies, transportation methods, and types of storage.

Although economic and environmental factors are the most common objectives in the design and planning of HSC infrastructure, recent studies increasingly consider factors related to risk assessment in the operation of HSCs. Robles *et al.* [10] propose a stochastic, spatially-based, multi-objective, multi-period MILP model to minimize daily costs, global warming potential, and risk when determining the optimal number, type, capacity, and location of production and storage facilities, as well as transportation units, in addition to the hydrogen flow between different locations.

On the other hand, social responsibility is one of the key factors for assessing the willingness of end-users to switch to hydrogen fuel cell vehicles.

An example of such a study is the one by Fazli-Khalaf *et al.* [11], who, in developing their HSC models, include reliability and social responsibility alongside environmental and economic criteria.

Their study focuses on people and their quality of life, taking into account social responsibility, such as job creation and timely satisfaction of customer needs. The authors develop a fuzzy probabilistic flexible programming model to enhance the flexibility of the hydrogen network under mixed uncertainties and to maximize the reliability and sustainability of the hydrogen supply chain in Iran.

Based on the literature review of recent years on approaches for the optimal design of hydrogen supply chains produced through steam methane reforming, it can be concluded that the majority of studies are dedicated to the design and planning of internal hydrogen supply chain networks for the transportation sector. The developed models are either deterministic or stochastic and are defined in terms of MILP. Approaches that consider only the economic performance of the examined HSC are widespread. Another, smaller group of approaches, alongside economic aspects, simultaneously considers environmental factors related to the assessment of greenhouse gas emissions released into the atmosphere as a result of hydrogen

production via SMR, as well as the transportation of raw materials and products. Some authors have also included additional optimization criteria in their studies, related to the assessment of the risk of the technologies used, achieving the highest quality of the produced product, and others. There are few optimization approaches in the available literature for designing a sustainable HSC through the application of steam methane reforming (SMR) that, alongside economic and environmental aspects, also consider social factors.

This gives us the basis to propose a multi-objective optimization framework for designing a sustainable hydrogen supply chain that simultaneously considers the economic, environmental, and social performance models of the chain, with a focus on building infrastructure for hydrogen fuel stations.

HYDROGEN PRODUCTION THROUGH STEAM REFORMING OF METHANE

Steam methane reforming (SMR), commonly known as steam reforming, is a standard industrial method for producing hydrogen. More than 97% of the hydrogen produced globally is primarily obtained through SMR [12]. SMR is mainly applied in the chemical and oil industries, and currently, it is the most widespread and cost-effective method for hydrogen production.

The production of hydrogen through SMR undergoes the following main stages: (a) synthesis gas production, (b) conversion of carbon monoxide to hydrogen (water-gas shift reaction), and (c) purification [13] (Figure 1).

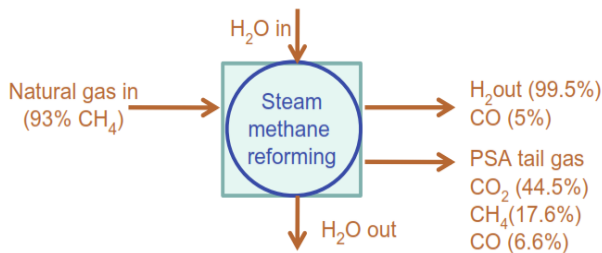
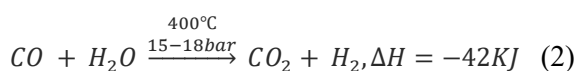
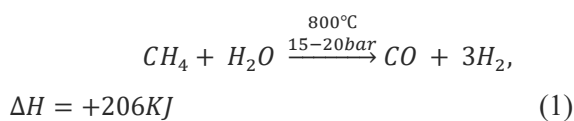
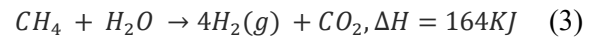


Figure 1. Block diagram of the steam methane reforming process [14]. In the first stage of the process, a catalytic endothermic reaction (Eq. 1) takes place between methane (natural gas) and steam at a high temperature (the steam methane reforming process). As a result of this reaction, synthesis gas is produced, which contains 85% of carbon monoxide, hydrogen, and small amounts of residual methane and carbon dioxide and water [15].



The steam methane reforming process is conducted at temperatures ranging from 700 to 1000°C and pressures of 15-20 bar in the presence of steam, during which hydrocarbons are converted [16]. After the exothermic water-gas shift reaction (Eq. 2), carbon monoxide is converted into carbon dioxide and hydrogen. The process takes place at a temperature of 400°C and a pressure of 15-18 bar.

The governing reaction of the steam methane reforming process is as follows:



In the purification stage, the pressure swing adsorption process is the predominant method [12], where the reactive gas mixture containing methane and hot steam is fed into the catalytic reactor. Since the reaction is endothermic, the combustion of methane with air in the reactor's furnace provides the required reaction heat. The energy efficiency of these processes is 64% [17].

OPTIMIZATION APPROACH FOR DESIGNING A SUSTAINABLE SUPPLY CHAIN FOR HYDROGEN PRODUCTION OBTAINED THROUGH THE STEAM METHANE REFORMING PROCESS

General formulation of the optimization problem

Steam reforming is typically applied to natural gas, but it can also be successfully adapted for processing other hydrocarbons such as propane, gasoline, or ethanol, providing flexibility in raw material selection.

The availability and economic viability of natural gas determine the competitiveness of steam reforming for hydrogen production. The hydrogen produced by this method is available at an affordable price of 1,2-1,5\$/kg-H₂.

It is evident, however, that carbon dioxide is an inevitable by-product. The primary pollution with carbon dioxide comes from the energy used to heat the reaction mixtures, which amounts to approximately 10 kg CO₂ of kg H₂. This contributes to generation of greenhouse gas emissions, making the method less environmentally friendly. Carbon dioxide is a valuable raw material for a number of industries, but the process of its utilization increases the cost of H₂ to 1,5–1,8\$/kg-H₂ [18].

Before hydrogen fuel can be successfully introduced to the market, however, there are several challenges to overcome, such as the high production cost and the lack of a developed infrastructure for hydrogen fuel transportation [19]. One way to overcome these challenges is by applying an

approach for the optimal design of sustainable HSCs. Key aspects in designing such chains include the simultaneous consideration of the three aspects of sustainability – environmental, economic, and social (Figure 2) [20].

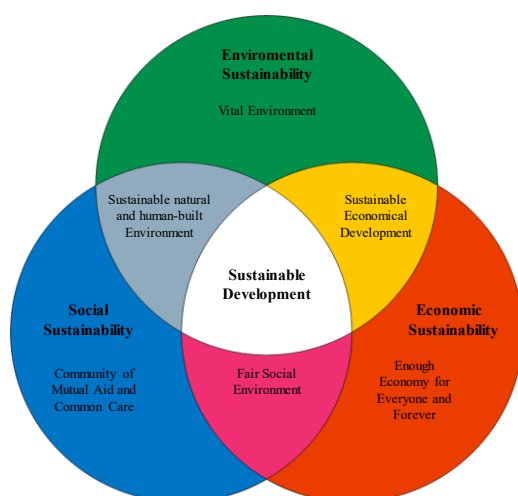


Figure 2. Concept of sustainable HSC management for hydrogen production and distribution [20].

This research aims to propose an optimization framework for designing a sustainable HSC, taking into account the three aspects of sustainability, with a focus on the construction of fueling stations. This issue is relevant as many countries are preparing to introduce hydrogen fuel for transportation purposes, as well as planning and building the necessary infrastructure for this. Initially, we consider the existing enterprises, such as chemical plants and fertilizer factories involved in hydrogen production from natural gas, as producers. The idea is that once the infrastructure for hydrogen fueling stations is built and hydrogen fuel end-users are formed, investors will then engage in the construction of facilities for producing carbon-neutral hydrogen.

Superstructure of sustainable HSC through SMR process

For the purposes of our study, we consider a superstructure of an HSC produced through SMR, which includes the following key elements:

1. *Hydrogen production in chemical plants and fertilizer factories.* The following processes are included:

- Steam methane reforming (SMR). This is the main process where methane reacts with steam at high temperatures (700–1000°C) using a nickel catalyst to produce synthesis gas (H₂, CO, CO₂).

- Carbon monoxide conversion (Water-Gas Shift) – an additional reaction to increase hydrogen yield by converting CO with steam into CO₂ and H₂.
- Hydrogen purification – through Pressure Swing Adsorption or membrane technologies for separating pure hydrogen.

2. Hydrogen storage and transport

- Short-term storage – using compressed hydrogen tanks.
- Distribution – transportation via cryogenic tankers.
- Local distribution stations – hydrogen refueling stations for industrial, transportation, and residential needs.

3. Consumption and applications

- Transport sector – hydrogen fuel cells for vehicles.

Figure 3 illustrates the superstructure of the considered HSC.

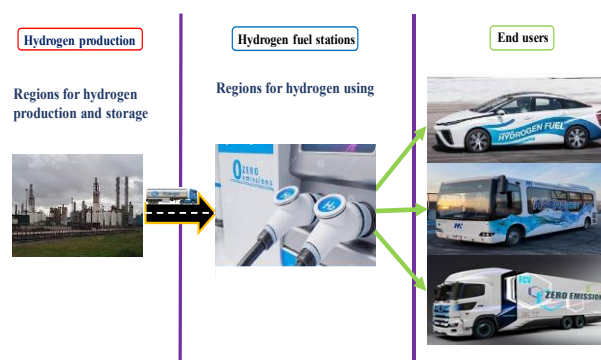


Figure 3. Superstructure of the HSC for hydrogen production *via* steam methane reforming with a focus on building hydrogen refueling stations.

Optimization framework of the approach

Optimal design of the HSC through SMR requires the definition of a multi-objective mathematical model that takes into account economic, environmental, and social factors. This model includes the following components:

Necessary data

To create the optimal model for designing a sustainable HSC through SMR, the following data is required:

1. *Economic Data:* Cost of Natural Gas; Cost of Water; Capital cost of SMR plants; Operational cost of SMR plants; Hydrogen storage cost; Transportation cost *via* trucks.
2. *Technical Data:* SMR facilities efficiency; Hydrogen yield per unit of methane; Production capacity of the SMR facilities; Hydrogen storage facilities; Transportation distance and mode.

3. *Environmental Data*: greenhouse gas emissions generated during hydrogen production; greenhouse gas emissions generated during hydrogen transportation; greenhouse gas emissions generated during hydrogen storage; Regulatory emission limits.

4. *Demand & Location Data*: Geographical locations of demand centers; Projected hydrogen demand over time; Availability of natural gas sources and infrastructure; Distance between production sites, storage, and hydrogen fuel stations.

5. *Social and Economic Data*: Labor costs related with employees hired in hydrogen production, storage, and transportation sites.

6. *Regulatory Data*: Government policies: Regulations, subsidies, or incentives for hydrogen production, transportation, and use.

Goal of optimization

The goal of solving the optimization problem is to determine the optimal operating conditions, as follows:

1. Structure of the Hydrogen Supply Chain.
2. Capacity for hydrogen produced through SMR process, considering the available renewable energy sources and technological efficiency, to meet the hydrogen demand.
3. Number, location, and capacity of the fueling stations that need to be built.
4. Performance of the fueling stations.
5. Number, location, and capacity of the hydrogen storage facilities that need to be built.
6. Design of the hydrogen transportation network (trucks, etc.), including the capacity, route selection, and distribution methods.
7. Number of jobs created as a result of the operation of all HSC elements.
9. Operational schedules for hydrogen production, storage, and transportation, ensuring system flexibility to handle varying demand patterns, renewable energy availability, and operational downtime.

The solution to this optimization problem provides a design that ensures not only the technical feasibility of the process but also its environmental, economic, and social sustainability, which is crucial for the future of the hydrogen economy.

Decision variables

For the purpose of defining the optimization model of the HSC, the following decision variables need to be introduced:

1. Continuous variable for the amount of hydrogen produced in the SMR facility.

2. Continuous variable for the amount of hydrogen transported from the SMR facility to the storage location.

3. Continuous variable for the amount of hydrogen transported from the storage location to the hydrogen fueling station.

4. Continuous variable for the amount of hydrogen stored in the respective facilities.

5. Continuous variable for the capacity of hydrogen production at SMR facilities.

6. Binary variable for establishing SMR facilities at a particular location.

7. Binary variable for selecting storage facilities.

8. Binary variable for transportation mode selection (truck).

9. The number of jobs that will be created for the building of facilities for production and operation of the hydrogen supply chain.

Mathematical model for the optimal design of a sustainable HSC through SMR process

The HSC is planned over a long-term horizon H of 10 years. This total period is segmented into a series of discrete time intervals t , each of which is further subdivided into multiple equal subintervals of duration ∇t .

Throughout the planning horizon, hydrogen consumption is expected to vary according to forecasted values. The optimal configuration of the sustainable HSC is mathematically represented as follows:

➤ Mathematical model of environmental performance of the HSC - $mTEI_t$, [kgCO₂eq /y]

The environmental criterion will include the environmental impact during the operation of the HSC through the greenhouse gas emissions generated at each time interval $t \in T$. These emissions are equal to the cumulative impact of each stage of the hydrogen production lifecycle through this process. Greenhouse gas emissions are typically determined as follows for each time interval $t \in T$:

$$mTEI_t = mELH_t + mEHS_t + mELD_t + mETT_t + mESW_t + mEAPP_t, \forall t \quad (4)$$

where:

$mTEI_t$ is the total environmental impact of the operation of the HSC over its entire lifecycle, [kgCO₂eq /y];

$mELH_t$ are the total greenhouse gas emissions from the hydrogen production process through SMR, [kgCO₂eq /y];

$mEHS_t$ are the total greenhouse gas emissions associated with the compression and storage of the produced hydrogen, [kgCO₂eq /y];

$mELD_t$ are the total greenhouse gas emissions from the production of diesel fuel associated with the transportation of hydrogen to the fuel stations, [kgCO₂eq /y];

$mETT_t$ is the environmental impact associated with the transportation of hydrogen to the fuel stations, [kgCO₂eq /y];

$mESW_t$ are the greenhouse gas emissions released during the utilization of waste (CO₂ as a by-product and components of natural gas such as N₂, H₂S, etc.), generated from hydrogen production for each time interval $t \in T$, [kgCO₂eq /y];

$mEAPP_t$ are the greenhouse gas emissions from the use of hydrogen as a fuel [kgCO₂eq /y].

➤ *Mathematical model of the economic performance of HSC - $mTHC_t$ [\$/y]*

The annual operating costs of hydrogen production through SMR include: capital costs for the construction of hydrogen production facilities through methane steam reforming; costs for purchasing the necessary raw materials for this production—water and electricity; production costs; costs for waste disposal from hydrogen production; costs for compressing and storing the produced hydrogen; transportation costs for raw materials and final products; maintenance costs for the built facilities; government incentives, etc.

The production costs take into account both the fixed annual operating costs, which are given as a percentage of the corresponding total capital investment, as well as the net variable cost, which is proportional to the processing amount.

The economic criterion represents the operating costs of the enterprise, which include the total investment costs for production facilities and the functioning of the HSC.

This price is expressed through the dependency for each time interval $t \in T$:

$$mTHC_t = mTIC_t + mTPC_t + mTPW_t + mTHH_t + mTHE_t + mTHS_t + mTMO_t + mTTC_t + mTTAXB_t + mTHSC_t + mTOEC_t - mT1L_t - mTA_t - mTH_t, \forall t \quad (5)$$

where:

$mTHC_t$ are the total annual costs of the HSC, [\$/y];

$mTIC_t$ are the total investment costs for the production capacity of the HSC relative to the period of operation and the buyout of the installation per year, [\$/y];

$mTPC_t$ are the costs associated with hydrogen production, [\$/y];

$mTPW_t$ are the costs for waste disposal from hydrogen production (CO₂ as a by-product and components of natural gas such as N₂, H₂S, etc.), [\$/y];

$mTHH_t$ are costs for raw material purchase – water, [\$/y];

$mTHE_t$ are costs for raw material purchase – electricity, [\$/y];

$mTHS_t$ are costs associated with compressing and storing the produced hydrogen, [\$/y];

$mTMO_t$ are costs for maintenance and operation of the hydrogen fueling stations, [\$/y];

$mTTC_t$ are the total transportation costs of HSC, [\$/y];

$mTTAXB_t$ is the carbon tax, levied based on the total amount of CO₂ generated during the operation of HSC, [\$/y];

$mTHSC_t$ are the total investment costs for the commercial capacity of the HSC relative to the period of operation and the purchase of the hydrogen station, [\$/y];

$mTOEC_t$ are the operational costs for the end hydrogen retailers, [\$/y];

$mT1L_t$ are government incentives for hydrogen consumption, [\$/y];

mTA_t is the total value of by-products (CO₂) [\$/y];

mTH_t is the revenue from the sale of produced hydrogen from all installed refueling stations, [\$/y];

➤ *Mathematical model of social performance of the HSC - $mJobs_t$ [\$/y]*

The model for the social assessment of the operation of the HSC determines the expected total number of jobs created as a result of the actions of all system components during its operation:

$$mJobs_t = mNJ1_t + mLT_t NJ12_t + mNJ2_t + mLT_t NJ21_t, \forall t \quad (6)$$

where:

the terms of equation (6) are determined according to the relationships at each time interval $t \in T$, [\$/y]:

$mNJ1_t$ are the costs for creating jobs related to the installation of hydrogen production facilities, [\$/y];

$mLT_t NJ12_t$ are the costs for creating jobs related to the operation of hydrogen production facilities, [\$/y];

$mNJ2_t$ are the costs for creating jobs related to the installation of hydrogen refueling stations, [\$/y];

mLT_tNJ21_t are the costs for creating jobs related to the operation of hydrogen refueling stations, [\$/ y].

Constraints

For the design of HSC and the creation of a model using MILP, certain constraints need to be considered. These constraints vary in nature. They are the following:

- Production constraints related to the hydrogen produced through steam methane reforming; potential production from renewable energy sources; demand in different sectors such as industry, transportation, and residential needs; losses during compression and transportation.
- Constraints regarding the maximum capacity of steam methane reforming as well as the capacity of storage facilities.
- Environmental constraints regarding the allowable levels of carbon dioxide emissions according to adopted regulatory requirements.
- Transportation constraints regarding the total transport capacity, capacity of the transport mode, and the number of transport units.
- Budgetary constraints regarding the total investment and operational costs of the HSC.
- Constraints regarding the achievement of demand satisfaction and others.

Objective function

To solve the optimization problem for the optimal design of HSC using SMR, an objective function has been defined, which includes the previously defined optimization criteria regarding the environmental, economic, and social performance of HSC (equations 4, 5, and 6). It aims simultaneously to:

1. *Minimizing the environmental impact of the HSC:* The reduction of the environmental impact of the considered HSC can be achieved by minimizing: greenhouse gas emissions related to hydrogen production; its storage; the production of diesel fuel for the vehicles used for transportation; the transport of raw materials and products; the utilization of waste carbon dioxide; as well as the use of hydrogen as a fuel.

2. *Minimizing the economic impact of the HSC:* The minimization of total costs across all stages of HSC, including minimizing: the total investment costs for building facilities for hydrogen production through steam methane reforming; costs associated with hydrogen production; costs for disposing of waste from hydrogen production; costs for purchasing raw materials for hydrogen production (water, electricity); costs related to compressing and

storing the produced hydrogen; operational costs; the carbon tax imposed on the generated greenhouse gas emissions during the operation of the HSC.

3. *Achieving social satisfaction for those employed in all elements of the HSC:* Maximizing the social and economic benefits of the HSC can be achieved by optimizing the costs of creating jobs associated with: the building of hydrogen production facilities; the operation of hydrogen production facilities; the building of hydrogen refueling stations; the operation of hydrogen refueling stations.

The overall optimization criterion is formulated as follows:

$$COST = \sum_{t \in T} LT_t (mTEI_t + mTHC_t) \quad (7)$$

Find: X_t [Decision variables]

$$\begin{aligned} &MINIMIZE\{COST(X_t)\} \\ &\rightarrow (Eq. 7) s. t. : \{Constraints\} \end{aligned}$$

where:

LT_t are the durations of time intervals $t \in T$, [year].

The proposed model is formulated in terms of mixed-integer linear programming (MILP) and includes the necessary data, parameters, environmental, economic, and social models for the representation of the HSC, the objective function, and the constraints. The model is created with the aim of being further tested on a real-case study on the territory of Bulgaria with its 27 administrative regions. The optimization model will be defined and solved based on the environmental and economic optimization criteria, while the social criterion will be defined as a constraint using the commercial optimization software GAMS.

CONCLUSIONS

The study proposes a mathematical approach for the optimal design of a sustainable HSC, produced through steam methane reforming, with a focus on the construction of hydrogen fueling stations. The proposed model is defined in terms of mixed-integer linear programming (MILP) and includes the necessary parameters, decision variables, environmental, economic, and social models for the representation of the HSC, as well as the objective function and constraints. In the future, its application is planned on a real case study from Bulgaria to support investment decisions, reduce costs, and minimize the carbon footprint, which is crucial for the development of the hydrogen economy.

Acknowledgement: The study represents results obtained under project "Supply chains for the

sustainable production and distribution of hydrogen from various feedstocks” funded by the Bulgarian Science Fund under Contract № KII-06-H89/6/09.12.2024.

REFERENCES

1. L. Feng, PhD Thesis, University Bourgogne Franche-Comté, Besançon, France, 2024.
2. S. de León Almaraz, PhD Thesis, Université de Toulouse, Toulouse, France, 2014.
3. M. Li, P. Ming, R. Huo, H. Mu, C. Zhang, *Sustainable Cities and Society*, **92**, 104444 (2023).
4. Irena (International Renewable Energy Agency), 2023, Global hydrogen production CO₂ emissions and average emissions intensity in the Net Zero Scenario, 2019-2030. Charts – Data & Statistics <https://www.iea.org/data-and-statistics/charts/global-hydrogen-production-co2-emissions-and-average-emissions-intensity-in-the-net-zero-scenario-2019-2030-3>.
5. J.O. Abe, A.P.I. Popoola, E. Ajenifuja, O.M. Popoola, *International Journal of Hydrogen Energy*, **44(29)**, 15072 (2019).
6. F. Razi and I. Dincer, *Renewable and Sustainable Energy Reviews*, **168**, 112763 (2022).
7. G. Durakovic, P. C. del Granado, A. Tomasgard, *Energy*, **282**, 128282. (2023).
8. IEA (International Energy Agency). Putting CO₂ to Use; IEA: Paris, France, 2019. https://iea.blob.core.windows.net/assets/50652405-26db-4c41-82dc-c23657893059/Putting_CO2_to_Use.pdf
9. A. Erdoğan, M.G. Güler, *International Journal of Hydrogen Energy*, **48**, 22752 (2023).
10. J.O. Robles, C. Azzaro-Pantel, A. Aguilar-Lasserre, *Computers & Chemical Engineering*, **140**, 106853 (2020).
11. M. Fazli-Khalaf, B. Naderi, M. Mohammadi, M.S. Pishvae, *International Journal of Hydrogen Energy*, **45(59)**, 34503 (2020).
12. C. Koroneos, A. Dompros, G. Roumbas, & N. Moussiopoulos, *International Journal of Hydrogen Energy*, **29(14)**, 1443 (2004).
13. N. Hajjaji, PhD Thesis, Institut National Polytechnique de Lorraine, France, 2011.
14. S.D.L. Almaraz and C. Azzaro-Pantel (eds.), in: Hydrogen economy Academic Press, 2017, p. 85.
15. J.R. Bartels, M.B. Pate, N.K. Olson, *International Journal of Hydrogen Energy*, **35(16)**, 8371 (2010).
16. G. Landucci, A. Tugnoli, C. Nicoletta, V. Cozzani, in: 5th International Seminar on Fire and Explosion Hazards, Edinburgh, UK, 2007, p. 23.
17. V. Beschkov, E. Ganev, *Energies*, **16(17)**, 6108 (2023).
18. E. Sun, S. Zhai, D. Kim, M. Gigantino, V. Haribal, O.S. Dewey, S. Williams, G. Wan, A. Nelson, S. Marin-Quiros, J. Martis, Ch. Zhou, J. Oh, R. Randall, M. Kessler, D. Kong, J. Rojas, A. Tong, X. Xu, C. Huff, M. Pasquali, R. Gupta, M. Cargnello, A. Majumdar, *Cell Reports Physical Science*, **4(4)**, 101338 (2023).
19. J. Kurtz, S. Sprik, T. H. Bradley, *International Journal of Hydrogen Energy*, **44(23)**, 12010 (2019).
20. E. Ganev, V. Beschkov, *Bulgarian Chemical Communications*, **54(3)**, 205 (2022).

Instructions about Preparation of Manuscripts

General remarks: Manuscripts are submitted in English by e-mail. The text must be prepared in A4 format sheets using Times New Roman font size 11, normal character spacing. The manuscript should not exceed 15 pages (about 3500 words), including photographs, tables, drawings, formulae, etc. Authors are requested to use margins of 2 cm on all sides.

Manuscripts should be subdivided into labelled sections, e.g. INTRODUCTION, EXPERIMENTAL, RESULTS AND DISCUSSION, etc. **The title page** comprises headline, author(s)' names and affiliations, abstract and key words. Attention is drawn to the following:

a) **The title** of the manuscript should reflect concisely the purpose and findings of the work. Abbreviations, symbols, chemical formulae, references and footnotes should be avoided. If indispensable, abbreviations and formulae should be given in parentheses immediately after the respective full form.

b) **The author(s)**' first and middle name initials and family name in full should be given, followed by the address (or addresses) of the contributing laboratory (laboratories). **The affiliation** of the author(s) should be listed in detail (no abbreviations!). The author to whom correspondence and/or inquiries should be sent should be indicated by an asterisk (*) with e-mail address.

The abstract should be self-explanatory and intelligible without any references to the text and containing up to 250 words. It should be followed by keywords (up to six).

References should be numbered sequentially in the order, in which they are cited in the text. The numbers in the text should be enclosed in brackets [2], [5, 6], [9–12], etc., set on the text line. References are to be listed in numerical order on a separate sheet. All references are to be given in Latin letters. The names of the authors are given without inversion. Titles of journals must be abbreviated according to Chemical Abstracts and given in italics, the volume is typed in bold, the initial page is given and the year in parentheses. Attention is drawn to the following conventions: a) The names of all authors of a certain publication should be given. The use of "et al." in the list of references is not acceptable; b) Only the initials of the first and middle names should be given. In the manuscripts, the reference to author(s) of cited works should be made without giving initials, e.g. "Bush and Smith [7] pioneered...". If the reference carries the names of three or more authors it should be quoted as "Bush et al. [7]", if Bush is the first author, or as "Bush and co-workers [7]", if Bush is the senior author.

Footnotes should be reduced to a minimum. Each footnote should be typed double-spaced at the bottom of the page, on which its subject is first mentioned. **Tables** are numbered with Arabic numerals on the left-hand top. Each table should be referred to in the text. Column headings should be as short as possible but they must define units unambiguously. The units are to be separated from the preceding symbols by a comma or brackets. Note: The following format should be used when figures, equations, etc. are referred to the text (followed by the respective numbers): Fig., Eqns., Table, Scheme.

Schemes and figures. Each manuscript should contain or be accompanied by the respective illustrative material, as well as by the respective figure captions in a separate file. As far as presentation of units is concerned, SI units are to be used. However, some non-SI units are also acceptable, such as °C, ml, l, etc. Avoid using more than 6 (12 for review articles) figures in the manuscript. Since most of the illustrative materials are to be presented as 8-cm wide pictures, attention should be paid that all axis titles, numerals, legend(s) and texts are legible.

The authors are required to submit the text with a list of three individuals and their e-mail addresses that can be considered by the Editors as potential reviewers. Please note that the reviewers should be outside the authors' own institution or organization. The Editorial Board of the journal is not obliged to accept these proposals.

The authors are asked to submit **the** final text (after the manuscript has been accepted for publication) in electronic form by e-mail. The main text, list of references, tables and figure captions should be saved in separate files (as *.rtf or *.doc) with clearly identifiable file names. It is essential that the name and version of the word-processing program and the format of the text files is clearly indicated. It is recommended that the pictures are presented in *.tif, *.jpg, *.cdr or *.bmp format. The equations are written using "Equation Editor" and chemical reaction schemes are written using ISIS Draw or ChemDraw programme.

EXAMPLES FOR PRESENTATION OF REFERENCES

REFERENCES

1. D. S. Newsome, Catal. Rev.–Sci. Eng., 21, 275 (1980).
2. C.-H. Lin, C.-Y. Hsu, J. Chem. Soc. Chem. Commun., 1479 (1992).
3. R. G. Parr, W. Yang, Density Functional Theory of Atoms and Molecules, Oxford Univ. Press, New York, 1989.
4. V. Ponec, G. C. Bond, Catalysis by Metals and Alloys (Stud. Surf. Sci. Catal., vol. 95), Elsevier, Amsterdam, 1995.
5. G. Kadinov, S. Todorova, A. Palazov, in: New Frontiers in Catalysis (Proc. 10th Int. Congr. Catal., Budapest (1992), L. Guzzi, F. Solymosi, P. Tetenyi (eds.), Akademiai Kiado, Budapest, 1993, Part C, p. 2817.
6. G. L. C. Maire, F. Garin, in: Catalysis. Science and Technology, J. R. Anderson, M. Boudart (eds.), vol. 6, Springer Verlag, Berlin, 1984, p. 161.
7. D. Pocknell, GB Patent 2 207 355 (1949).
8. G. Angelov, PhD Thesis, UCTM, Sofia, 2001, pp. 121-126.
9. JCPDS International Center for Diffraction Data, Powder Diffraction File, Swarthmore, PA, 1991.
10. CA 127, 184 762q (1998).
11. P. Hou, H. Wise, J. Catal., in press.
12. M. Sinev, private communication.
13. <http://www.chemweb.com/alchem/articles/1051611477211.html>.

Texts with references which do not match these requirements will not be considered for publication!!!

CONTENTS

<i>G. Geniş, O. İsmail</i> , Drying of sour cherry with microwave and infrared drying methods; investigation of drying kinetics and parameters.....	59
<i>M. Marcheva, M. Petkova V. Slavova, V. Popov</i> , Biochemical, transcriptional and fluorescence spectroscopy analysis of fatty acids in seeds of camelina varieties in the organic intercropping system.....	68
<i>K. V. Stefanova</i> , Determination of boundary conditions from experimental data for computational fluid dynamics simulations for phases change material solutions in the ground mass with emphasis on ground heat exchangers.....	78
<i>N. Samghouli, L. Rghioui, S. Sebbahi, A. El Hajji, L. Guennoun, R. Khaoulaf, M. Serghini Idrissi, S. El Hajjaji</i> , Removal of methylene blue from aqueous solution by loquats nuclei..	85
<i>M. M. Momchilova, D. N. Gradinarska-Ivanova, K. I. Valkova-Yorgova, D. G. Yordanov</i> , Comparative analysis of the effect of cricket powder and spirulina in model meat systems as substitutes for soy in raw pork products.....	94
<i>V. A. Majidzade, S. F. Jafarova, S. P. Javadova, A. N. Azizova, S. D. Dadashova, A. Sh. Aliyev, D. B. Tagiyev</i> , Electrodeposition of Mo-Se thin films and influence of the main factors on their composition.....	102
<i>N. Delinska, M. Perifanova-Nemska D. Blazheva, A. Slavchev</i> , Research on the potential of postbiotics in soaps for improving their quality and functionality.....	108
<i>E. Ganev, D. Nikolova, E. Kirilova, R. Vladova, V. Beschkov, T. Valkanova, B. Burdin, E. Slavcheva, J. Iliev</i> , Sustainable design approach of a hydrogen production supply chain through water electrolysis.....	114
<i>E. Ganev, V. Beschkov, E. Kirilova, D. Nikolova, R. Vladova, M. Dimova-Gabrovska</i> , Optimization approach for the design of a sustainable hydrogen supply chain through steam methane reforming.....	123
<i>INSTRUCTIONS TO AUTHORS</i>	131